論文 / 著書情報
Article / Book Information

題目(和文)	
Title(English)	Beam Monitor Development for the RF Cavity Tuning of High-Intensity Proton Accelerator Facility
著者(和文)	三浦昭彦
Author(English)	Akihiko Miura
出典(和文)	学位:博士（工学）, 学位授与機関:東京工業大学, 報告番号:甲第10208号, 授与年月日:2016年3月26日, 学位の種別:課程博士, 審査員:堀岡 一彦,堀田 栄喜,高山 健,小栗 慶之,長谷川 純
Citation(English)	Degree:, Conferring organization: Tokyo Institute of Technology, Report number:甲第10208号, Conferred date:2016/3/26, Degree Type:Course doctor, Examiner:,,,,
学位種別(和文)	博士論文
Type(English)	Doctoral Thesis

Beam Monitor Development for the RF Cavity Tuning of High-Intensity Proton Accelerator Facility

Akihiko Miura

Department of Energy Sciences,
Interdisciplinary Graduate School of Science and Engineering,
Tokyo Institute of Technology

February 2016

Beam Monitor Development for the RF Cavity Tuning of High-Intensity Proton Accelerator Facility

ABSTRACT

The present thesis describes a beam monitor development and tuning results using developed beam monitors in the linac of Japan proton accelerator research complex (J-PARC). This thesis consists of the following nine chapters.

Because the thesis mainly refers to the beam monitor development to meet with the project of output energy upgrade of J-PARC linac, the outlines of the J-PARC history and the linac upgrade project are introduced in the first chapter (Chapter 1). Also the objectives of the beam monitors developed in the project are mentioned.

After the introduction, tuning strategies are introduced to prepare the explanation of the beam commissioning using the newly developed beam monitors. Before the descriptions of each beam monitor, a beam monitor layout which is strongly contributed to the tuning strategies is introduced and the design specification are summarized in the chapter (Chapter 2).

From chapter 3 to 7, a basic idea of the design and a fabrication of the beam monitors are introduced. Chapter 3 is for a beam current and phase monitor, chapter 4 is for a beam position monitor, chapter 5 is for a transverse profile monitor, chapter 6 is for a longitudinal beam profile monitor and chapter 7 is for a beam loss monitor. A theoretical calculation and an analysis are conducted for the beam monitor design of the beam monitors to be installed in the energy upgraded beam line and some of the results are shown. For the upgrade project, we chose annular-coupling structure linac (ACS) cavities. The most important tuning after the project is the longitudinal beam profile matching at the injection point of the new ACS cavities because the acceleration frequency of ACS is thrice of the SDTL. Both the transverse and longitudinal beam profile monitors are developed and improved. The new tuning strategy using these profile monitors is also introduced in these chapters. These chapters refer to the characteristic data obtained from on- and off-line tests. In the last of these chapters, the configurations of the beam monitoring system of the linac are introduced.

Newly developed beam monitors are commissioned to check the proper functioning of monitors and used for the beam dynamics studies. Finally a beam commissioning using the newly developed beam monitors and an interlock systems is discussed (Chapter 8).

The last chapter (Chapter 9) summarizes the beam monitor development for the energy upgrade and shows the results of their beam dynamics studies together with the conclusion of the thesis.

Beam Monitor Development for the RF Cavity Tuning of High-Intensity Proton Accelerator Facility

Akihiko Miura

CONTENTS

Abstract

Contents

Chapter 1

Introduction

1.1 Outline of the J-PARC Linac Project

The Japan Proton Accelerator Research Complex (J-PARC) facility has been constructed as a joint project of the Japan Atomic Energy Agency (JAEA) and the High Energy Accelerator Research Organization (KEK). The facility comprises a 600-MeV linac, a 3-GeV rapid-cycling synchrotron (RCS), and a 50-GeV synchrotron (Main Ring, MR). In the project plans of J-PARC, half of the 400-MeV beams from the linac are injected to the RCS, while the other half are further accelerated up to 600 MeV by a superconducting linac (SC). The RCS provides a beam power of 1 MW to the pulsed spallation neutron experimental facility of the material and life science facility (MLF) with a repetition rate of 25 Hz, while the 50-GeV MR provides a beam current of 15 μA with a period of 3 s to either the fundamental and nuclear physics experimental facility of the hadron facility (HD) or the neutrino facility (NU) as shown in Fig. 1-1 [1].

Table 1-1 summarizes the history of the beam commissioning in J-PARC. The J-PARC construction started in 2001, and the beam commissioning of the linac started from 2006 and achieved the 181 MeV in 2007, which results in a beam power of about 20 kW at the exit of linac. The corresponding beam power at the exit of RCS reaches about

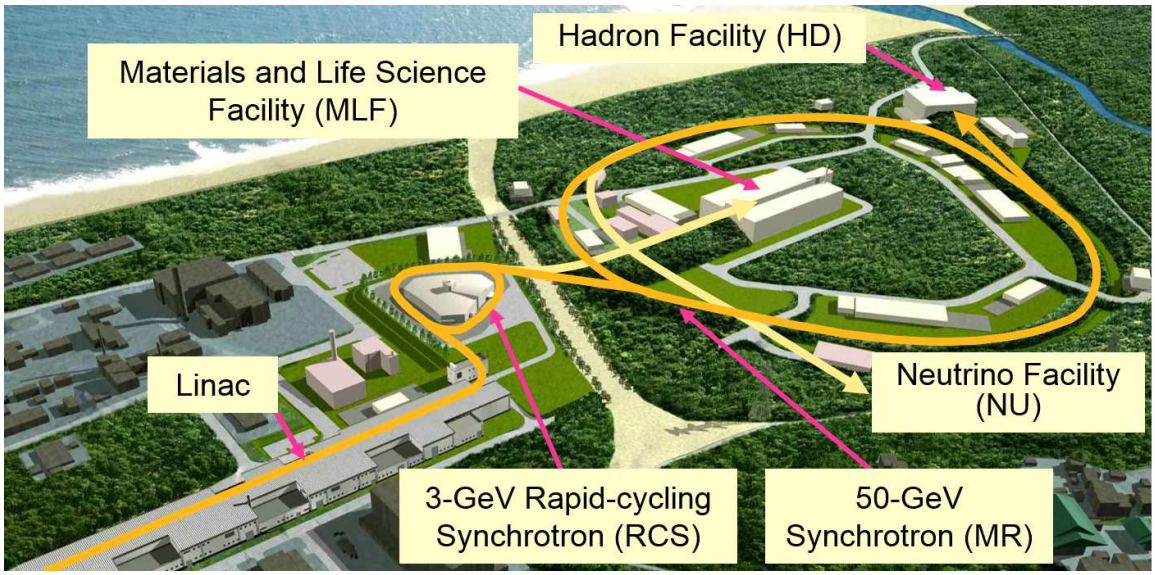

Figure 1-1: Overview of Japan proton accelerator research complex (J-PARC) facility [1].

two hundred kW [2].

The beam commissioning of the RCS started in October, 2007, and the design energy of 3 GeV was achieved within that month. In December 2008, the user experimental operation of the MLF started, and the beam energy of 30 GeV at MR was achieved. The first proton beam reached the hadron experimental facility and the neutrino experimental facility in 2009, proton beams have reached all experimental facilities. The user experimental operation continued with the exception of a 10-month interval due to the gigantic earthquake occurred in March 2011. The gigantic earthquake forced the J-PARC a beam shutdown for restoration efforts. The beam operation of the linac resumed in December 2011 and that for users in January 2012 with beam power of 7.2 kW. The beam power was extended to 13.3 kW in March 2012, which is almost the same beam power as just before the earthquake [3, 4].

Table 1-1. History of J-PARC accelerator commissioning.

Year	Month	Event
2001	Apr.	J-PARC construction started.
2006	Nov.	Linac beam commissioning started.
2007	Jan.	Linac beam energy of 181 MeV was achieved.
	Oct.	RCS beam commissioning started. RCS beam energy of 3 GeV was achieved.
2008	Dec.	User operation of the MLF started. MR beam energy of 30 GeV was achieved.
2009	Jan.	First proton beam was transported to HD.
	Mar.	Energy upgrade of the linac to 400 MeV started.
	Apr.	First proton beams reached the neutrino target.
2011	Mar.	Tohoku earthquake occurred. Gigantic damage occurred.
	Dec.	Beam operation resumed from the earthquake.
2013	May.	Radiation accident in HD. Operation of all facilities suspended.
	Sept.	Installation of energy upgrade equipment completed.
	Dec.	Operation of all facilities resumed excepting HD. Commissioning of 400 MeV started.
2014	Jan.	400-MeV beam energy establishment in linac.
	Sept.	Front-end equipment replacement completed in linac.
	Oct.	Linac commissioning start including 40 – 50 mA trial.
2015	Apr.	HD user operation resumed.

In parallel with the 181-MeV user experimental operation, a 400-MeV energy-upgrade project began in 2009 to achieve the designed RCS beam power of 1 MW. New annular coupling structure linac (ACS) cavities were developed for the energy-upgrade project of a peak beam current up to 50 mA with a replacement of the ion source (IS) and the radio frequency quadrupole linac (RFQ). After completion of the ACS fabrication and installation, the beam commissioning for the 400-MeV beam energy establishment started in December 2013. Based on an achievement of the 400-MeV beam energy in January 2014, 400-MeV beam pulses were injected to and accelerated in the RCS. In September 2014, a replacement of the IS and the RFQ were completed to ramp up the peak beam current, and the commissioning of the higher peak beam current was conducted. At present, the J-PARC linac is operating with a beam energy of 400 MeV, peak beam current of 30 mA, and a repetition rate of 25 Hz and the beam is fully injected to RCS.

1.2 J-PARC Linac Upgrade Project

The linac originally comprised a 50-keV negative hydrogen IS, a 3-MeV RFQ, a 50-MeV drift tube linac (DTL), and a 181-MeV separated-type DTL (SDTL). There were two SDTL-type debunchers allocated downstream of the SDTL section and a linac-to-3-GeV RCS beam transport line (L3BT), as shown in Fig. 1-2. The downstream of future ACS is a beam transport line from linac to 3-GeV Synchrotron (L3BT). The L3BT consists of a straight section, a first arc section, a transverse halo scraper section, a second arc section and an injection section.

Space charge effects in the RCS injection are predicted to be ramped up with the upgrade of peak beam current, and it should limit the beam power. That means the injection energy must be increased to suppress the space-charge effects at the injection point [5]. In this regard, the energy upgrade is essential for increasing the output beam power. To realize 1 MW beam power at RCS, we started to upgrade the energy and to ramp up the peak beam current of the linac.

In the energy-upgrade project, two original debuncher cavities were moved to the end of the SDTL section as the 16th acceleration module of SDTL cavities to increase the accelerated beam energy of 191-MeV (Fig. 1-3). New ACS-type bunchers were installed for longitudinal matching between the SDTL and the ACS cavities because the operating frequency is 972 MHz for the ACS which is a three-fold frequency jump from that of SDTL. In the new ACS section, 21 ACS acceleration modules were installed. The ACS downstream is the beam transport line (L3BT). Two ACS-type debuncher

cavities were placed in the L3BT. The first debuncher (DB1) was located in the straight section for the correction of the momentum centroid jitter. The second one (DB2) was placed at the downstream of first arc section and it is for the optimization of the momentum spread at the RCS injection. There are four beam dumps for independent linac beam commissioning. A straight beam dump was placed at the most upstream.

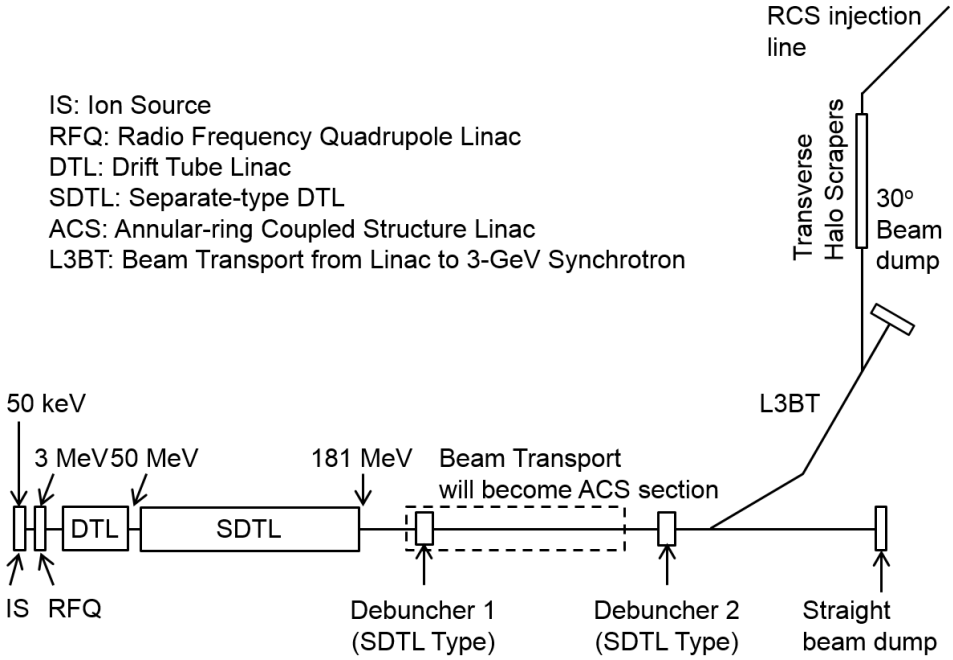

Figure 1-2: The original beam line of J-PARC linac.

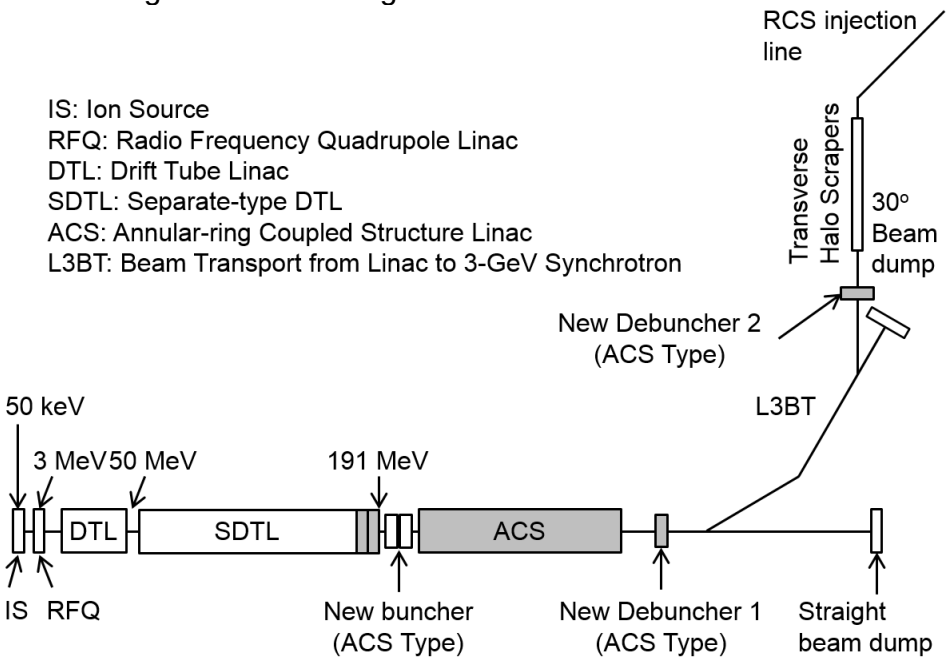

Figure 1-3: Beam line after energy-upgraded linac.
Differences from the original beam line are shown in gray.

For the ramp up of peak beam current, we replaced the IS and the RFQ to deliver a peak beam current of 50 mA. The user experimental operation is still at 30 mA level, but 40-mA and 50-mA operations were conducted to demonstrate an operational parameters and for the performance evaluation [6].

The time structure of the beam pulse in the linac made for RCS injection is shown in Fig. 1-4 which is composed of a 324-MHz micro-bunch, a 560-ns intermediate bunch length, and a 0.5-ms macro-pulse length with 25-Hz repetitions. The longest pulse duration we have to observe occurs during the 0.5-ms macro pulse.

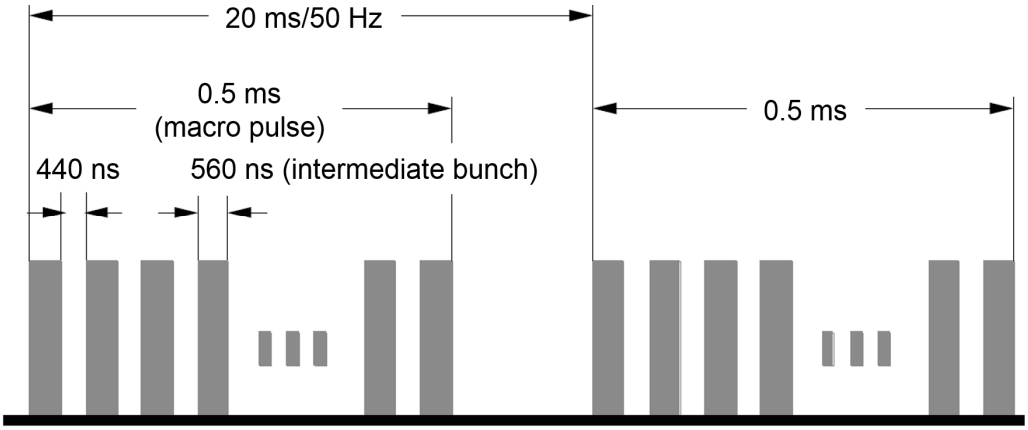

Figure 1-4: Required time structure of the linac beam pulse; pulse length of 0.5 ms, designed repetition rate of 50 Hz (at present 25 Hz), and chopping ratio of 56%.

Table 1-2 shows the main parameters in the present stage (after) and before the upgrade. The J-PARC linac had been operating with an output energy of 181 MeV and a designed peak current of 30 mA. After the beam is chopped between the RFQ and the DTL, the average linac beam power should be more than 18-kW for sustaining 300-kW operation of the RCS.

1.3 Beam Monitors for RF Accelerator Tuning

We are planning to provide a high power beam from the linac which comprises 50-mA peak current and 400-MeV energy to achieve 1-MW beam power at the RCS. The main purpose of the tuning is to achieve a stable beam condition with small emittance and low loss. For this purpose, the acceleration cavity, the acceleration frequency, and the aperture size of the transport line were carefully designed. In addition, the transverse and the longitudinal focusing forces were optimized to make a balance between the beam size and the transport line. That is necessary to suppress the beam loss as small as possible in the beam commissioning.

Table 1-2. Design beam parameters before and after energy upgrade.

	Before Energy Upgrade	After Energy Upgrade
Beam Particle	Negative Hydrogen	Negative Hydrogen
Peak Beam Current	5-15 mA	5-50 mA
Output Energy	181 MeV	400 MeV
Typical Bunch Length	5-6^{o} (rms)	2-3^{o} (rms)
Typical Transverse Width	1-2 mm (rms)	1-2 mm (rms)
Macro Pulse Width	0.5 ms	0.5 ms
Acceleration RF Frequency	RFQ, DTL, SDTL: 324 MHz	RFQ, DTL, SDTL: 324 MHz ACS: 972 MHz
Bunch Repetition Frequency	324 MHz	324 MHz
Operational Repetition Rate	25 Hz	25 Hz
Chopper Beam-on Ratio	56 %	56 %
Beam Power at the Exit of Linac	18 kW	133 kW

The peak beam current, the beam energy, the energy (or momentum) spread, and the transverse emittance are key parameters to inject the high power beam to the RCS, and these should be adjusted to the RCS requirement. If beam halo occurs due to mismatching, it may lead to a significant beam loss. To obtain the proper injection parameters to RCS, we have developed the following beam monitors: beam position monitor (BPM), beam current monitor (slow current transformer, SCT), beam phase monitor (fast current transformer, FCT), transverse profile monitor (wire scanner monitor, WSM), and beam loss monitor (BLM). All of the beam monitors have played important roles in the RF accelerator tuning. Also the BPM, the SCT, the FCT, and the BLM have been used for the continual user operation.

Even though proper parameters were obtained, these would not be extended to beam operations with higher peak current and energy. In these cases, mismatching and transverse-longitudinal coupling may degrade the beam power of world top level.

1.4 Objectives of the Study

Although the final goal of J-PARC is to achieve a beam power of 1 MW at the exit of RCS, the establishment of 400-MeV operation in the linac and tentative high power demonstrations are important milestones for the high-power beam operation. Based on the original tuning strategies, we discussed new tuning strategies to meet with the beam energy upgrade and the peak beam current ramp up. In particular in the energy upgrade,

the acceleration frequency jumps to 972 MHz which is thrice that of the SDTL frequency. We focused the beam dynamics at the frequency jump phase that may lead to increase of longitudinal mismatch [7], and we decided to develop new tuning methods to match the longitudinal beam-width. We also focused on the transvers-matching device to keep the equi-partitioning beam transport design which avoids an excess emittance growth due to mismatching of the transverse beam width or a transverse-longitudinal emittance exchange. Taking into consideration of the matching of both transverse and longitudinal beam profiles, the objectives of this study were set as follows;

1. to modify the transverse beam profile monitor for the high beam current,
2. to develop the longitudinal beam profile monitor for the frequency jump, and
3. to establish the tuning strategies using the developed profile monitors.

For the transverse beam profile monitor, we need to consider not only durability to the high beam current, but the sensitivity of 10^{+4} dynamic range which concerns the beam halo measurements.

The studies presented in this thesis are motivated towards the development of beam monitors for the upgraded J-PARC linac and also for high-power ion accelerators. Therefore the commissioning for the up-graded (400-MeV) beam energy is included in the objectives of this study. The evaluation of the specification of monitors is also included in the objectives of this study whether it can be accommodated to the upgraded linac.

1.5 Contents of the Thesis

Outlines of the J-PARC history and the linac upgrade project were introduced briefly in the first chapter (Chapter 1), because the thesis mainly refers to the beam monitor research and development to meet with the project of J-PARC linac upgrade. The objectives and the content of the thesis were described in this chapter.

Specification of the beam monitors are strongly depending on the accelerator tuning strategies and the installed location. In chapter 2, the author introduces the tuning strategies for the achievement of high intensity beam operation. Based on them, the layout for the beam energy and beam transmission measurement is discussed. The layout is including a longitudinal and transverse profile monitor for profile matching using RF accelerator cavities and quadrupole magnets. Finally, the requirement for the beam monitor design and installation are summarized.

In chapters 3 to 7, basic ideas of the design and the fabrication processes of the beam

monitors are shown. Chapter 3 is for a beam position monitor, chapter 4 is for a beam current and phase monitor, chapter 5 is for a transverse profile monitor, chapter 6 is for a longitudinal beam profile monitor which is the key device for the longitudinal beam matching, and chapter 7 is for a beam loss monitor. Theoretical calculations and analyses conducted for the design of the beam monitors are shown in these chapters. The design works enable to develop highly sensitive monitors that realize to measure its halo together with the beam profile. It also provides us important information on the existence of neutral hydrogens which lead to loss of the beam particles. The author explains such a new measurement scheme in chapter 6, in which a longitudinal beam profile monitor and its operation are shown. The author discussed the measurement errors of the longitudinal profile measurement and the beam operation design by beam study using the device. In these chapters, the author also refers to the characteristic data obtained from on- and off-line tests. The tuning strategy using the monitor is presented which leads to establish the energy upgraded beam operation and a proper beam injection scheme to the RCS. In the last of these chapters, configurations of the beam monitoring system of the linac are shown.

In chapter 8, the commissioning procedure of the accelerator using newly developed beam monitors is explained and the discussion on the beam dynamics in the linac is shown. In the last chapter, researches and developments of beam monitors and their commissioning processes for high-power ion accelerators are summarized based on the results of this study.

References

[1] Y. Yamazaki, ed., “Technical Design Report of J-PARC”, *KEK Report 2002-13*; JAERI-Tech 2003-44 (2003).

[2] N. Ouchi, “Status of the J-PARC Project”, *Journal of the Korean Physical Society*, **Vol. 52**, No. 3, pp. 699-709, (March 2008).

[3] A. Miura, et. al., “Beam Monitor Deformation by Tohoku Earthquake and its Recovery Project”, *Proceedings of the second International Particle Accelerator Conference (IPAC´11)*, **WEPC144**, San Sebastian, Spain, September, (2011).

[4] T. Maruta, et. al., “Progress of Beam Commissioning and Beam Loss Mitigation in J-PARC Linac after the Tohoku Earthquake”, *Journal of the Korean Physics Society*, **Vol. 63**, No. 7, Oct. 2013, pp. 1274-1279.

[5] P. K. Saha, et. al., “Beam Emittance Control by Changing Injection Painting Area in a Pulse-to-pulse Mode in the 3-GeV Rapid Cycling Synchrotron of Japan Proton

Accelerator Research Complex", *Physical Review Special Topics – Accelerators and Beams*, **16**, 120102, (2013).

[6] H. Oguri, "Power Upgrade of J-PARC Linac", *Proceedings of the 4th International Particle Accelerator Conference* (IPAC2013), **WEYB101**, Shanghai, China, May (2013).

[7] David McGinnis, "Status of the Felmilab Booster After the 400 MeV Upgrade", *Proceedings of the Fourth European Particle Accelerator Conference* (EPAC94), London, England, **0497**, (1994).

Chapter 2

Method of RF Cavity Tuning of J-PARC Linac

Beam monitors are essential instrumentations for tuning of the accelerator, maintaining the beam quality, mitigating the beam loss, and indicating the operational status. At the first stage of the linac beam commissioning using 5-mA beam current to establish 181-MeV beam energy, commissioning strategies were proposed for the RF cavity tuning, the beam loss mitigation, and the injection control to RCS. Based on the commissioning strategies, the numbers of beam monitors and their layout were determined considering the redundancy in the original beam line. The numbers of beam monitors used in the original beam line are listed in Table 2-1 [1].

Some of the commissioning strategies can be followed for the upgraded linac, however effects of wake field generated by the beam space charge and thrice frequency up-shift of the ACS cavities are the issues to be discussed [2, 3]. In this chapter, we introduced commissioning strategies which had been employed for the original beam line. We discuss change points of the commissioning strategies and propose a monitor layout for the upgraded beam line. Finally, we summarize the requirements for the beam monitor design and new tuning method.

2.1 Beam Commissioning Strategies

2.1.1 Beam Energy Measurement

Beam energy is an essential parameter for the RF cavity settings and injection controls. We measured the energy by the time of flight (TOF) method using a pair of the beam phase monitors. A schematic of the beam energy measurement by the TOF is described in Fig. 2-1. For the TOF measurements, a pair of the fast current transformers (FCTs) was placed at a drift section, namely at the place between the RF cavities. The length between the FCTs is defined by the $\beta\lambda$ period, where β is relative velocity and λ is the wave length of RF field. We placed them with short distance of 2.5 $\beta\lambda$ usually and also with long distance of 21 $\beta\lambda$ as reference.

Beam energy is described using the following formula,

$$K = m_0 c^2 \cdot (\gamma - 1). \qquad (2\text{-}1)$$

Where γ is the Lorentz factor defined by,

$$\gamma = \frac{1}{\sqrt{1-\beta^2}},\ \beta = \frac{L}{\Delta t \cdot c}\ . \qquad (2\text{-}2)$$

Table 2-1. Numbers of beam monitors for the original beam line and the energy-upgraded beam line.

Section of Linac	Beam Monitor	Numbers for Original Beam Line	Numbers After Energy Upgrade
Front-end between IS and DTL	BPM	8	8
	FCT	4	4
	SCT	5	5
	WSM	4	4
	BLM	0	0
DTL	BPM	0	0
	FCT	3	3
	SCT	3	3
	WSM	0	0
	BLM	10	10
SDTL	BPM	31	32
	FCT	44	46
	SCT	15	16
	WSM	4	4
	BLM	16	16
MEBT2*	BPM	4	6
	FCT	1	8
	SCT	3	2
	WSM	1	0
	BLM	5	5
ACS	BPM	11	42
	FCT	3	42
	SCT	3	21
	WSM	3	4
	BLM	21	21
	BSM	0	3
L3BT	BPM	40	40
	FCT	4	7
	SCT	7	7
	WSM	20	20
	BLM	33	33
Beam Dump (4 beam dumps)	BPM	8	8
	FCT	1	1
	SCT	4	4
	WSM	4	4
	BLM	5	5

* MEBT2 is the beam transport and matching section between SDTL and ACS.
BPM: Beam Position Monitor
FCT: Fast Current Transformer, Beam Phase Monitor
SCT: Slow Current Transformer, Beam Current Monitor
WSM: Wire Scanner Monitor, Transverse Beam Profile Monitor
BLM: Beam Loss Monitor

Here, Δt is the flight time and L is the flight length. Then, Δt can be correlated to the phase shift at operational frequency of 324 MHz as follows,

$$\Delta t = \Delta\theta/360 \times 324 \times 10^6, \text{ and} \quad (2\text{-}3)$$

$$\Delta\theta = \theta_{FCT1} - \theta_{FCT2} \pm n \times 360. \quad (2\text{-}4)$$

These equations allow to estimate the phase delay from the TOF signals of FCTs (FCT1 and FCT2). The length L was measured using a laser measurement system with accuracy of ± 0.1 mm.

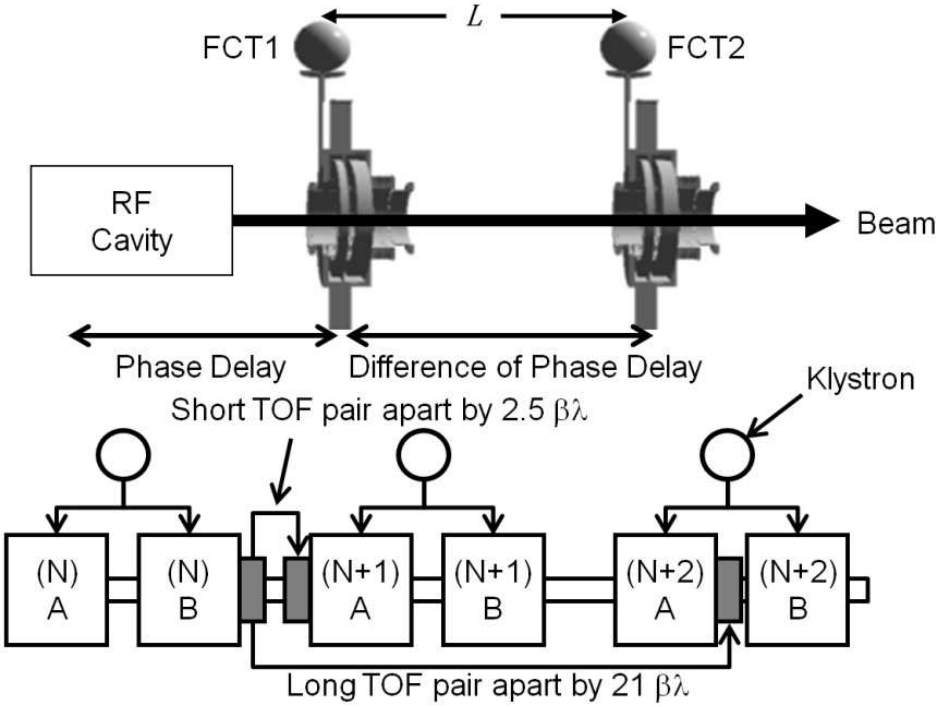

Figure 2-1: Schematic of the beam energy measurement by TOF method.

2.1.2 RF Cavity Tuning

In the tuning of amplitude and phase of the RF acceleration cavity, a phase-scan method has been adopted using above energy measurement. There is a variety of phase-scan methods with different monitor setups and different approaches. In the tuning of J-PARC RF cavities, the following three schemes were considered [4, 5];

Scheme I: RF amplitude and phase are scanned at just after the cavity under tuning. The output beam phase is measured with an FCT. Only the relative variation of output beam phase is used to find the RF phase and amplitude.

Scheme II: RF amplitude and phase are scanned with measuring the beam energy after the cavity under tuning. The output beam energy is measured with two FCTs based on the TOF method. While the beam energy is measured,

only the relative variation of the beam energy is used to find the RF amplitude and phase.

Scheme III: The setting is essentially the same with Scheme II, but the knowledge of the absolute output energy is used to find the RF amplitude and phase.

After the consideration, the proper amplitude and the phase of each accelerating cavity were set by using a phase scan method [5-7] based on the TOF measurement (scheme II) with a pair of FCTs.

An example of the results is shown in Fig. 2-2 which indicates the phase scan curves for the SDTL16. When the RF phase of the SDTL16 was scanned, the input energy from the exit of SDTL15 was 181.1 MeV with energy range from 170.8 to 191.4 MeV. The top half of the scan result means an acceleration phase up to about 10 MeV and the bottom half shows a de-acceleration phase. Amplitude of the waveform corresponds to the input voltage of the RF cavity. The agreements between the measured energy and the simulation were very well, as shown in Fig. 2-2, which indicates that the tuning error is within 1.0 % in amplitude and $\sim 6.0^{o}$ in phase. As shown in Fig. 2-1, two SDTL and ACS cavities are driven by one klystron, the phase scans were performed one by one.

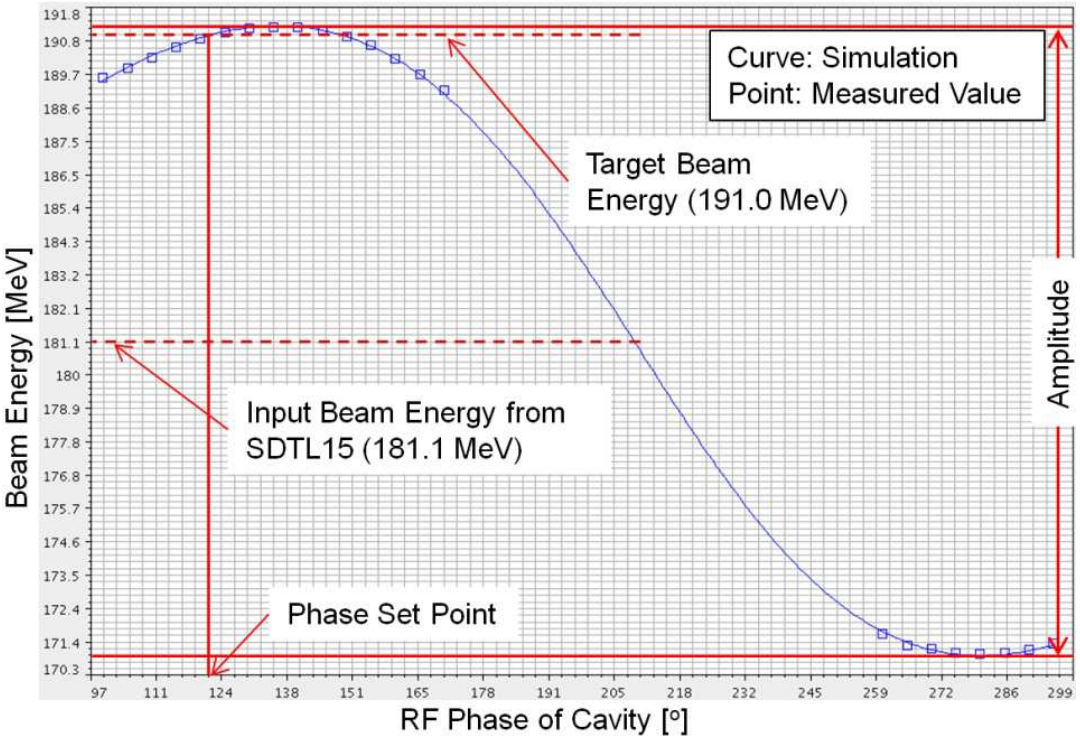

Figure 2-2: Example of phase scan result taken at SDTL16.Points are beam energies taken with 2^{o}-intervals at the top and bottom of the scanning results, and curve shows the simulation (PARMILA) result.

2.1.3 Beam Transmission

The beam transmission is continuously observed through the commissioning and user operations using slow current formers (SCTs). Signals are plotted with the location as shown in Fig. 2-3. The trend shows a typical beam transmission in the beam line. When a large transmission drop is observed in the beam line, we tune the settings of RF buncher, steering, and quadrupole magnets to suppress the beam loss.

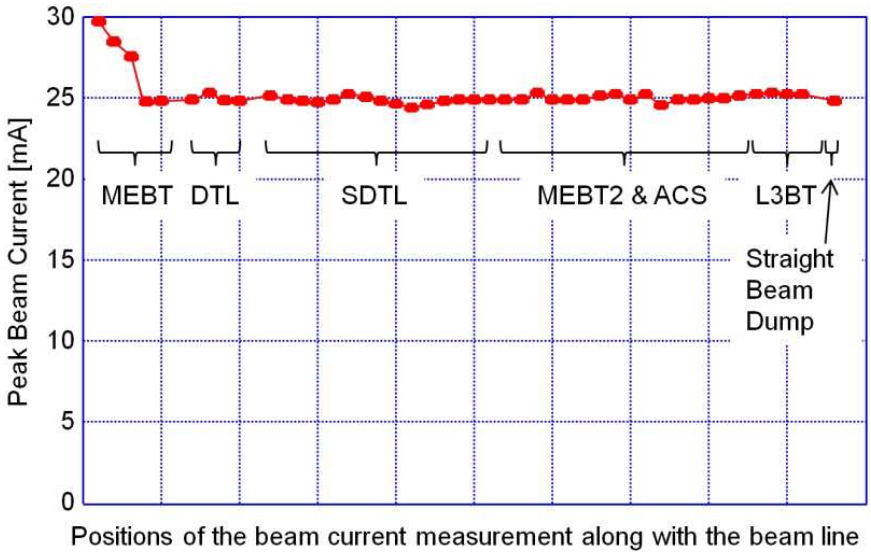

Figure 2-3: Aligned beam current measurement results in beam line taken at 25-mA operation. Vertical line means peak beam current and horizontal one shows the location.

2.1.4 Beam Orbit Tuning

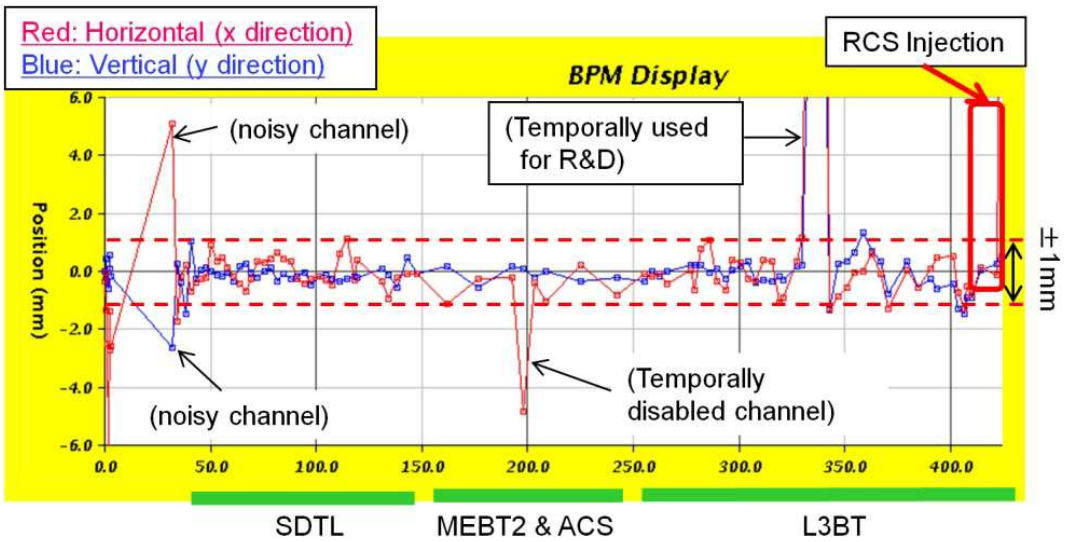

Figure 2-4: Results of beam position measurement with beam line taken at 15-mA operation before the energy upgrade. Vertical line means offset beam position from aligned center axis.

Figure 2-4 shows typical results of beam position measurement using beam position monitors (BPMs). As shown, the beam orbit was tuned within 2.0 mm error with small oscillation around the center of the beam ducts and cavities, excepting an injection points. We used the steering magnets to correct the beam orbit to the aligned center axis (0.0 mm).

2.1.5 Transverse Profile Tuning

The beam size mismatch is defined as $(W_{max} - W_{min}) / (W_{max} + W_{min})$, where W_{max} and W_{min} are the RMS beam widths of the most and the least broad profile at four measuring positions. In order to suppress emittance growth, the tolerance for the RMS beam size mismatch should be set to be less than 10 % which was set as a goal for transverse tuning. To achieve this goal, we proposed a scheme for transverse matching [8] in which three or more WSMs are placed periodically. Quadrupole magnets were located in front of the WSMs and tuned to have the same beam widths at the wire scanner locations. Although three wire scanners are sufficient for this scheme in principle, additional wire scanners were prepared to improve tuning accuracy and for redundancy. Four WSMs were installed in series in the vicinity of the matching point where an adequate set of quadrupole magnets are adjusted. The adequate set of parameters was found through trial and error by adjusting the strengths of the four quadrupole magnets.

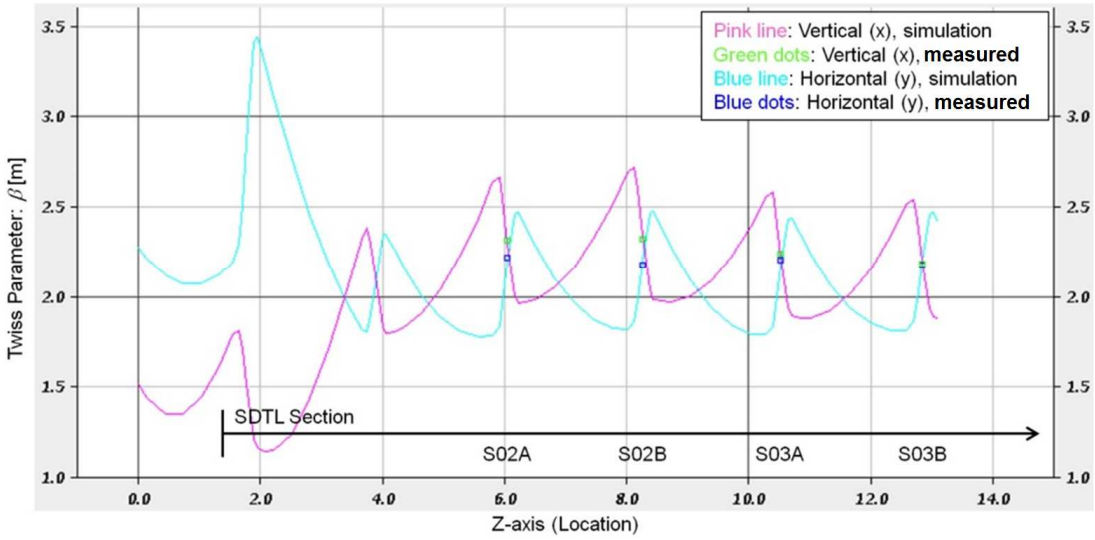

Figure 2-5: Transverse tuning method in SDTL section. Pink and blue lines are the simulated beam envelope evolution.

Adopting the transverse matching scheme is preferred because the scheme only needs accuracy relative to the beam width. To adopt this scheme, the lattice should be periodic, and the longitudinal profile around the matching section should be reasonably uniform. We assessed the optimal initial conditions using Trace3D and have succeeded in restricting the number of tuning quadrupoles to four at all matching points.

Figure 2-5 shows an example of the transverse matching procedure at the Separated-type Drift Tube Linac (SDTL) section in the linac. Pink and blue lines indicate the evolution of the simulated beam envelope. In the matching sections, we aligned the RMS beam sizes (green and blue dots), which are determined periodically by WSMs located in the matching section.

2.1.6 Beam Loss Mitigation

There are a lot of knobs to mitigate the excess beam loss, because the cause of the beam loss is in a variety aspect of beam properties. Misalignment of the beam orbit is one of the important causes. This is not only caused by the setting error of the steering magnet, but induced also by the misalignment of the beam transport line. Instability at the RF cavity is another reason of the beam loss. If an electronic discharge or a multipactoring occurs frequently in an RF cavity, the RF field becomes unstable. To avoid this situation, parameters of RF settings, i.e., the amplitude of the RF field should be changed. However, this may cause emittance growth because modifying the amplitude of RF cavity locally changes the longitudinal focusing force which may induce an erratic beam behavior in the whole of cavities.

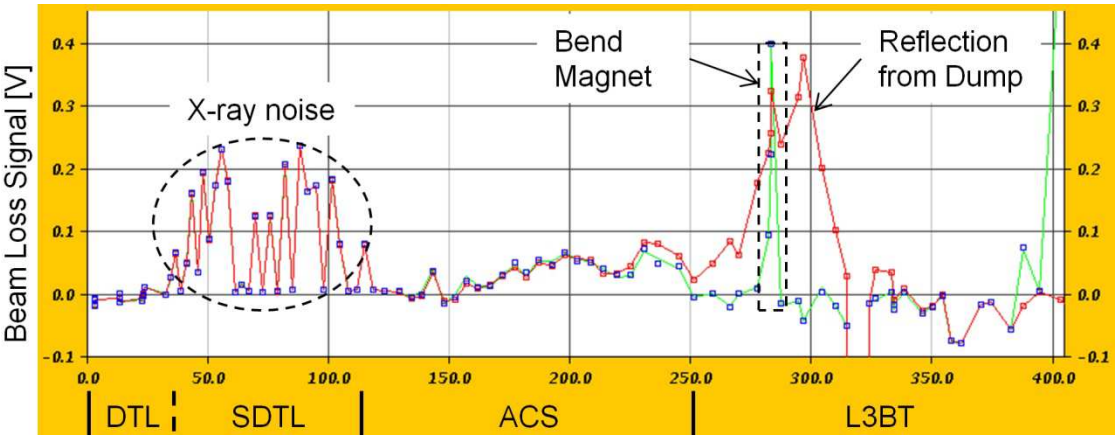

Figure 2-6: Typical beam loss trends along the beam line. Red trend shows the beam loss signals obtained at beam operation to straight beam dump. Green trend is the signals at beam operation to RCS injection.

A localized misalignment of high power density beam leads to destroy or heavily activate the accelerator equipment. This fact makes the beam loss monitor (BLM) system to be one of the essential diagnostic tools for beam tuning. It should suppress the radiation outside the accelerator shielding and the losses to a level which ensures hands-on-maintenance of the accelerator components during shutdown. Beam loss signals taken at 15-mA operation aligned in the beam line is shown in Fig. 2-6. For the beam loss mitigation, total beam loss signal is carefully observed when we change the parameters.

2.1.7 Commissioning Strategies for Upgraded Beam Line

The aim of the beam commissioning after energy upgrade is to seek an appropriate operational parameters of 400-MeV and higher peak beam current. We have to suppress excess beam losses induced from insufficient operation-parameter tuning of which effect is not clearly seen in the original 181-MeV operation. We plan to perform the tuning of ACS cavities with our original method, because we can make commissioning under 5-mA peak beam current without considering the effect combined by the higher peak current.

After establishing 400-MeV acceleration, additional tunings are needed to suppress the beam loss and improve the beam quality. It includes orbit correction, transverse and longitudinal matching, and so on.

As a three-fold frequency jump is planned at a place between SDTL and ACS, seeking a proper matching condition at the place is crucial to suppress excess beam loss. We have two bunchers for the longitudinal matching and six quadrupole doublets, four of which are used for the transverse matching. A way to conduct the matching is to treat the transverse and the longitudinal matching separately and to iterate the tunings of them until these matchings converge. We expect that the scheme could be advantageous for beams with modest space charge effects as we can employ the same transverse matching scheme for the beams in 181-MeV operation [8].

We plan to adopt similar scheme for the longitudinal direction using three bunch shape monitors (BSMs) installed periodically at the entrance of ACS section. The amplitudes of two bunchers are adjusted so that the measured RMS beam widths with the BSM array become the same. A new way is needed to tune the longitudinal RMS beam size for redundancy which will be discussed in chapter 6.

2.2 Beam Monitor Layout in the Linac Beam Line

The beam monitor layout from the front-end to the end of SDTL15 was the same with the original. Beam monitors were remained in the beam line. Based on the tuning scheme, we arranged the beam monitors from SDTL16 to ACS06 for the energy-upgraded linac as shown in Fig. 2-7.

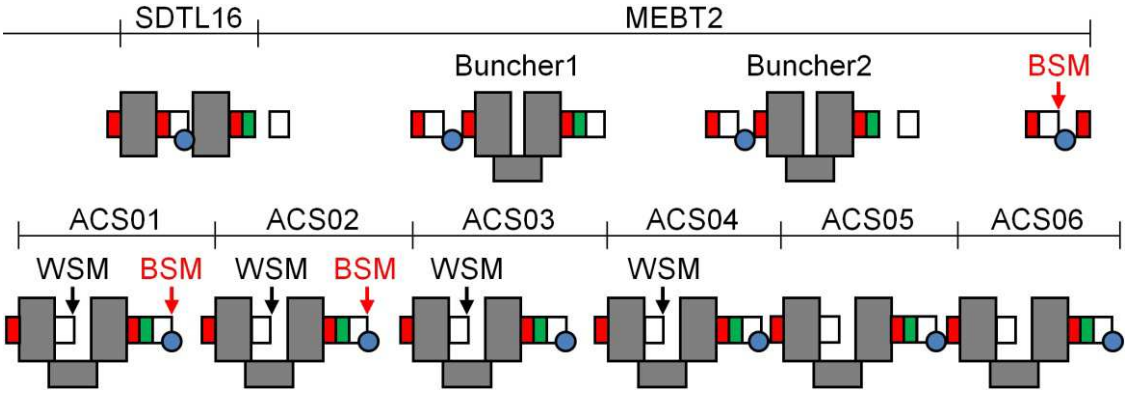

Figure 2-7: Beam monitor layout around SDTL16, matching section between SDTL and ACS (MEBT2), and the upstream part of the ACS section after the energy upgrade.

*gray square: cavity, white square: BPM,
red square: FCT, green square: SCT,
blue circle: BLM, arrow: position of the WSM and the BSM

The detailed layout of beam monitors in each ACS module is shown in Fig. 2-8. One module consists of two accelerating unit cavities and a bridge coupler. There is a drift space for placing the quadrupole doublets at the bridge coupler and another drift space between the modules, where most of the beam monitors were installed. A pair of FCTs was located at the exit of the second cavity and at the entrance of the next cavity to measure the beam energy at the drift space by TOF method. The drift space is narrow compared with the downstream of SDTL, because the frequency jump leads to the shorter drift distance. A farthest combination of FCTs for energy measurement is a reference of the shorter combination in the SDTL section, but shorter one is more accurate because it can avoid the effect of breakdown of the bunch structure during the long drift. We decided to use only shorter combination; therefore a number of FCTs were saved. An SCT and an FCT were placed in the one vacuum chamber package, where the SCT was located behind the FCT to measure the beam current. By comparing the beam currents taken by the upstream and the downstream SCTs, the beam transmission through the acceleration module was measured.

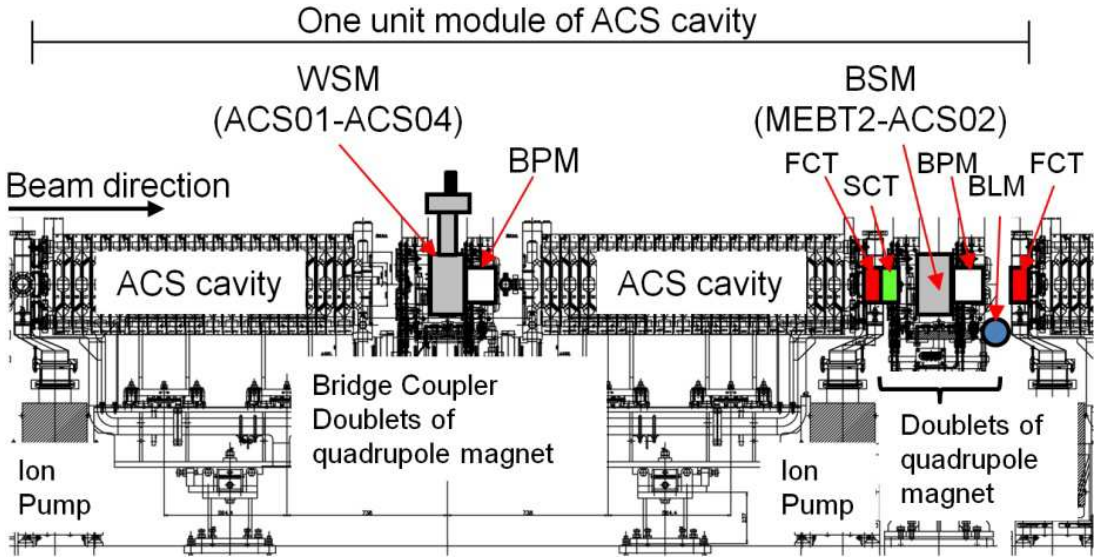

Figure 2-8: Detail layout of beam monitors in each ACS module.

The BPMs were mounted directly on the yoke of the quadrupole magnet to get a higher position accuracy with respect to the quadrupole magnet. A BPM installed on the bridge coupler is used as a backup. The location of the BLM needs to be optimized through verification and sensitivity check because the BLM is sensitive to the X-rays released from the RF cavities (as shown in Fig. 2-6) and the real beam loss signal is difficult to discern amidst a high X-ray background.

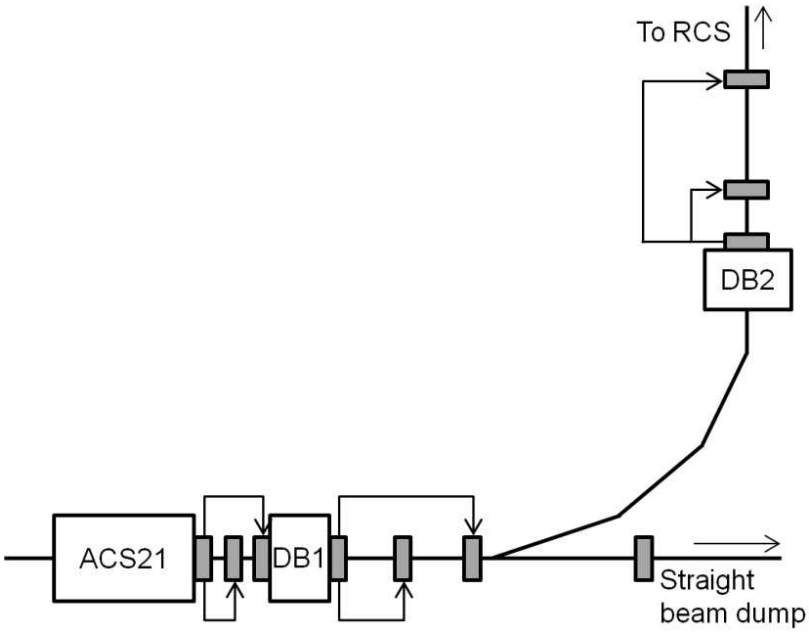

Figure 2-9: FCT layout for downstream of last ACS cavity (ACS21). DB1 and DB2 are the first and the second debuncher, respectively.

We adopted above policy to all of the ACS modules with the addition of a WSM or a BSM for some of the upstream modules. We installed four WSMs between the doublets of the quadrupole magnet on the bridge coupler of the first four ACS modules. Further, we placed a space between the downstream doublets of the module (which usually serves as the place for the installation of a gate valve), and three BSMs located from MEBT2 to the ACS02. In the energy-upgrade project, a total of 49 BPMs, 52 FCTs, 24 SCTs, 4 WSMs, 24 BLMs, and 3 BSMs were either installed or replaced (Table 2-1).
Most of the monitors we used are originally installed in the L3BT. Additional pairs of FCTs for beam energy measurements, as well as for debuncher tuning downstream of each debuncher were installed (Fig. 2-9). Two debunchers downstream of the ACS were used to tune the beam quality for RCS injection. This beam transport line contains a pair of FCTs which determine the set-point for debunchers 1 and 2.

2.3 Beam Monitor Requirement

The main objective of the study is to develop the beam monitors for the achievement of 400-MeV operation. Based on the commissioning strategies, beam monitor requirements were summarized as follows.
Radius of the cavity bore and the beam duct should be several times larger than the RMS beam size to prevent the beam from excess loss [9, 10]. Ability of the high voltage power supplier prevents the beam from the bore size extension. In order to restrict the beam orbit within 2.0 mm, the accuracy of BPM is required to be less than 0.2 mm.
We need monitors with wide dynamic range to account for the complicated pulse structure of beams in the J-PARC linac. To meet with the fastest time structure of 324 MHz, we developed FCTs of which time constant is less than 1.0 ns. Also to measure the small beam current, sensitive SCTs were developed. As the SCTs were adopted to measure the intermediate current pulse, time constant should be less than 0.5 μs. After the ACS section, beam bunch is accelerated by RF field with 972 MHz, but the beam bunch is supplied 324 MHz from the upstream. The phase shift was compared with 324 MHz phase comparator, and the phase accuracy was estimated to be less than 6.5^{o} which is corresponding to momentum shift (Δp) less than 0.5% at 972 MHz. This means the upstream system can inject the 400-MeV beam with energy spread of ± 0.2 MeV. The range and the accuracy of the beam current monitors were estimated to be from 0.1 mA to several tens mA and $\pm 5.0\%$.
For the transverse matching, we need the information on the RMS beam size. The dynamic range of WSM should be larger than 10^{+2} for the RMS beam size adjustment.

Along with the peak beam current ramp up, we have to suppress the emittance growth with monitoring a small beam fluctuation. We designed the WSM with stepping resolution less than 0.1 mm, because the RMS beam size is estimated to be 2-3 mm. The target of the dynamic range of the WSM was set to be 10^{+4} which enables measurement of beam halo with beam current around 1 μA level. It would also bring more accurate RF tuning of chopper cavity which is located in the front-end.

To take longitudinal matching, we newly developed a longitudinal pulse width monitor (BSM). The BSM need to have a dynamic range of 10^{+2} to obtain RMS beam phase size with 1.0^{o} resolution because the estimated beam phase size is 3.0^{o} in the ACS section. For the BSM, the resolution of transverse stepping was designed to be less than 0.1 mm. Beam loss detection is essential to evaluate the radiation through operation. The signal response should be less than 1 μs, because the monitor is used to stop the beam operation when the beam loss was detected. An X-ray sensitive ion chamber was adopted for the loss monitor because of high response and ease of maintenance.

To account for the significant beam-parameter upgrades, the newly-designed beam monitors were installed in the upgraded beam line for the beam commissioning as well as for longitudinal matching. After the installation of the newly-fabricated beam monitors, the commissioning plans to support the beam monitor check were proposed [11].

This study is aiming to discuss new beam monitor designs and their performances, in addition, to provide strategies for extending the range of measurement for the next stage accelerator facilities. The author also proposes an innovative use of the monitors for the beam dynamics studies in high power accelerator in which the space charge affects the beam behavior. We summarized the required specification for the beam monitors to be used in the upgraded beam line in Table 2-2.

Table 2-2. Design requirements of beam monitors.

Monitor	Tuning Device	Requirement
Beam Position Monitor (BPM)	Steering and Quadrupole Magnet	Position Accuracy: ±0.2 mm
Beam Current Monitor (SCT)	Steering Magnet, etc.	Response Time: τ < several tens ns Droop rate: τ_{droop} < 1.0%/μs
Beam Phase Monitor (FCT)	Cavity Amplitude and Phase	Phase: $\phi < 6.5^{o}$, (Δp < 0.05% of 400 MeV) Response Time: τ < 1.0 ns
Transverse Profile Monitor (WSM)	Quadrupole Magnet RF Chopper Phase	Transverse Scan Accuracy: ΔL < ±0.1 mm Dynamic Range: > 10^{+4}
Longitudinal Profile Monitor (BSM)	Cavity Amplitude	Phase Resolution: $\phi < 1.0^{o}$ Transverse Scan Accuracy: ΔL < ±0.1 mm
Beam Loss Monitor (BLM)	Steering and Quadrupole Magnet	Response Time: τ < 0.1 μs

2.4 Summary

In this chapter, we introduced a tuning strategy for the upgraded operational parameters in J-PARC. Methods for energy measurements, RF cavity tunings, beam transmissions, orbit tuning, and beam monitoring for the transverse profile matching, have been proposed and developed for the next stage upgrade in J-PARC. The beam monitor layout was proposed based on the tuning strategies. Moreover, we referred that the layout of J-PARC linac with the tuning strategy was unique and it can provide practical guidepost for planned high power accelerator facilities [12].

The author emphasized that development of the high dynamic range WSM can be used for beam halo measurement. Also the author referred that the development of longitudinal pulse width monitor can be useful to take longitudinal matching at the frequency jump section at J-PARC. Finally, the beam monitor requirements for the development of the high power accelerators were summarized.

References

[1] A. Miura, et. al., “Progress of Beam Instrumentation in J-PARC Linac”, *Proceedings of the First International Beam Instrumentation Conference (IBIC2012)*, Tsukuba, Japan, **MOIA02**p, 2012.

[2] S. Sato, et. al., “Installation of Beam Monitor Sensors in the Linac Section of J-PARC”, *Proceedings of Proceedings of The tenth European Particle Accelerator Conference (EPAC06)*, **TUPCH061**, Edinburgh, Scotland, (2006).

[3] Y. Liu, et. al., “Stability Studies for J-PARC Linac Upgrade to 50 mA/400 MeV”, *Proceedings of the sixth International Particle Accelerator Conference (IPAC2015)*, **THPF039**, Richmond, Virginia, USA, (2015).

[4] D. O. Jeon, “Comparison of Phase Scan vs Acceptance Scan for The SNS DTL”, *Proceedings of the 2006 Linear Accelerator Conference, (LINAC06)*, **TUPAN070**, Knoxville, Tennessee, USA, (2006).

[5] M. Ikegami, et. al., “RF Amplitude And Phase Tuning of J-PARC DTL”, *Proceedings of the 2007 Particle Accelerator Conference (PAC07)*, **TUPAN043**, Albuquerque, New Mexico, USA, (2007).

[6] G. Shen, et. al., “RF Amplitude And Phase Tuning of J-PARC SDTL”, *Proceedings of the 2007 Particle Accelerator Conference (PAC07)*, **TUPAN062**, Albuquerque, New Mexico, USA, (2007).

[7] H. Sako, et. al., “Development of Commissioning Software System for J-PARC Linac”, *Proceedings of the 2007 Particle Accelerator Conference (PAC07)*,

MOPAN044, Albuquerque, New Mexico, USA, (2007).

[8] M. Ikegami, et. al., “Transverse Tuning Scheme for J-PARC Linac”, *Proceedings of the 2005 Particle Accelerator Conference (PAC05)*, **p. 2750**, Knoxville, Tennessee, USA, (2005).

[9] T. Kato, et. al., “Design of Beam-Transport Line between the RFQ and the DTL for the JHP 1-GeV Proton Linac”, *Proceedings of the 1994 International Linac Conference, Tsukuba, Japan (LINAC1994)*, **MO-07**, Tsukuba, Japan, (1994).

[10] K. Hasegawa, et. al., “The KEK/JAERI Joint Project: Status of Design and Development”, *Proceedings of the XX International Linac Conference*, **TU102**, Monterey, California, USA, (2000).

[11] A. Miura, et. al., “Beam Monitors for the Commissioning of Energy Upgraded Linac”, *Conference Proceedings of Journal of the Physical Society of Japan (JPS)*, **No. 8**, 011002, (2015).

[12] S. M. Lidia, et. al., “Overview of Beam Diagnostic System for FRIB”, *Proceedings of the 2015 International Beam Instrumentation Conference (IBIC2015)*, **MOPB071**, Melbourne, Australia, (2015).

Chapter 3

Beam Position Monitor (BPM)

In designing the beam position monitor (BPM), the operational principle is best described by the transfer impedance, which is basically a frequency dependent quantity transferring of the beam current to a voltage signal. For the purpose of the BPM design to meet with the upgraded parameters of linac, we adopted a stripline for the pick-up of the small beam signal and a logarithmic amplifier for the signal processing electronics with wide dynamic range. The required position accuracy is 0.2 mm for beam orbit correction and the time resolution is 20 ns to observe the intermediate pulse, as well as the macro beam pulse.

Sensor head of the stripline BPM was fabricated by the following steps.

1. Design of outer shape and aperture size
2. Design of the stripline length and width
3. Measurement of the characteristic impedance
4. Evaluation of the linearity and the dynamic range including the logarithm amplifier

After the fabrication, installation accuracy was estimated using a test stand. We finally discussed the position accuracy of the beam measurement including installation errors.

3.1 Signal Treatment for Stripline BPMs

An alternating current signal is induced on the electrode and coupled with radio frequency (RF) because the electric field of a bunched beam is time dependent. Four pick-up electrodes are installed crosswise at the beam pipe and the difference of signals from counter-facing electrodes yield the beam's center-of-mass position. They are coupled to the electro-magnetic field generated by the charged particle beam. For relativistic beam velocities the transverse field components in the laboratory frame increase compared to the values within beam's rest frame. The Lorentz transformation from the beam's rest frame to the laboratory frame for the field component transverse to the direction of motion is given by the Lorentz factor $\gamma = 1/\sqrt{1-\beta^2}$ and even for moderate beam velocities the resulting field can be approximated by a so-called transverse electric and magnetic field distribution.

3.1.1 General Formalism

The theoretical estimation of the sensitivity of stripline pick-up was established by R. E. Shafer [1]. He found the sensitivity of the stripline pick-up as the following dB ratio of the wall currents induced at two counter-facing electrodes that are parts of a cylindrical beam pipe.

The dB ratio is given by,

$$\left(\frac{I_{WR}}{I_{WL}}\right) = \frac{160}{ln(10)}(1+G)\frac{sin(\phi/2)}{\phi}\frac{x}{\phi} + O(x^2) \ , \qquad (3\text{-}1)$$

where G is given by,

$$G = 0319\left(\frac{\omega r}{\beta\gamma c}\right)^2 - 0.0145\left(\frac{\omega r}{\beta\gamma c}\right)^3 \ , \qquad (3\text{-}2)$$

ϕ is electrode opening angle, r is radius of beam pipe, x is beam position, ω is angular frequency, and c is velocity of light.

Note that for highly relativistic beam, $G = 0$, and the pick-up sensitivity depends only on the two counter-facing electrode geometry. One of the main features of formulas (3-1) and (3-2) is that the pick-up sensitivity depends on the beam energy and the processing frequency.

3.1.2 Stripline Design and Fabrication

The shape and size of the BPM are severely restricted because they are mounted directly onto the yoke of the quadrupole magnet for installation without any independent BPM alignment. It is known that the stripline type electrode is more suitable to obtain wide frequency characteristic than the electrostatic type electrode which is difficult to tune the frequency characteristic flat around the acceleration frequency owing to the stray capacitance [2].

A drawing of the BPM which is newly designed for the ACS beam line is shown in Fig. 3-1. Here, it is important to note that, inner diameter of the beam pipe is specified to be 40.0 mm, because the electrode of the stripline needs to be placed along the beam pipe diameter to avoid degradation of the accelerator acceptance [3].

The induced voltage from a stripline electrode by beam charge is inversely-proportional to the distance between the electrode as well as to the length, and width of the electrode. When the characteristic impedance at both upstream and downstream terminals is equal to Z_0 (50 Ω), induced voltage at the upstream terminal from the stripline electrode with the length (λ) can be described as the equivalent circuit model of stripline as follows [1]:

$$V(\omega)=\frac{\phi Z_0}{2\pi}\langle I_b\rangle A(\omega)\sin\left[\frac{\omega\lambda}{2c}\left(\frac{1}{\beta_s}-\frac{1}{\beta_b}\right)\right]. \quad (3\text{-}3)$$

Where, ϕ represents the opening angle (Fig. 3-1), and I_b is the peak beam current. $A(\omega)$ is a constant depending on the RF frequency (324 MHz), with β_s as the relative velocity of signal transfer in the electrode and β_b as the relative velocity of the beam. We calculated the electrode length and decided a suitable electrode length which determines the maximum voltage as shown in Eq. (3-3).

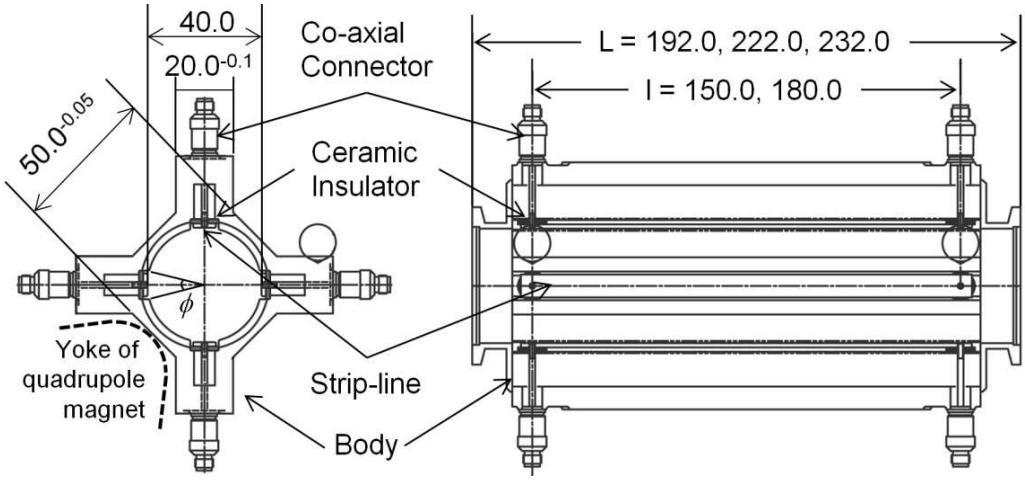

Figure 3-1: Drawing of BPM for ACS section.

The plot of phase term of Eq. (3-3) is shown in Fig. 3-2. Here, the maximum induced voltage can be obtained at the maximum of sinusoidal function. We chose the design length, which ranges from 150 mm to 180 mm corresponding to 181 MeV (β_b=0.55) and 400 MeV (β_b=0.65), respectively.

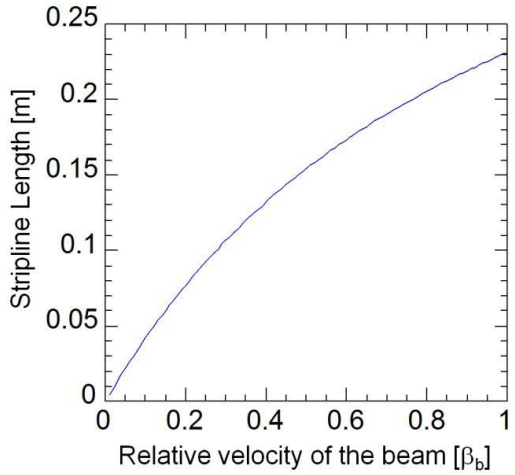

Figure 3-2: Relation between relative velocity (β_b) and stripline length.

The width of the stripline is decided based on its transmission impedance. This impedance should be 50 Ω to match that of the signal cable. To determine the width of the stripline, we calculated the characteristic impedance of the stripline using the cross-sectional distribution of the electrical field generated by the electrical charge of the beam [4, 5]. The characteristic impedance of the stripline is calculated using two-dimensional Poisson equation calculation code "Poisson Super Fish" [6]. In this code, an electrical field was obtained assuming the inducted electrical charge at the surface of the stripline due to the beam particles.

An example of calculated electrical field is shown in Fig. 3-3. As there are symmetries of the shape in each of 4 (right, left, up, and down) electrodes, only a quarter of cross section is shown. At the narrow space which is a gap between the stripline and the body, there is a ceramic insulation, and high electrical field regions can be seen. We varied the width of the stripline as a parameter. After the electrical gradient was obtained, characteristic impedances of the stripline were calculated, which is shown in Fig. 3-4.

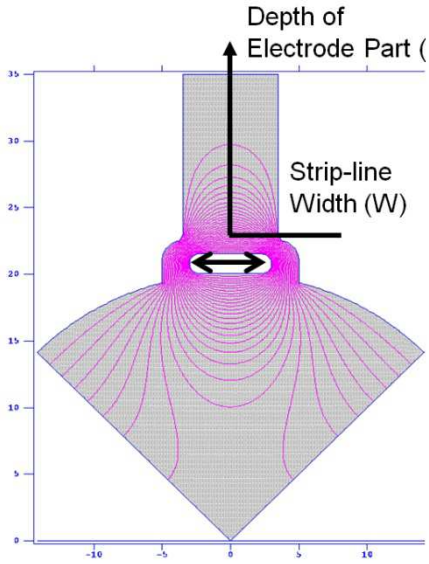

Figure 3-3: Cross-sectional distribution of electrical field around one electrode of stripline BPM.

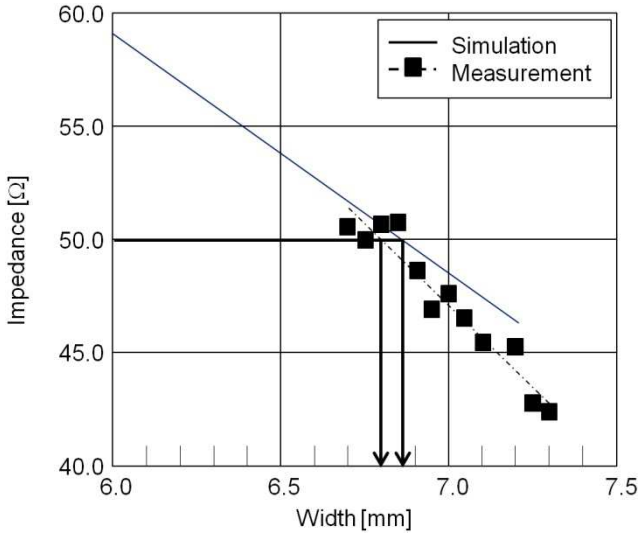

Figure 3-4: Relationship between the width of strip-line electrode and its impedance. Blue line is the estimation relationship taken by simulation, green line is taken by the measurement, and dashed line is fitted line.

Based on the two-dimensional calculation, we fabricated a prototype BPM. To determine the relationship between the width of stripline and its impedance, we used removable electrodes, which range in width from 6.70 to 7.30 mm in 0.05-mm steps,

to cover the estimated width. The measured impedance is also shown in Fig. 3-4 with respect to the stripline width, where the line is estimated from the relationship determined by the simulation, the points with dashed line is the measured impedance. As shown, the measurements were in near agreement with the estimated values around 50 Ω. The estimation showed that the most suitable impedance was a length of 6.86 mm while the measurements indicated that of 6.80 mm. In addition, after the electrode was welded, the remarkable upward shift of the impedance was observed by the small change of the stripline width. About 2 Ω of the impedance was changed by the shift of 1.0 mm in width. We chose 6.85 mm as the width of the electrode, taking into consideration of this upward shift.

3.2 Electronics for Signal Processing

We chose the logarithmic ratio method as a signal processing system because of the advantages of robustness and wide dynamic range. The output signal from the logarithmic amplifier was low-pass filtered for noise reduction.

The beam position derived by the logarithmic processing is [7]

$$x = \frac{1}{S} \cdot (logV_R - logV_L) = \frac{1}{S_x} \cdot log\frac{V_R}{V_L} \propto \frac{1}{S_x} \cdot V_{out} \qquad (3\text{-}4)$$

with the position sensitivity given by S is [dB/mm], and V_R and V_L are induced signal voltages [V] both right and left electrodes respectively. Sensitivity is described as below using a width of stripline electrode W,

$$S = \frac{160}{ln\,10} \times \frac{sin(\phi/2)}{\phi} \times \frac{1}{r} = \frac{160}{ln\,10} \times \frac{W}{2\phi} \times \frac{1}{r}\ . \qquad (3\text{-}5)$$

Designed signal processing scheme is shown in Fig. 3-5. The output can finally be digitized by a slow sampling analog to digital convertor (ADC). In the logarithmic amplifier, low pass filters and differential amplifiers are sequentially combined.

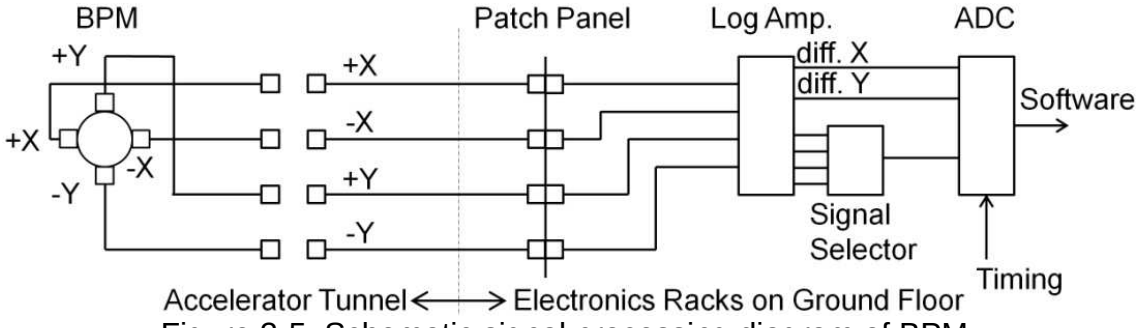

Figure 3-5: Schematic signal processing diagram of BPM.

For the calculation of beam position, for example, vertical position X [mm] can be described below using Eq. (3-4),

$$X = \frac{1}{S} \cdot 20log_{10}\left(\frac{V_R}{V_L}\right) \ . \quad (3\text{-}6)$$

Vertical position can be described by the same formula. The characteristic impedance Z_0 of BPM should be matched to 50 Ω, because the impedance of transmission line is 50 Ω. For example, for typical geometrical parameters of BPM in ACS; r is 20.0 mm (diameter is 40.0 mm) and W is 6.85 mm, S is calculated to be 1.733 [dB/mm]. Assuming 5 mA as the smallest peak beam current for cavity tuning the minimum output voltage was estimated to be 15.2 mV (-23.3 dBm). When the logarithm amplifier is designed using AD8036 produced by Analog Devices Inc., which has a large input margin and output linearity adaptable to the small signal input. For the system of logarithmic amplifier, output voltage V_o [V] can be described as a function of input V_i [V] as follows,

$$V_o = \frac{1}{2} log_{10}\left(\frac{v_i^2/z_0}{10^{-3}} \times \frac{Z_0}{10^{-3}}\right) \ . \quad (3\text{-}7)$$

This can be easily written in

$$V_o = k \cdot P_i + m, \text{ then} \quad (3\text{-}8)$$

$$P_i = \frac{V_o}{k} - \frac{m}{k}$$

here, k and m are characteristic constants and offset of the amplifier.

After fabrication of the logarithm amplifier for the 4-stripline BPM, we measured a relation between inputs and outputs. An example of fitting functions can be obtained as below:

$P_R = 5.015\,V_R - 25.489,\ R^2 = 1.0000$ [dBm],
$P_L = 4.998\,V_L - 25.332,\ R^2 = 1.0000$ [dBm],
$P_T = 4.973\,V_T - 25.392,\ R^2 = 0.9999$ [dBm], and
$P_B = 4.990\,V_B - 25.405,\ R^2 = 1.0000$ [dBm].

After these formulas were plugged into (3-7), we can obtain both horizontal (X) and vertical (Y) position with the equations below.

$$X = \frac{1}{1.733}(5.015V_R - 4.998V_L - 0.157) \quad (3\text{-}9)$$

$$Y = \frac{1}{1.733}(4.973V_T - 4.990V_L + 0.013)$$

In this case, offsets of the center position (when V_R, V_L, V_T, and V_B are equal to 0) is

about 0.091 mm horizontally and 0.008 mm vertically, and these should be considered as the calibration offsets. We confirmed the linearity and offset of all pairs of BPM sensor head and logarithmic amplifier and they were employed with the same combinations. As the result, we could confirm that all offset-values were within ±0.1 mm.

3.3 Calibration

We measured the electrical center position of BPM using a simulated beam signal induced by a thin wire at a stable calibration bench shown in Fig. 3-6. To relate the physical position and its reconstructed position via electrical readout, the following scheme was used in the calibration bench.

· Scanning the wire through the cross section of BPM, horizontally and vertically, and put 324 MHz RF on the wire during scan to simulate the beam.

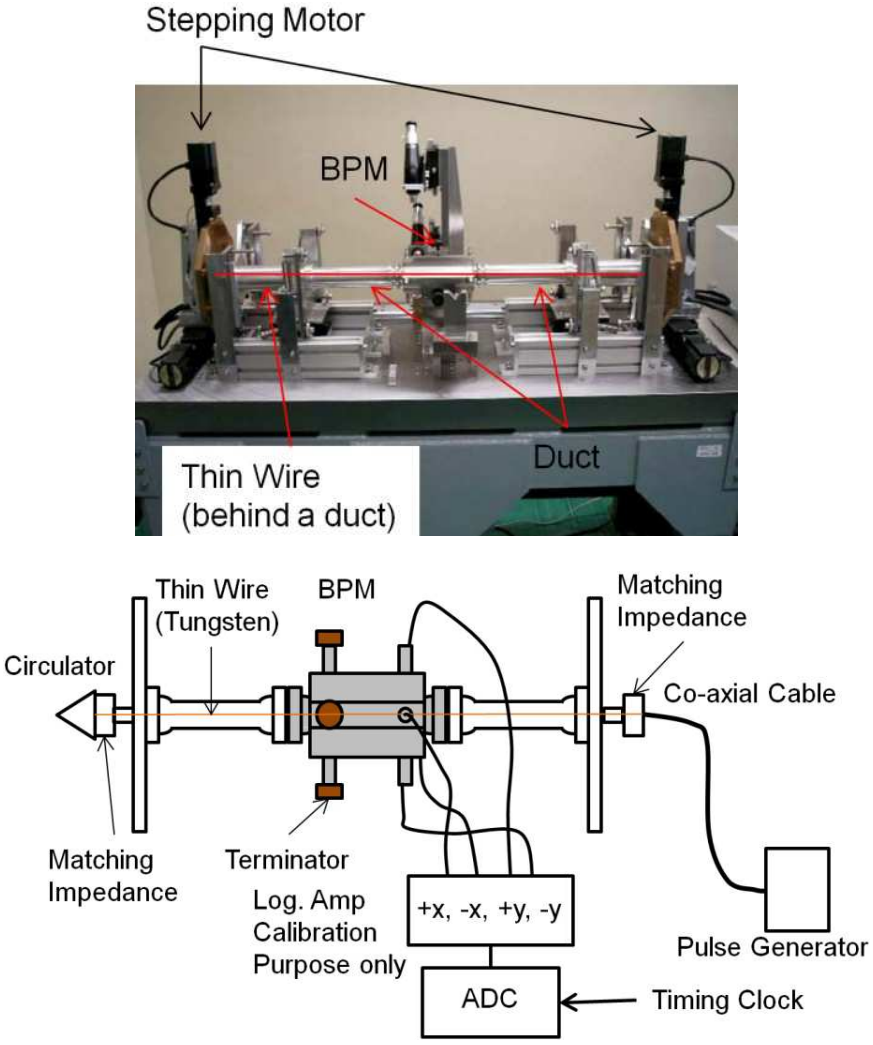

Figure 3-6: Overview of calibration bench for BPM.

· Amplifying the induced voltage logarithmically on 50 Ω load, and taking the ratio between the right and the left stripline for horizontal position, and between the top and the bottom for vertical position.

· Interpolating (analytically fitting) the position among scanned points. As seen in Fig. 3-7, as outer the wire goes (especially for off-XY-axis position) the discrepancy gets larger. The fitting functions need to be optimized especially around the center of the beam duct.

Figure 3-7 shows the relationship between the mechanical and the electrical position. The red points represent the scanning wire position, blue ones are obtained positions. As shown, positions of the mechanical center and the electrical center differ (X, Y) = (30 μm, -50 μm) slightly. We considered the fitting functions are adaptable in a region within 5.0 mm radius.

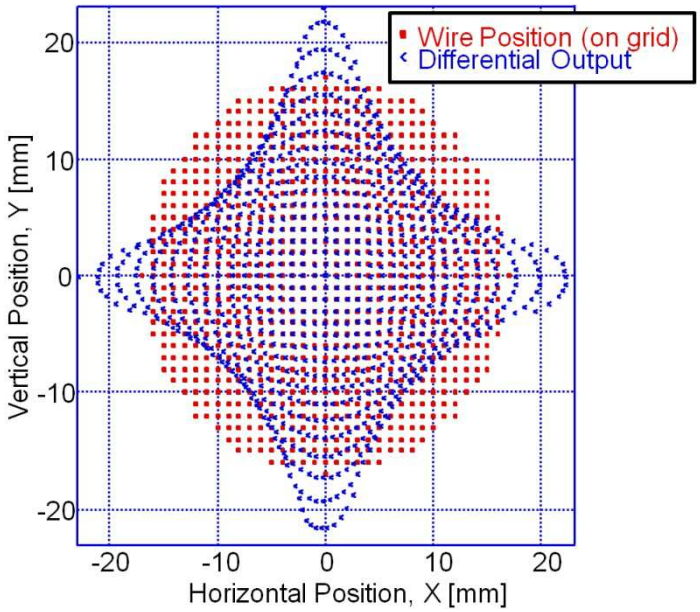

Figure 3-7: Mapping of the BPM position characteristics moving the thin wire. Red dots are wire position on a 1.0 mm square grids. Horizontal position (X) and vertical position (Y) are directly the measured positions by a logarithmic amplifier module.

By the fitting, we could obtain a fifth order fitting function on *x* axis as follows.

$$x = 0.1943m^5 - 0.1185m^4 - 0.3728m^3 + 0.1444m^2 + 5.1229m + 0.125 \qquad (3\text{-}10)$$

Where, *m* is the position by logarithmic amplifier signals. With the same procedure above, the following function was obtained on *y* axis.

$$y = 0.0087n^5 - 0.0921n^4 - 0.0885n^3 + 0.1271n^2 + 5.0874n - 0.1834 \qquad (3\text{-}11)$$

Where, *n* is the obtained vertical position.

We obtained the data to get these fifth order fitting functions of all BPMs, and adopted

them to indicate the operational beam orbit status.

3.4 Installation Accuracy: Beam Based Calibration

We confirmed the alignment offset of BPMs from the center axis of the quadrupole magnets by the conventional beam based calibration (BBC) method, in which responses of beam position to a change of strength of the quadrupole or the steering magnets were examined [8] because the quadrupole magnets were well aligned within 0.1-mm accuracy. This method requires a singlet quadrupole magnet and one of its upstream steering magnets as the tuning knobs. The offset of magnetic center was derived by analyzing the deviation of beam orbit generated by the variation of quadrupole magnet and steering magnet.

The beam orbit was measured using the BPM near the quadrupole magnet and a downstream BPM. Practically, to find a BPM with best response, several downstream BPMs were used for the measurement. We checked the alignment errors from SDTL16 to the end of MEBT2 by this method because the beam line and the magnet layout were completely changed after SDTL16. As the results, the offset was measured to be 18.8-μm within a few 10-μm accuracy [9].

3.5 Longitudinal Profile Measurement by BPMs

Waveforms of accelerated beams were directory observed by the stripline electrode through RF transmission line with about 40 m in length.

We observed the beam waveforms with acceleration up-to the exit of SDTL15, ACS05, and ACS21 as shown in Fig. 3-8. The waveforms taken at ACS10, which is the middle of ACS section, are shown in Fig. 3-9.

Overlapped waveforms with these three modes are shown in Fig. 3-9. In the figure, the length of L is equal to the wavelength of acceleration RF (324 MHz) and the difference of M is depending on the beam energy. The longitudinal RMS size was estimated from the top or the bottom shape of the waveform which was depending on the drift length as listed in Table 3-1. Smallest one was 0.1015 [ps] corresponding to the phase of 11.8^{o}. This was actually too large because the estimated longitudinal size was ~ 3^{o}. We clarified that the mismatching between the BPM electrode and the cable impedance caused the error [2].

By adjusting the BPM electrode impedance, details of the waveform could be observed with time resolution of 0.010 ns which is corresponding to the phase of around 1.0^{o}. We demonstrated that BPMs provide the information on longitudinal beam profile when the characteristic impedance is exactly matched to the transmission line.

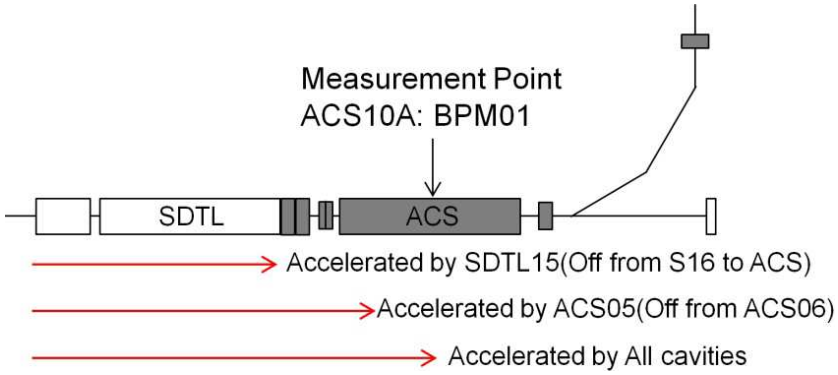

Figure 3-8: Observation of BPM waveforms at ACS10.

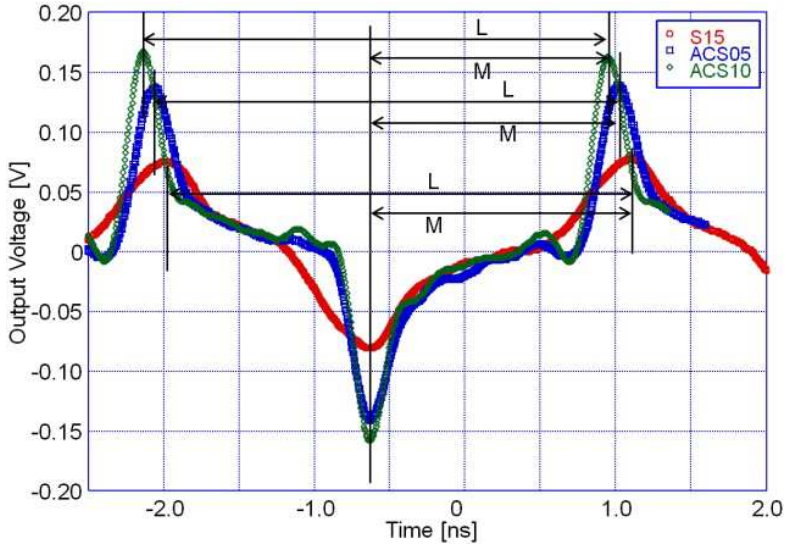

Figure 3-9: Comparison of BPM waveforms.

Table 3-1: Beam size difference with different acceleration mode (20 shots average).

	Average [ns]	Standard Variation
SDTL15	0.2726	0.0101
ACS05	0.1229	0.0057
ACS10	0.1015	0.0024

3.6 Summary

We designed BPMs and installed them in the drift space between ACS cavities to match the parameters of the geometrical restriction. The relative beam velocity around the measurement points for the stripline length, and the characteristic impedance for the stripline width were considered in the design process. Approximately 50 BPMs were fabricated and installed based on the new design. The calibration data were obtained with a scanning wire by supplying 324 MHz RF from which the geometrical center

offset and the calibration functions were derived. The author estimated the center offset was several tens μm with accuracy of 0.1 mm using a test stand. By beam based calibration after installation, we confirmed installation accuracy of 0.02 mm. The total accuracy of BPM was estimated to be less than 0.20 mm for the beam position measurement.

As the stripline electrode is sensitive for the small beam current, we compared the waveforms obtained at varies acceleration patterns, and clarified the differences of the structure. We pointed out that, when the electrode geometries are properly designed, the BPM waveforms can provide useful information on the longitudinal profile of the beam bunch.

References

[1] R. E. Shafer, "Beam Position Monitor Sensitivity for Low-β Beams", *Proceedings of the 1994 International Linac Conference*, pp. 905-907, Tsukuba, Japan, (1994).

[2] P. Forck, "Lecture Notes on Beam Instrumentation and Diagnostics", *Textbook of Joint University Accelerator School*, pp. 9-39, (January - March 2012).

[3] A. Miura, et. al., "Design and Delivery of Beam Monitors for the Energy-upgraded Linac in J-PARC", *Journal of the Korean Physical Society*, **Vol. 66**, No. 3, pp. 364-372, (February 2015).

[4] S. Sato, et. al., "Systematic Calibration of Beam Position Monitor in the High Intensity Proton Accelerator (J-PARC) LINAC", *Proceedings of the 22nd International Linac Conference (LINAC2004)*, **TUP70**, Lubeck, Germany, (2004).

[5] T. Miyao, et. al., "Beam Position Monitors for the ACS Section of the J-PARC Linac", *Proceedings of the 10th European Workshop on Beam Diagnostics and Instrumentation for Particle Accelerators (DIPAC2011)*, **TUPD18**, Hamburg, Germany, (2011).

[6] Poisson Superfish Announcement by LANL Home Page: http://laacg1.lanl.gov/laacg/.

[7] F. D. Wells, et. al., "Log-Ratio Circuit for Beam Position Monitoring", *Proceeding of Particle Accelerator Conference 1991 (PAC91)*, **p. 1139**, San Francisco, USA, (1991) and F. D. Wells, et. al., "Beam Position Monitoring in the 100-MHz to 500-MHz Frequency Range Using the Log-Ratio Technique", *Proceeding of Particle Accelerator Conference 1993 (PAC93)*, **p. 2316**, Washington, USA, (1993).

[8] G. Shen, et al., "Beam Based Alignment of J-PARC Linac", *Proceedings of the 4th Annual Meeting of Particle Accelerator Society of Japan, and the 32nd Linear*

Accelerator Meeting in Japan, **TP60**, Wako Japan, (2007).

[9] A. Miura, et. al., “Beam Monitors for the Commissioning of Energy Upgraded Linac”, *Conference Proceedings of Journal of the Physical Society of Japan (JPS)*, **No. 8**, 011002, (2015).

Chapter 4

Beam Current and Beam Phase Monitor

We have developed transformer type current monitors to measure the beam current and the phase. Commissioning strategies require the time resolution of 50 ns and the signal droop rate less than 1%/μs to the slow current transformer: SCT. Phase accuracy of 6.5^{o} and time resolution of 1 ns are required to the fast current transformer: FCT. In this chapter, we show the design procedures and the performances of the SCT and the FCT fabricated for the ACS section. Finally, we proposed a new interlock system using two SCTs to prevent significant beam loss.

4.1 Beam Current Monitor (SCT) Development

The longest pulse duration we have to monitor is 0.5 ms. Usually conventional current transformers (CTs) are difficult to accommodate to beam current measurements with such a long time duration.

The response function of the CT is described as [1]:

$$V_0 = \frac{RI_b}{N}\frac{j\omega L/R}{1+j\omega L/R-\omega^2 LC} \ . \qquad (4\text{-}1)$$

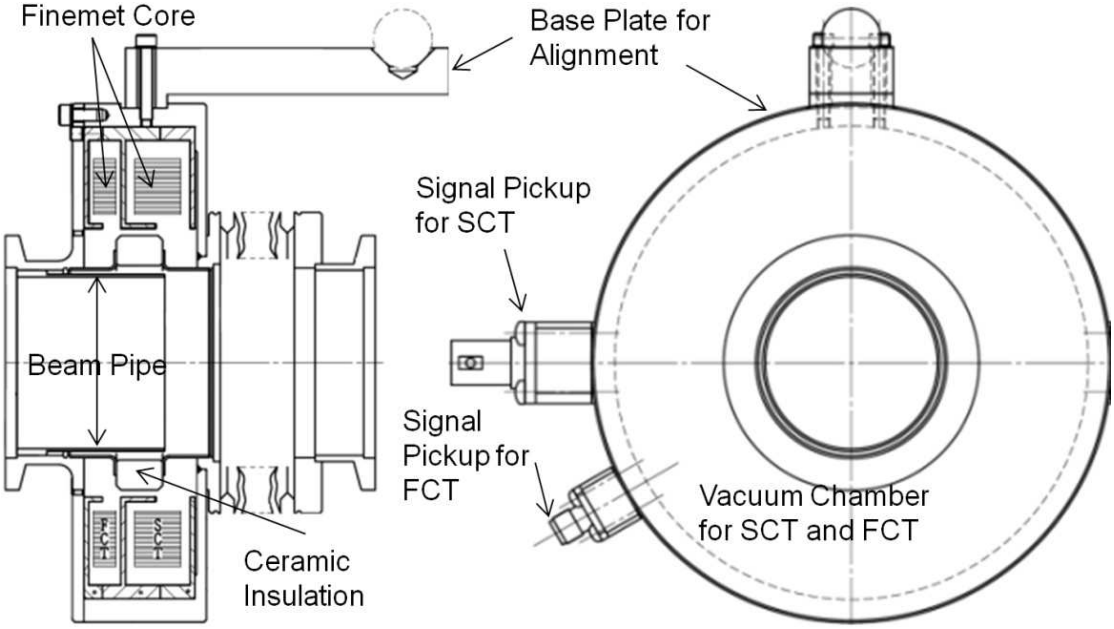

Figure 4-1: Drawing of FCT and SCT monitor chamber.

Where R is a load resister, L is the self-inductance, C is the stray-capacitance, I_b is the beam current, N is the number of coil turns, ω is frequency, and j is imaginably unit. The CT that can tolerate a low cut-off frequency should help us to cover the observation range, because of the temporal structure of the beam bunch. The cut-off limit is represented as $\omega_L = R/L$, and its inverse corresponds to the time constant for the observation limit. The inductance L is restricted, because when we increase L by increase of coil winding, it simultaneously increases the stray-capacitance in the structure.

If the beam current of the intermediate bunch, as well as the macro beam pulse is to be observed, the cut-off frequency of the pulse should be much smaller than that of the intermediate bunch. Thus the time constant should be less than several tens nanoseconds. The beam current monitor (slow current transformer, SCT) we have developed, utilizes a laminated Finemet^{TM} (FT-3M, Hitachi Metals, Ltd.) core, that is made of a Fe-based crystallized metal alloy, with 50-turn windings around the core.

The monitor chamber for the SCT and the beam phase monitor (fast current transformer, FCT) is shown in Fig. 4-1 [2]. The core width of the SCT (10.0 mm) is twice that of the FCT (5.0 mm) because the higher inductance of the wider core provides a higher beam current response and indispensable also for small droop rate which is described as $t_{droop} \sim L/R$. The main role of the ceramic insulation is to prevent the vacuum condition from the degradation due to outgassing from the laminated magnetic core.

The signal processing system of the SCT is shown in Fig. 4-2. The method to reduce ω_L is to develop a low input impedance; R, amplifier. The system has a pre-amplifier and a buffer amplifier. This was installed close to the SCT as possible; otherwise the impedance miss-match causes the reflection of the signal and deforms the current signal. Therefore the pre-amplifier needs to be installed close to the SCT head and it should be protected against the radiation.

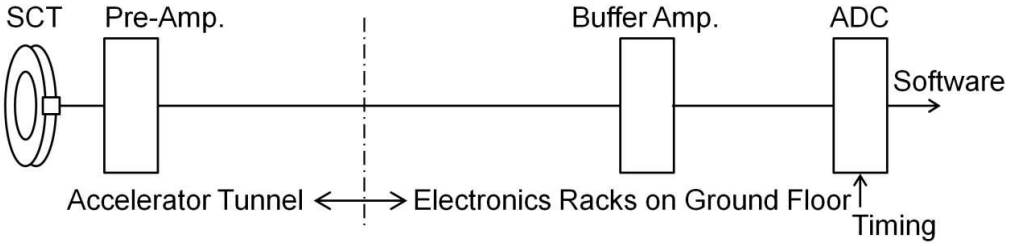

Figure 4-2: The signal processing system of the SCT.

Typical SCT waveform is shown in Fig. 4-3. As shown, the time response of the SCT was estimated to be approximately 20 ns, which is sufficient for the observation of the intermediate bunch clearly. From Fig. 4-3, we also know that the droop rate is <1 %/μs.

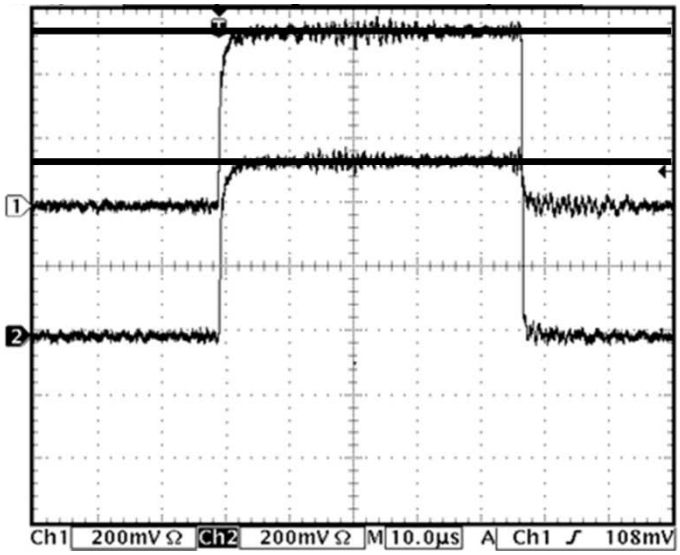

Figure 4-3: Waveforms of the SCTs at different two positions at 5.0-mA operation.

4.2 Beam Phase Monitor (FCT) Development

The beam phase measurement related to the RF signal provides key information to tune the RF cavity. Therefore, the most important information should be extracted from the fundamental RF component of J-PARC linac, namely 324MHz. The beam phase monitor has to have sufficient response to this RF fundamental component.

Conventional current transformers are difficult to extend the high frequency cut-off, $\omega_H=1/CR$, to the RF frequency because of the effect of stray-capacitance (C). The core made of crystallized metal alloy Finemet^{TM} (FT-3M) enabled a single winding structure that extended the frequency response up-to GHz region and realized the beam phase monitor.

A single tern coil was set into the vacuum chamber with SCT core as shown in Fig. 4-1. A flange without a flexible pipe needs to face to the end plates of the cavity because the distance between the FCT pair must be strictly fixed for the TOF measurements.

A new phase detector circuit has been developed, in which the beam signal is directly compared with the reference of 324-MHz signal. A block diagram of the developed phase detector is shown in Fig. 4-4. A direct phase comparator provided a fast response to the phase observations with accuracy within 1.0^o as shown in Fig. 4-5, at a test bench with a time response of less than 3 ns.

The signal processing system of the FCT is shown in Fig. 4-6. An RF reference signal is adjusted exactly to the acceleration RF frequency by using a trombone circuit, to compare it with the beam phase in the phase comparator. In the system of FCT, the RF

signal with the acceleration frequency are transferred to the phase comparator connected by about 30 m-long RF cable. We took the phase shift during the RF transmission as a characteristic offset to the system, because the RF phase is shifted in the transmission line. This offset was considered in the beam energy calculation.

A typical waveform of the FCT is shown in Fig. 4-7 where we measured 100 ms-macro pulse at about 200-MeV beam. The results show that this FCT has a fast time response and can detect the 324 MHz RF signal which corresponds to 3.09 ns.

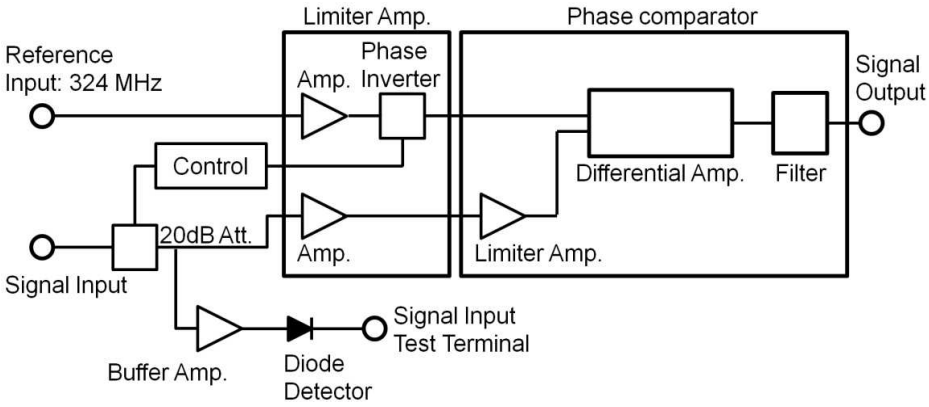

Figure 4-4: Block diagram of developed phase detector.

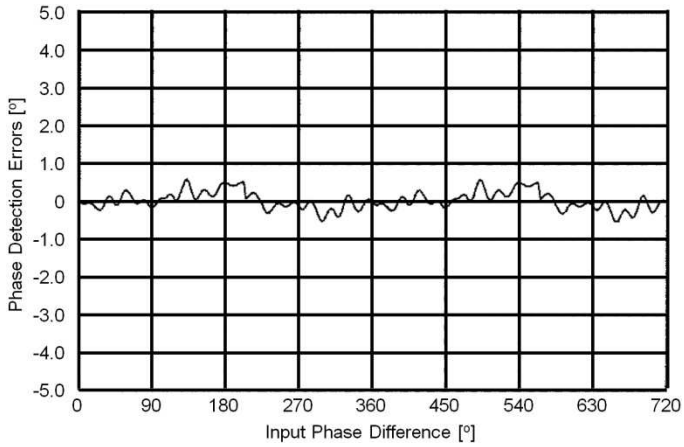

Figure 4-5: Phase detection errors of phase detector.

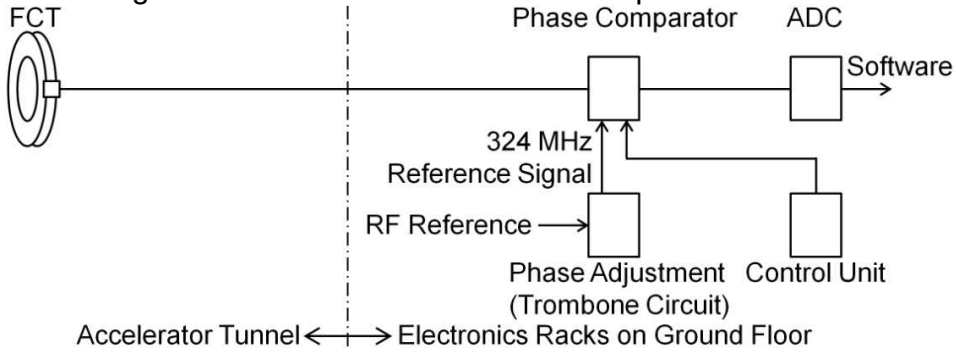

Figure 4-6: The signal processing system of the FCT.

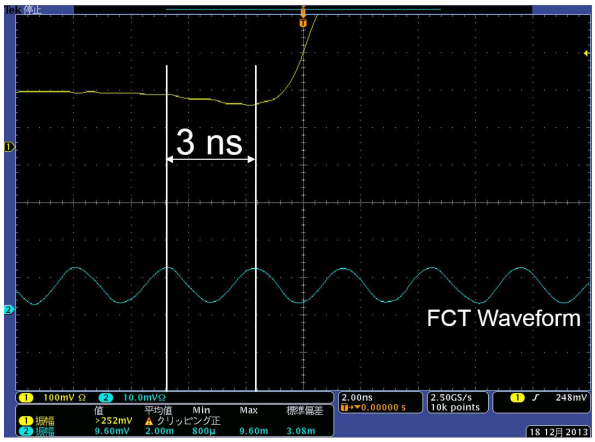

Figure 4-7: Typical Waveform of FCT.

4.3 Bench Test of FCT

Figure 4-8 shows the overview of the test bench to take the characteristic signal response of FCTs. An FCT was set on the bench on the left side. Waveguides of which characteristic impedance matches to 50 Ω with RF conductor with ϕ17 mm diameter were connected to the flanges and the one side (top) is terminated. An RF signal with 0 dBm (1 mW) was supplied from the other side (bottom) using a network analyzer and the reflected signal and output signal from the FCT terminal were measured.

Obtained results are shown in Fig. 4-9 [3]. The inductance of FCT was estimated to be 30.0 [nH], so that the high cut-off frequency is 1.67 [GHz]. The frequency characteristic indicates the achievement of broad dynamic range beyond the third higher harmonics (972MHz) up-to 1.5 GHz. The result means the FCT is available to observe the micro structure of the beam bunch up-to the third higher harmonics region of the upgraded linac.

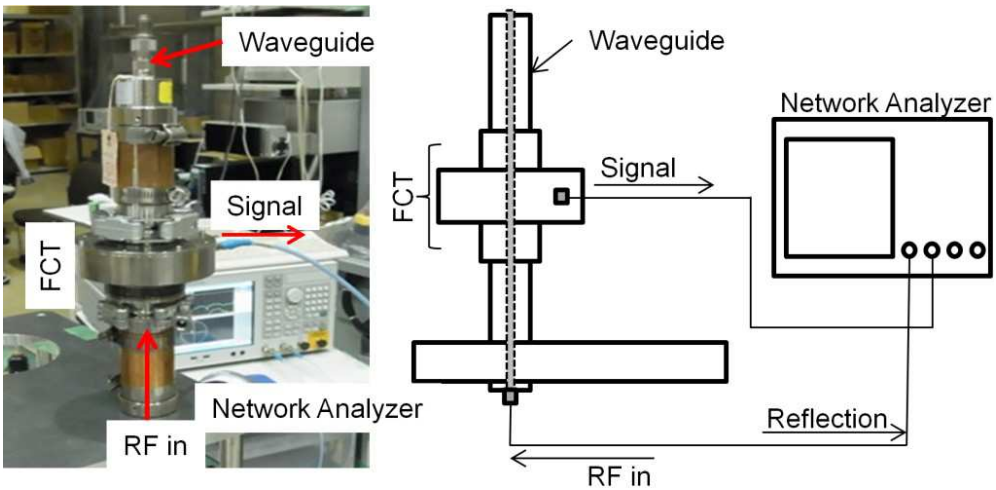

Figure 4-8: Test bench and signal network of characteristic measurement for FCT.

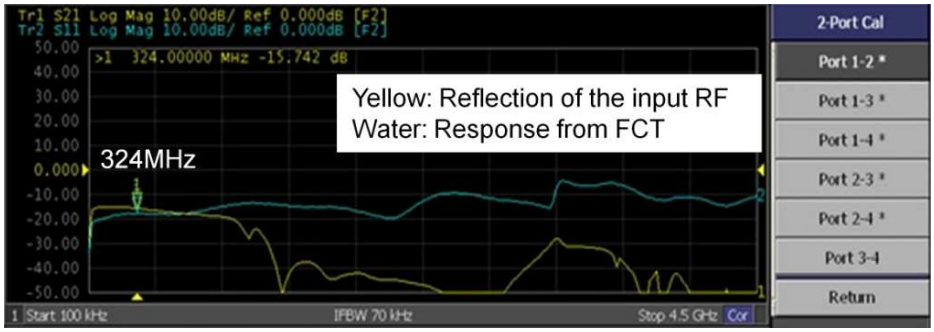

Figure 4-9: Measured performance of FCT.

In principle, BPMs also can be adopted to measure the beam phase. We compared the signal response of the FCT with a BPM at 324 MHz. The BPM was mounted in the same test bench as shown in Fig. 4-10. The measured signal levels were -15.742 dB for FCT and -25.957 dB for BPM as shown in Fig. 4-9 and 4-11. Here, the input signal level from the network analyzer was 0.5 V, and the estimated signal from FCT was 82 mV and that from BPM was 25 mV. The results showed that the FCT is three times sensitive than that of the BPM. Results also showed that the BPM has a good response at 324 MHz, but the characteristic response was periodical in the GHz region [3]. Then an advantage of FCT to the phase measurement was confirmed.

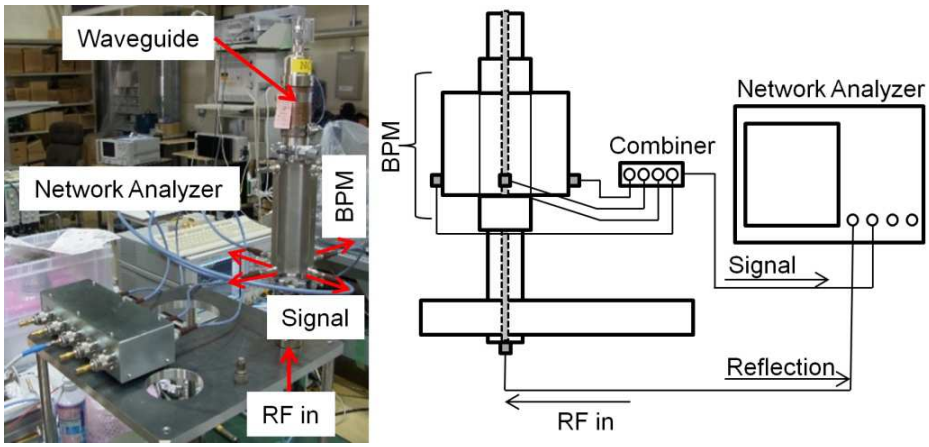

Figure 4-10: Test bench and signal network of characteristic measurement for BPM.

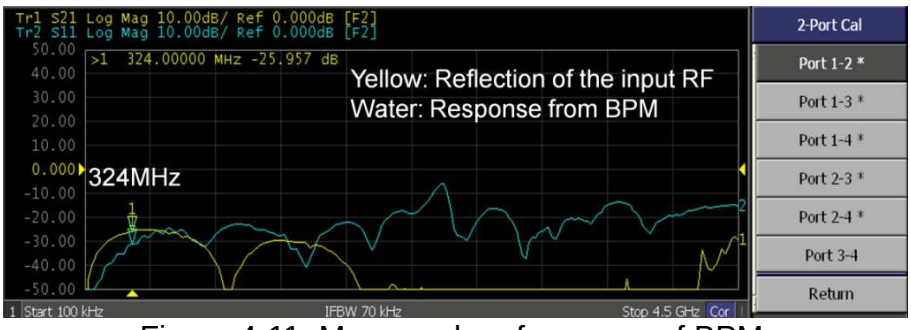

Figure 4-11: Measured performance of BPM.

4.4 Application of SCT for Interlock of Beam Loss at Low-Energy Part

The output beam power of the J-PARC linac has been improved by increasing the acceleration energy and peak beam current. The beam loss is getting serious along with increasing output beam power; however, the beam loss in the front-end region is difficult to detect because of the low level of the radioactive emission. We have developed an interlock system using the beam current monitors to prevent significant material activation. In this system, an electrical circuit measures the beam transmission between the two beam current monitors.

The J-PARC linac has a matching section between the RFQ and the DTLs (see in Fig. 1-3), where 3-MeV beams are monitored and are made profile matching. An ion chamber-type beam loss detector has been employed for the beam loss detection (will be discussed in chapter 7). The beam loss detector has a fast signal response; therefore, we have used this to develop an interlock system to stop the beam operation when an abnormal beam behavior is detected. However, there was no beam loss detector in 3-meV matching section because the energy of radiation generated by 3-MeV beam is not sufficiently high to be detected.

An interlock system was developed that uses some SCTs and a new electrical circuit to measure the beam transmission.

4.4.1 Circuit Design of Beam Transmission Measurement

The new interlock system, which uses SCTs, is named the beam transmission monitor (BTM). The system compares beam current signals from two independent SCTs.

A schematic diagram of the system configuration of the BTM is shown in Fig. 4-12. The system comprises two SCTs, and a signal processing circuit for the BTM shown in gray. Pre-amplifiers are usually used for continual user operation and their sensitivity are tuned to 0.10 V/mA. The buffer amplifier has four channels per module, with two channels connected to the digitizer (one for both waveform-outputs, 1 and 2) during the beam operation, and the other two channels used by the BTM. The BTM circuit has six output terminals, as shown in Fig. 4-12.

The signal processing flow in the BTM is shown in Fig. 4-13. It has two input terminals for the two signals coming from the two independent SCTs. Just after the signals are inputted into the terminals, gain adjustment knobs amplify the input signals independently. These can be tuned by observing the low beam current signals (outputs 1 and 2). To detect small beam losses, the beam current signals are

integrated with a gate signal that covers an entire beam pulse. The rise of the gate signal pulse plays a significant role in the trigger of the integration, whereas the flank plays a significant role in the reset of the integration. After integration, which can be observed in outputs 3 and 4, the difference, which should be small, is usually taken by the two integrated inputs. The difference can be observed at the output 5 terminal and it is integrated again into the circuit. The final integrated differential signal can be observed in output 6.

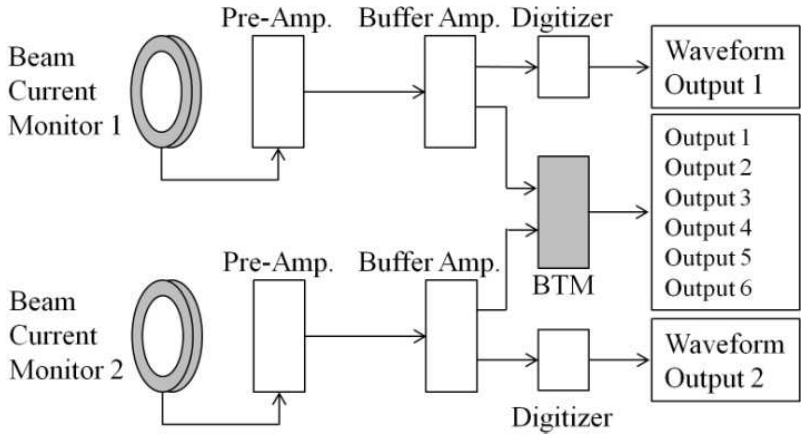

Figure 4-12: System Configuration of the beam transmission measurement.

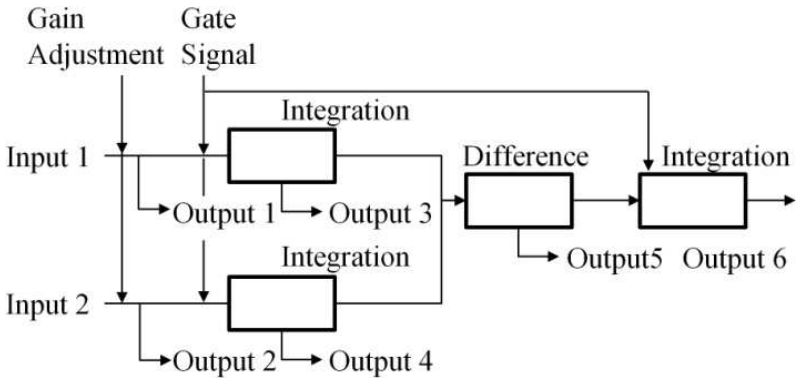

Figure 4-13: Block Diagram of the signal processing flow in the beam transmission monitor (BTM) circuit.

Figure 4-14 shows the estimated waveform at each output terminal. Two rectangular simulated beam input pulses are assumed with different wave heights at inputs 1 and 2. When the current signal to input 1 is from upstream of input 2 and the input gain is adjusted, the wave height of the current signal to input 2 is smaller than that of input 1. After inputs 1 and 2 are integrated during the gate period, outputs 3 and 4 are obtained. The waveforms of outputs 3 and 4 are proportionally increased between

beam-on and beam-off, and the highest peak is held until the reset signal. The integrated signals are subtracted and the result is output 5. Furthermore, this signal proportionally increases in a beam period. The differential voltage is accumulated over time, with the integrated difference being quadratically increased. During the beam period, the differential signal proportionally increases until the reset signal.

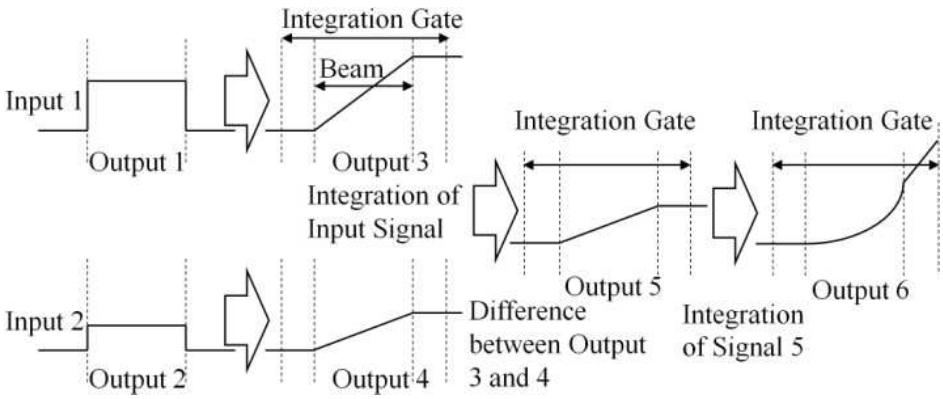

Figure 4-14: Waveforms during BTM signal processing.

4.4.2 System Test

There is a matching section between the RFQ and the DTLs, where the beam energy is 3 MeV, and there are five SCTs in this section. As all the beams are considered to be lost in the DTL, we focused on the beam current monitors upstream and downstream of the DTL. Therefore, input 1 was occupied by the beam current signal from the last MEBT1 and input 2 was for the last DTL. In the test operation, a beam with a 30-mA peak current and a 100-μs pulse length was used. The integration gate covered the beam pulse with a width of 2 ms from 50 μs preceding the current rise.

When the beam is operated with tuned beam lines, the beam loss in the DTL is assumed to be small. When the input currents are the same, the trends of inputs 1 and 2 as well as those of outputs 3 and 4 are the same. Therefore, the subtraction of outputs 3 and 4 gives a value of zero for output 5, which will result in no signal in output 6.

Using carefully tuned beam line, inputs 1 and 2 were maintained with the same pulse height by the gain adjustment knobs for the input signals. The waveforms of output 1 (raw output of input 1), 2 (raw output of input 2), 5 (difference of integration between 3 and 4), and 6 (final integration of the difference 5) are shown in Fig. 4-15. Figure 4-16 shows the waveforms of outputs 3 (integration of input 1), 4 (integration of input 2), 5, and 6. Integration of the input pulses, which started by the gate pulse, shows the same trends for outputs 3 and 4, with the difference between (output 5) of

outputs 3 and 4 then being close to zero. Finally, the integration (output 6) of output 5 was shown to be almost zero.

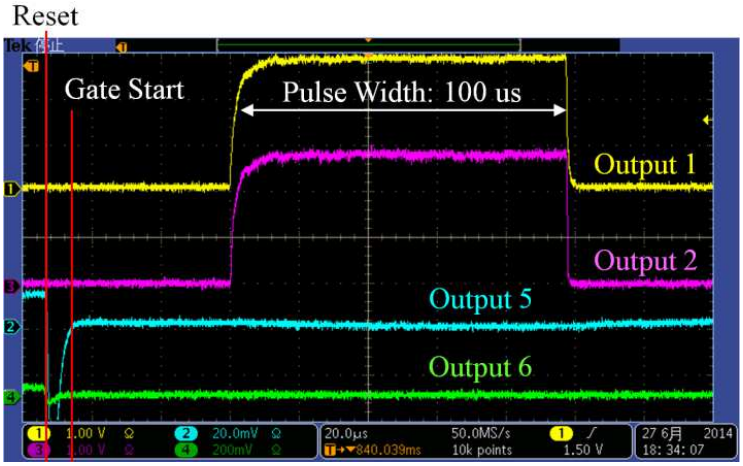

Figure 4-15: Waveforms of outputs 1, 2, 5, and 6 when pulses with same heights are input. The horizontal axis scale is 20 μs/division.

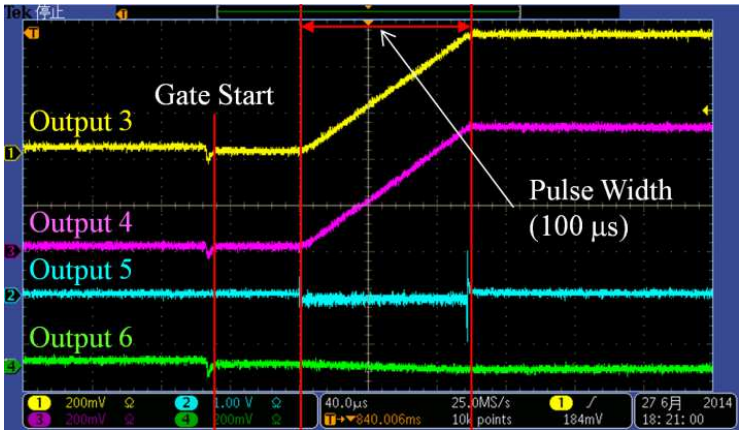

Figure 4-16: Waveforms of outputs 3, 4, 5, and 6. The horizontal axis scale is 40 μs/div.

We assumed a case in which the entire beam was lost in the DTL. Input 1 remained; however, input 2 was suspended from producing any signals. Figure 4-17 shows the waveforms of the outputs 1, 3, 5, and 6 at 400 μs/div along the horizontal axis. Output 3 is proportionally integrated and the difference of output 3 and input 2 (actually no signal input) was also proportionally integrated and the peak value was maintained until the reset signal. While the beam was passing, the proportional difference was integrated quadratically.

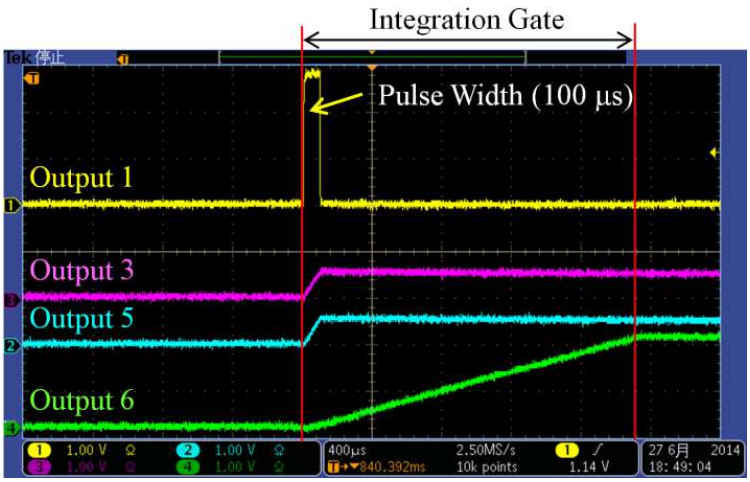

Figure 4-17: Waveforms of outputs 1, 3, 5, and 6 for beam loss in the DTL section. The horizontal axis scale is 400 μs/div.

After the beam had passed, the integration of the differential signal was proportionally increased due to the remainder of the peak value. Figure 4-18 shows the extensions of the waveforms of outputs 3, 4, 5, and 6 around the pulse duration. A quadratic increase of output 6 was observed.

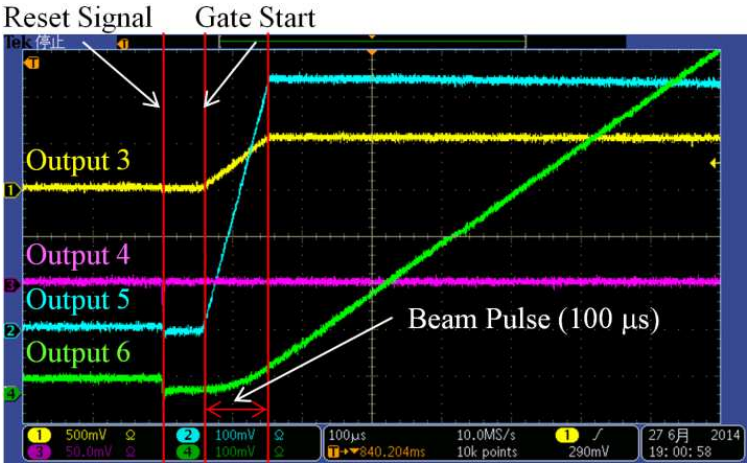

Figure 4-18: Waveforms of outputs 3, 4, 5, and 6 with beam loss in the DTL section. The horizontal axis scale is 100 μs/div.

We tested the beam loss detection system in the case of normal operation with beam loss occurring in the front-end section (DTL) and confirmed that the signal outputs of all the terminals worked as estimated.

The performance of the BTM was confirmed by obtaining the maximum output of the integrated difference. In the interlock level, the worst case is that provides the maximum output from output 6, because it is sensitive to the small difference

between outputs 1 and 2. We decided a threshold value which suspends the beam operation alarm. The threshold was set to be a half of the maximum value, which implies that the alarm is triggered later than halfway through the pulse. The signal rise of output 6 is slow because it increases quadratically in the case of ordinary beam loss. Nevertheless, we also use output 5 for alarming because the signal from output 5 provides quicker response than that from output 6. The system was confirmed to be successful when used in actual beam operations.

4.4.3 Result of Interlock System Development

A new interlock system using beam current monitors is proposed. We developed an electrical circuit to measure the beam transmission using two beam current monitors for the system. We established the new system and tested it using an actual beam in two typical cases. Based on the results obtained in all the cases of beam loss, we obtained the worst signal response, which will be used as a threshold for the interlock.

Fortunately, we haven't had any interlock by this system, however the BTM circuit can be adopted to another interlock system by the connection of the other beam monitors. We successfully developed useful electrical circuit to be applied for various interlock system.

4.5 Summary

The designs and performances of SCT and FCT were described in this chapter. The time constant of SCT is required to be less than 50 ns and the signal droop rate is less than 1%/μs. The waveform of beam currents suggested that the performance of SCT achieved these requirements. In the beam operation, we derived a calibration function to the output voltages (V_{out}) of SCT is V_{out} [V]=0.01$\times I_{in}$ [mA] as shown in Fig. 4-19.

Phase accuracy of 6.5^{o} and time constant of 1 ns are required by the commissioning strategies. We have developed fast current transformer FCT composed of Finemet^{TM} core and one-turn configuration. The resolution of FCT was less than 1 ns and the phase accuracy of FCT was estimated to be less than 1.0^{o} by using a signal processing based on phase comparator. Tuning and systematic errors of the actual phase measurement will be discussed in Chapter 9.

Finally, a new interlock system using SCTs which the author proposed and developed was introduced. It is getting attractive all over the world, because the BTM provides the new system which can be adopted to the place where it is difficult to detect the beam

loss signal. In addition, some applied systems using the BTM are proposed, because it can be adopted for comparing two different signals.

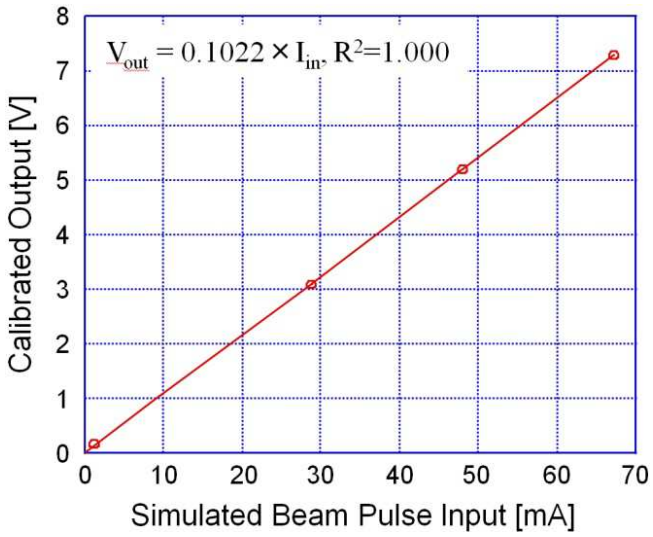

Figure 4-19: Linear trend of SCT for calibration.

References

[1] P. Forck, "Lecture Notes on Beam Instrumentation and Diagnostics", *Textbook of Joint University Accelerator School*, January - March 2012, pp. 9-39.

[2] A. Miura, et. al., "Design and Delivery of Beam Monitors for the Energy-upgraded Linac in J-PARC", *Journal of the Korean Physical Society*, **Vol. 66**, No. 3, February 2015, pp. 364−372.

[3] A. Miura, et. al., "Design and Performances of Phase Monitor in J-PARC Linac", *Proceedings of the 26th International Linear Accelerator Conference (LINAC2012)*, **TUPB102**, Tel-Aviv, Israel, (2012).

[4] A. Miura, et. al., "Interlock of Beam Loss at Low Energy Part of J-PARC Linac", *Proceedings of the 15th International Conference on Accelerator and Large Experimental Control Systems (ICALEPCS2015) conference*, **MOPGF137**, Melbourne, Australia, (2015).

Chapter 5

Transverse Profile Monitor (Wire Scanner Monitor)

Wire scanner monitors (WSMs) are reliably operated in many accelerator facilities around the world. Although 10^{+2} is usual dynamic range for evaluating the RMS beam size, combining two different profile measurements or employing another profile monitor based on a different principle would enable a wider dynamic range to observe the beam halo [1-3]. The main role of the WSM is to measure the RMS beam size for transverse matching between the quadrupole magnets in J-PARC linac. A dynamic range of 10^{+2} is sufficient to measure the RMS beam size for the matching procedure in J-PARC linac [4, 5]; however, our goal is to develop much more sensitive WSMs for the linac to simultaneously observe the beam halo. Because of the high-power level of J-PARC linac, suppressing a halo around the beam core is considered critical for stable operation. For example, a beam halo reportedly appeared at the location of a mismatched magnet and/or an improperly installed cavity [6]. The beam intensity loss became significant when the beam current was increased. We estimated that the intensity of the beam halo of the matched beam is less than 10^{-3} of the beam core. Therefore, we set the target of our WSM to have a dynamic range of 10^{+4}.

The transverse beam size is estimated typically to be 2 to 3 mm in RMS. Then, a 0.1-mm position resolution is usually required to monitor the beam profile.

The other purpose of the WSM is to confirm the available beam current. While our beam current monitor (slow current transformers, SCT) can monitor the beam current of J-PARC linac (5 mA) with an accuracy of 0.1 mA, WSM can measure a smaller beam current, because the wire directly measures the charge flux of the beam. We expect that the wide dynamic range of the WSM can estimate the beam extinction rate deflected by RF chopper cavity by monitoring the evolution of the beam current.

5.1 System Configuration

There are eight matching sections in the linac. The most upstream point is the matching section between RFQ and DTL with a beam energy of 3.0 MeV. Other matching sections are the upstream of the separated-type DTL section (SDTL), the annular-ring coupled structure linac section (ACS), and the beam transport line from linac to 3-GeV

rapid cycling synchrotron (L3BT). Downstream of L3BT includes the arc, a vertical collimator, a horizontal collimator, and an injection sections, as shown in Fig. 5-1.

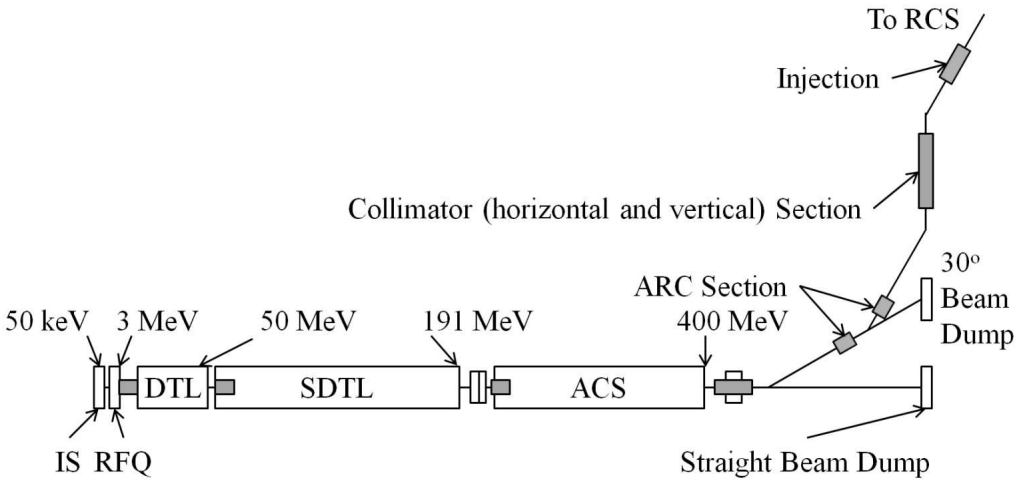

Figure 5-1: Transverse matching points of linac. Gray squares are matching points.

The WSM consists of a beam measurement head (wires), a bias voltage supplier, a stepping motor unit and electrical circuits to treat the signals, and a control system. Figure 5-2 and 5-3 show the structure of the WSM, and Figs. 5-3(a) and (b) are the head and the wire frame of the WSM, respectively. Because the wires are connected on a head 45° to the horizontal axis, both horizontal and vertical profiles can be measured in a single stroke. The wire head frame was produced from stainless steel to prevent charging by secondary electron capture. Based on thermal calculations described in the following section, a 30 μm diameter tungsten wire was selected and connected to the frame to monitor beams over 50-MeV energy. In addition, we placed 2.0-mm thick carbon plates on a frame for beam collimation at L3BT, as shown in Fig. 5-4(b). The carbon plate was considered sensitive because it has a wide surface for detection.

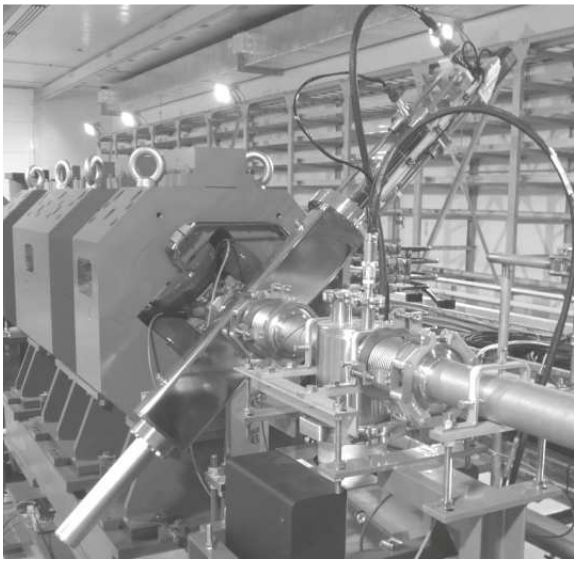

Figure 5-2: Whole view photo of WSM, with head and wire frame.

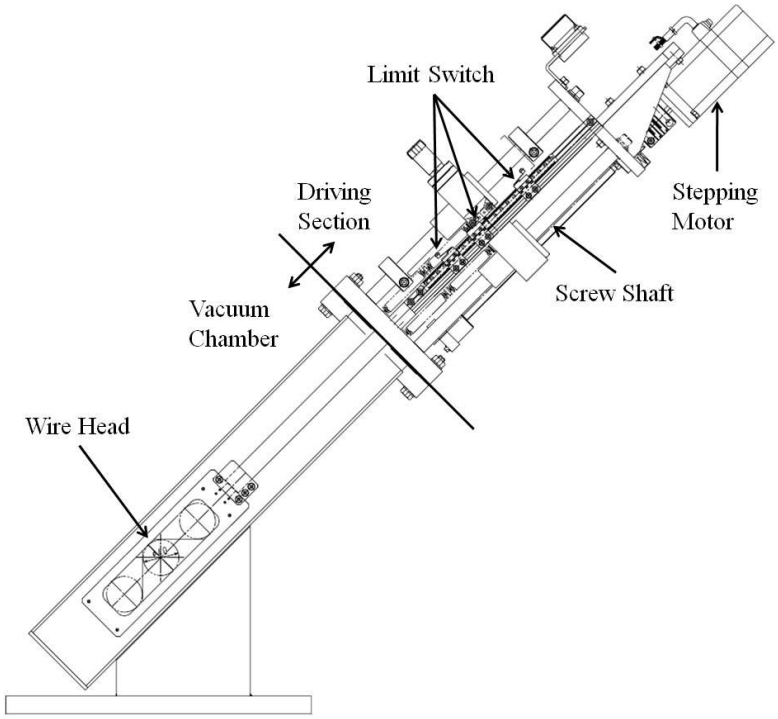

Figure 5-3: Structure of the wire scanner monitor.

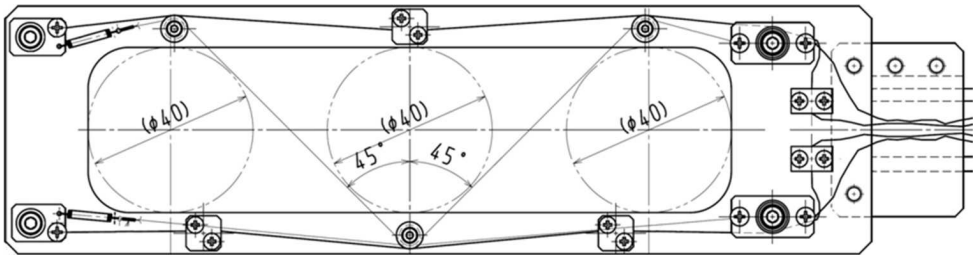

Figure 5-4(a): Example WSM head and wire frames in the ACS section.

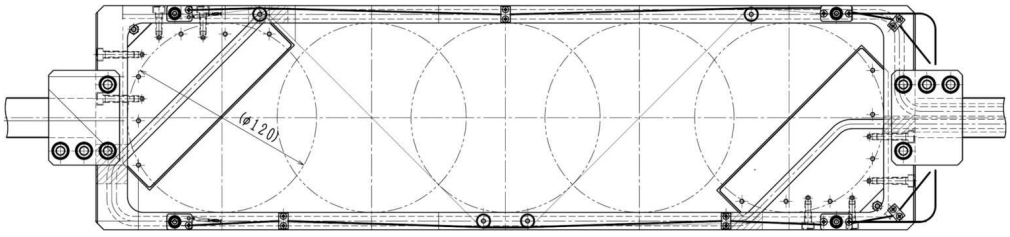

Figure 5-4(b): Example WSM head and wire frames in the L3BT section.

When a negative ion beam passes through the wire, electrons remain inside the wire. Emission of secondary electrons creates a counter current that results in a non-negligible signal. A beam profile with a voltage bias ranging from −240 V to +240V was measured

in the beam test. The optimal bias for the profile monitor was +20 to +60 V [7]. When no bias was applied, nearly the same profile was obtained. We used the WSM for matching the RMS beam size and found that the secondary electron effects are usually negligible, except by the beam tail component.

The stepping motor drive we employed was obtained commercially. The drive system could remotely control the wire head from the ground floor with 0.05 mm steps. We designed a signal amplifying unit to increase the sensitivity for less than 50 ns signal in order to observe a beam pulse with a width of 100 ms; the signal was enhanced by a factor of 3 to 300.

The WSM signal sequence is shown in Fig. 5-5. Signal cables are connected to the wires that are funneled through a shaft pipe. The signals are separated into BNC connectors to the pre-amplifiers which are locally installed around WSM.

The WSM control system is shown in Fig. 5-6. The motor step can be controlled remotely from the electronics racks, which are 35 m to 120 m at the farthest point from the WSM.

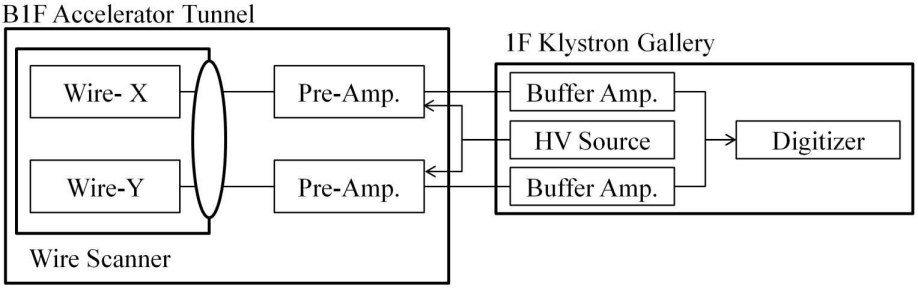

Figure 5-5: Signal sequence of the wire scanner monitor. Here, wire-X and wire-y are the horizontal and vertical wires respectively.

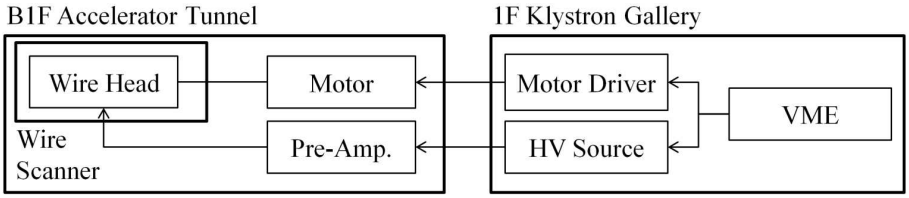

Figure 5-6: Control system of the wire scanner monitor. Here, VME is a control unit.

5.2 Design Calculation

5.2.1 Signal Generation in Wire

Negative hydrogen ion (H^-) beams are accelerated in the J-PARC linac. Collisions

between the H^- beams and a wire can lead to the following signal sources [8]:
(1) negative current by electron deposition to the wire,
(2) positive current by proton deposition to the wire, and
(3) positive current by the secondary electron emission.
When high energy electrons and protons impact a thin wire, both electrons and protons penetrate the wire. When they have sufficient energy to pass through the wire, the signal is mainly derived from process (3). Since the energy of electrons is $m_e/(m_p + m_e)$ of the protons, they remain in the wire. Here, the signal is generated by processes (2) and the (3). When both electrons and protons are captured in the wire, all mechanisms contribute to the signal.
We estimated the contribution of each mechanism using the beam stopping power formula provided by the Bethe-Bloch model. The formula gives the energy deposition density as a function of the charge and speed of the particles, and the material properties of the target [9]:

$$-\frac{dE}{dx} = \frac{4\pi r_e^2 m_e c^2 N_0 Ze}{A\beta^2}\left[ln\frac{2m_e c^2\beta^2}{(1-\beta^2)I^2} - \beta^2\right] . \quad (5\text{-}1)$$

Here, dE/dx is the beam stopping power, x is the thickness of material traversed [g/cm^2], N_0 is Avogadro's number, Z and A are atomic and mass numbers of the material, Z_e and $v = \beta c$ are the charge and the velocity of the moving particle, m_e is the electron mass, r_e = 2.8 fm is the classical electron radius, and I is an effective atomic ionization potential as 13.5 eV in hydrogen.
An important point is that dE/dx is much larger for lower energy particles, which means that for low-energy beams, larger signals are expected. Moreover, the thermal load becomes more important for low energy particles.
We calculated the secondary electron yield from the mechanism (3) using the following expression:

$$Y = \left(\frac{Pd_s}{E_k}\right)\cdot\frac{dE}{dx} , \quad (5\text{-}2)$$

where dE/dx is provided by the national institute of standards and technology (NIST) [10], d_s is the average depth at which the secondary electrons are located, E_k is the average amount of kinetic energy lost by an ion per ionization produced in the wire, and P is the probability.
We used P=1/2, d_s=1nm, E*=25eV [11], and calculated the stopping power. We obtained the stopping power of electrons and that protons in tungsten (W), as shown in Figs. 5-7(a) and (b). The electron stopping powers in tungsten were estimated to

be 2.09 and 1.49 [MeV cm^2/g] at 0.098 and 0.217 MeV, respectively, which correspond to 181 and 400 MeV of protons. Similarly, the stopping powers of protons in tungsten were 2.56 [MeV cm^2/g] at 181 MeV and 1.63 [MeV cm^2/g] at 400 MeV.

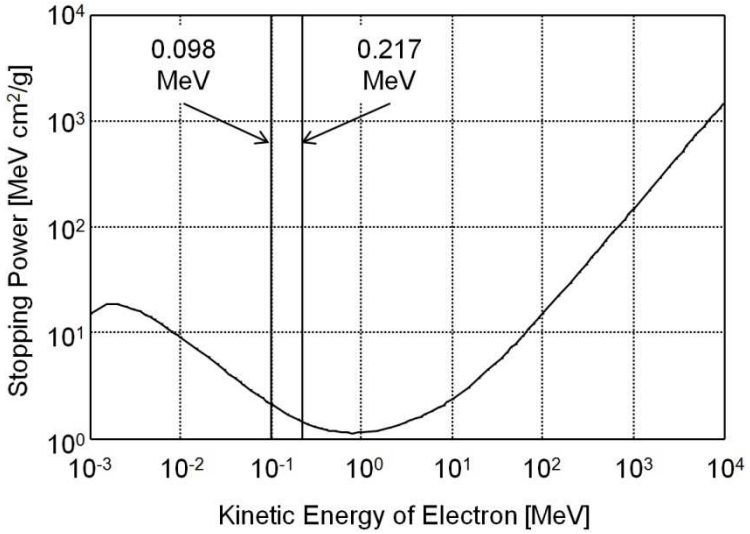

Figure 5-7(a): Stopping power of electron beam in tungsten [10].

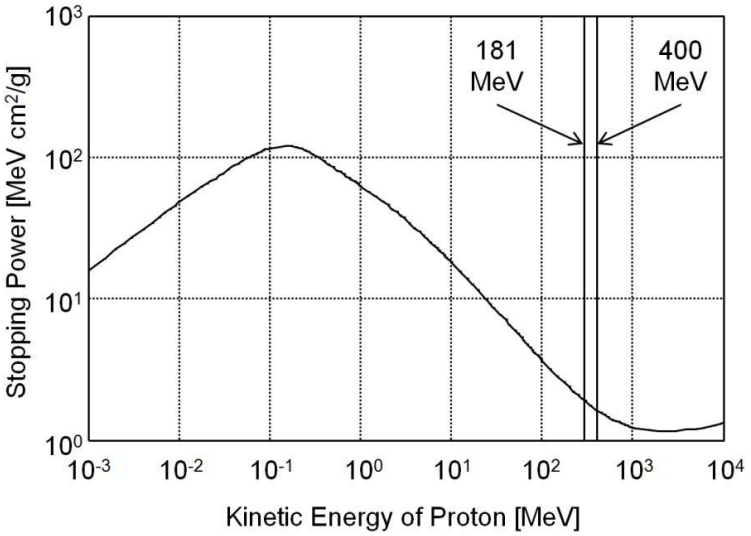

Figure 5-7(b): Stopping power of proton beam in tungsten [10].

The electrical signal of WSM was derived using contributions from mechanisms (1), (2), and (3), which are determined on the basis of the energy deposition of electrons and protons in tungsten, and the generated secondary electrons. Subsequently, the WSM signal can be described by the following equation:

$$I = 2V\rho\left(\frac{dE_e}{dx}\right)_e + V\rho\left(\frac{dE_p}{dx}\right)_p - V\rho Y \ . \qquad (5\text{-}3)$$

Where V is an effective volume in which there are interactions between beam particles and the wire. If the calculated value is negative, the signal is governed by electron deposition with only a small emission of secondary electrons.

Generated signal current by the interactions between the beam particles and the wire is calculated and shown in Fig. 5-8. In the calculation, we assumed the beam energy was 191 MeV at a transverse RMS beam size of 2.0 mm. The wire diameter and the peak beam current were considered as parameters. The results predicted that a milli-ampere-order negative signal current can be obtained when a 50 μm wire for both 191MeV beam interacts. As shown in Fig. 5-8, the electrons pass through wires when the diameter is thinner than 17 μm. To stop the electrons and provide greater signal, wires over 18 μm diameter are needed. Namely, the signal source is from electron deposition without excess secondary electrons.

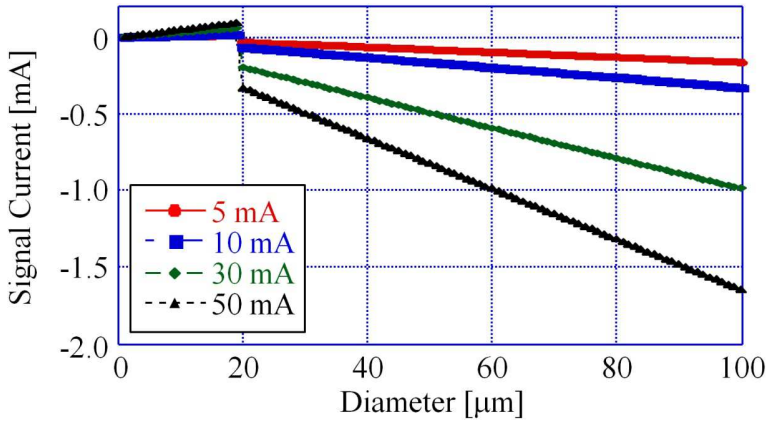

Figure 5-8: WSM current signal by H^- beam collisions with transverse rms size of 2.0 mm for beam energy of 191 MeV.

5.2.2 Thermal Stress

Using the energy deposition derived from Eq. (1) and the radiation loss from the wire surface, we calculated the wire temperature. Prior to estimating the temperature, we estimated the energy deposition as a function of wire diameter and beam current.

As suggested above, tungsten is the most compatible material for the WSM wire because of its high melting point (3422 ºC). The estimated power deposition by the 191-MeV beam is shown in Fig. 5-9.

The equation for heat valance of the wire is given by the following:

$$\frac{dQ}{dt} = Q_{beam} - \sigma(T_{wire}^4 - T_0^4) \ , \qquad (5\text{-}4)$$

where Q_{beam} is the power deposition and the second term is the radiation power flow. Since this equation does not include a thermal conductivity term, it provides only a conservative temperature estimation.

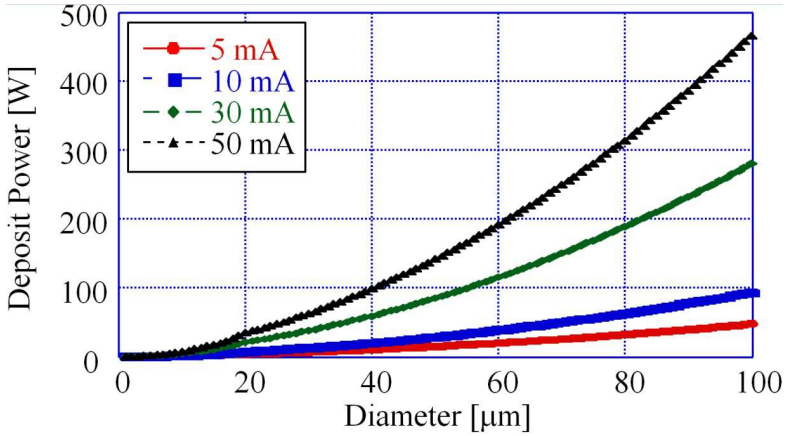

Figure 5-9: Power deposition of H^- beams with 2.0 mm rms size in tungsten wire at a beam energy of 191 MeV.

The result is shown in Fig. 5-10, where (a) is the temperature evolution due to the beam loading at 30 mA and (b) is that at 50 mA. A full beam was considered in the calculation, namely, a beam with 400-MeV energy, 30 and 50-mA peak current, 50-Hz repetition, 0.5 ms macro pulse width, and 56% duty factor. In the figure, the small temperature fluctuation is due to a cyclic power input with 50-Hz repetition. Since the melting point of tungsten is 3680 K, this result indicates that 30-μm tungsten would not be heated to the temperature limit. Based on the calculation, we employed WSMs composed of 30-μm tungsten wires for the 400-MeV linac. Since the line expansion was estimated to be about 5.0 mm when the temperature of a 0.4-m wire was increased to 3000 K, we used a spring support to apply about hundred newton (N) of tension to the wire.

Previously, WSMs installed in the downstream of L3BT have been exposed to a 181-MeV beam before the upgrade. These WSMs are presently exposed to a 400-MeV beam. As shown in Fig. 5-7(a), the beam stopping power is predicted to become smaller with increasing beam energy. We then concluded that the thermal stress induced by the energy deposition is relaxed in the upgraded accelerator.

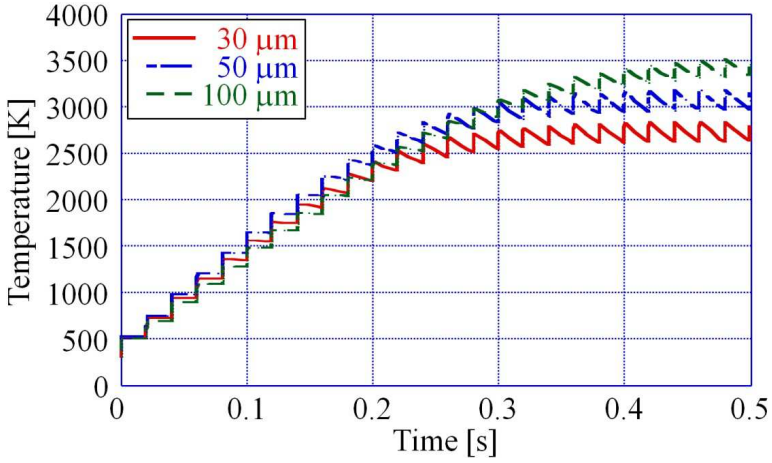

(a) For peak beam current of 30 mA.

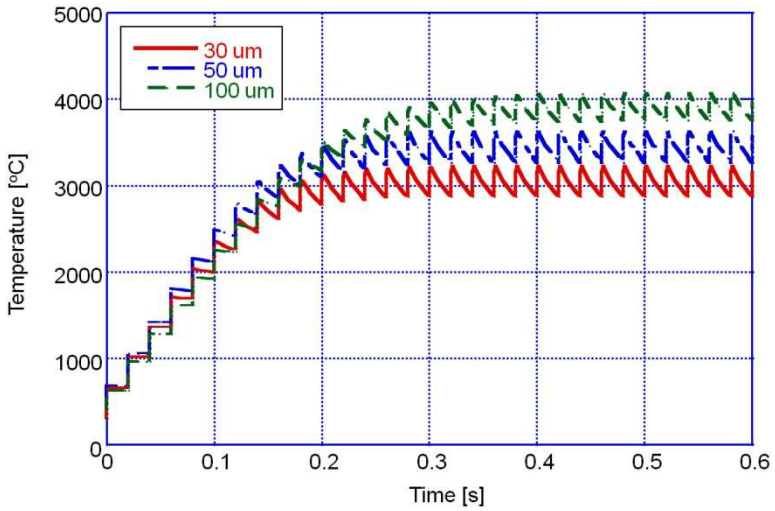

(b) For peak beam current of 50 mA.

Figure 5-10: Temperature evolution by beam loading with energy of 400 MeV, repetition 50 Hz, macro pulse width 500 μs, and duty factor 56 %.

5.3 Beam Profile Measurement

We measured the profiles and background levels using beams with 181-MeV energy, 15-mA peak current, 500-μs pulse length at the ACS section and the beam line to the straight beam dump. We took the beam profiles at ACS02 and averaged the data for 5 shots. A vertical profile is shown in Fig. 5-11. From the beam profiles, we calculated the beam size and the emittance assuming a Gaussian distribution [12].

The background noise was acquired at ACS02 and the result is shown in Fig. 5-12, which indicates that the background noise is less than 10^{-4}. By averaging all of the

background noise using a least-squares method, we determined that the sensitivities of horizontal and vertical signals are 1.65×10^{-5} and 1.67×10^{-5}, respectively. By comparing the background data presented in Fig. 11, we estimated that the WSM dynamic range is more than 10^{+4} and the signals at a level of 10^{-4} are from the beam tail. As shown, we achieved sufficient WSM sensitivity in order to observe the beam dynamics. We emphasize that this is due to the large electron–tungsten yield and the optimally designed amplification system.

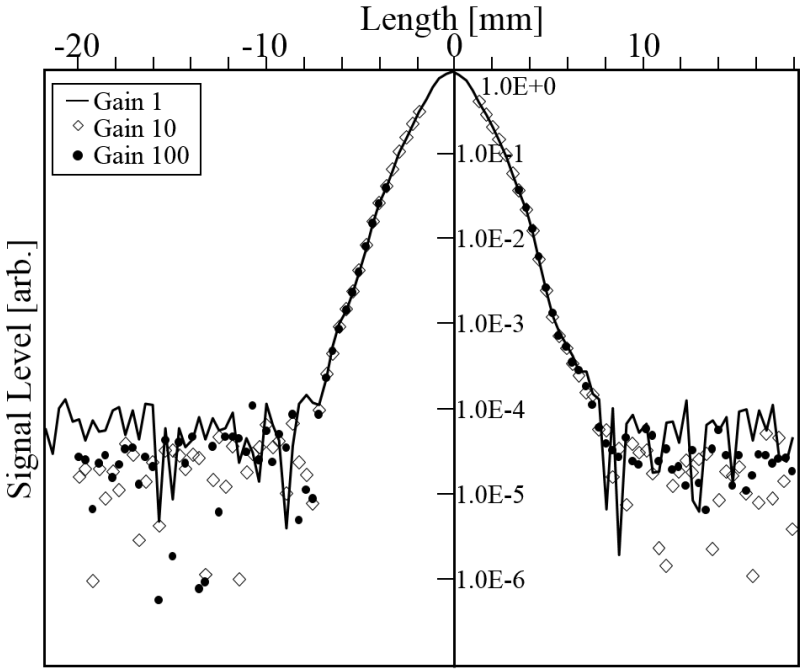

Figure 5-11: Vertical beam profile at ACS02.

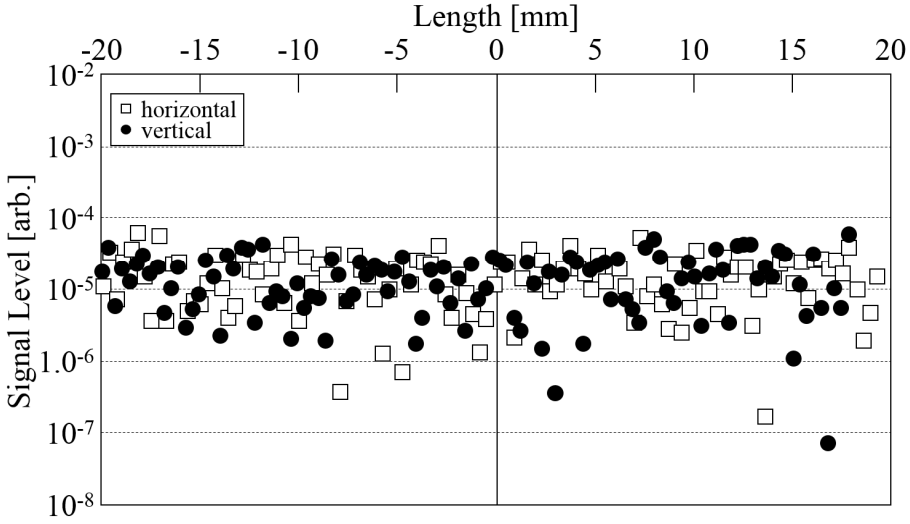

Figure 5-12: Background noise at ACS02 taken without beam operating.

The WSM waveforms located in the ACS section with beam center currents of 5 mA and 40 mA are shown in Figs. 5-13(a) and (b), respectively. As shown, the waveform appeared with negative polarity and the pulse heights of 410 mV and 2.9 V were estimated to correspond to current signals of 30 μA and 0.2 mA, respectively, for the 5 mA and 40 mA beam operation. The ratio of the signal was in close agreement to the ratio of the peak beam current.

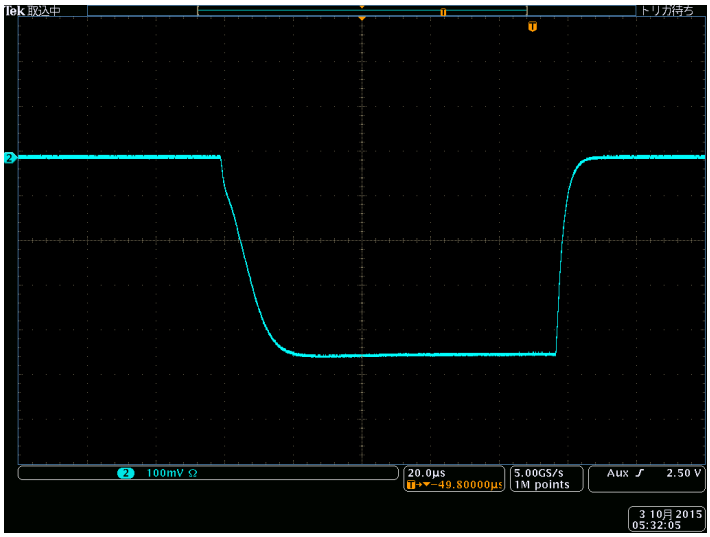

(a) For peak current of 5 mA.

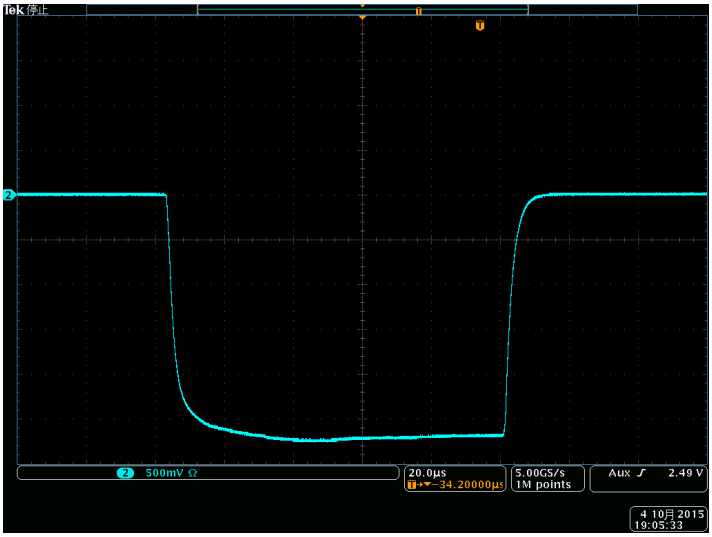

(b) For peak current of 40 mA.

Figure 5-13: Waveforms of the beam pulse by the tungsten wire with 100 mV/div in (a) and 500 mV/div in (b).

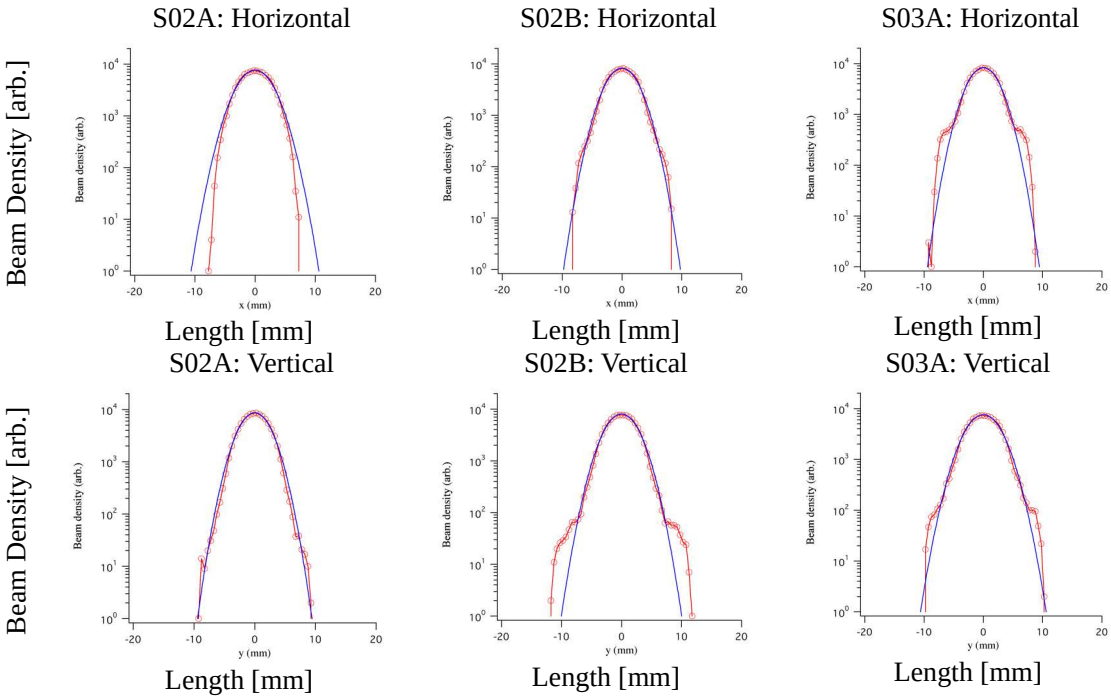

Figure 5-14: Beam profiles of a typical mismatching case measured by WSMs located at SDTL02 and 03.

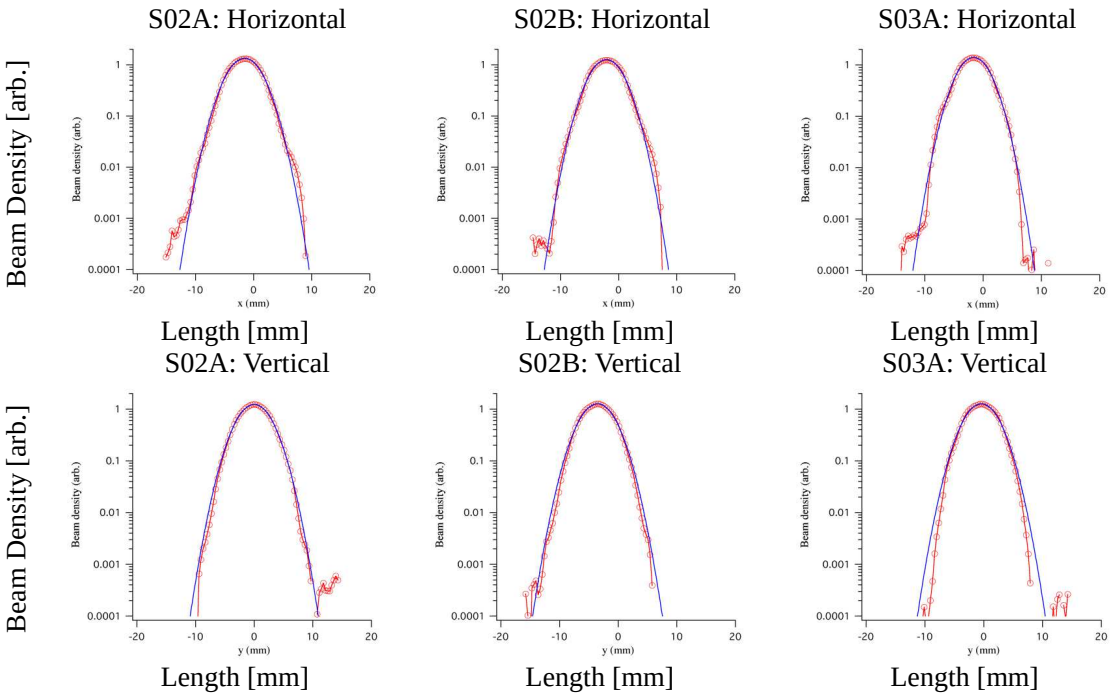

Figure 5-15: Beam profiles after the RMS beam alignment.

Figure 5-14 shows the beam profiles taken at 30 mA under mismatched conditions at SDTL 02 and 03. As shown, a halo grew rapidly. When we aligned the quadrupole magnet to the design beam envelope with a consideration of transverse beam profile in sigma fitting, a significant fraction of the beam halo disappeared, as shown in Fig 5-15. This demonstration is the first to show that WSMs can be used for matching operation and/or observing emittance growth at 30-mA current level.

5.4 New Tuning Method: Phase Tuning of Chopper Cavity

Precise beam chopping in the linac is an important issue for injecting the beam into the RCS. The RCS accelerates two bunches whose width reaches about 560 ns in normal operation, and the corresponding chopping factor is about 56 %, i.e., the beam is on for 560 ns and then off for 440 ns (see in Fig. 1-4). The RF chopper must be tuned to make a proper phase setting to kick all of the beam bunches out from the beam line to the scraper.

Although SCTs have been used for the beam current measurement, our WSM shown to exhibit a wide dynamic range, is capable of a beam measurement at several μA. When the phase is not properly set, small beams remain in the beam line. Therefore, we propose a new phase tuning method using the WSM to measure the small beam current, which is difficult to detect by SCTs.

Figure 5-16 shows a schematic of the tuning method of an RF chopper phase. An RF chopper has a pair of electrode which supplies an RF field to kick the beam out of the beam line to produce the intermediate structure of the beam pulse. If the RF chopper phase is detuned, the beam remains in the beam line. The remaining beam can be accelerated up to the exit of the linac, however, the beam cannot be accelerated in the downstream synchrotron (RCS) and it would be the fatal beam loss. When we tune the RF chopper phase, all of the beam bunches out from the beam line. If the phase is not at an optimum set-point, remaining beam is transferred to the downstream.

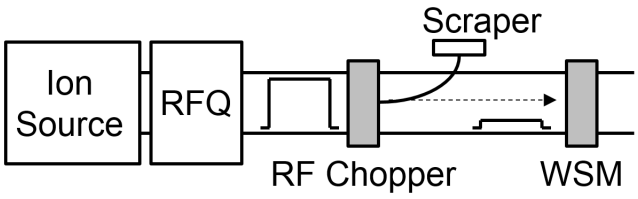

Figure 5-16: Schematic of the RF chopper tuning using WSM.

Figure 5-17 shows the signals of remaining beam current taken by the WSM. We inserted the wire at the position of highest intensity. The main component of the beam was kicked by the chopper cavity and the remaining components of the beam were analyzed as in Fig. 17 (a). When we shifted the phase setting to an optimal direction, the WSM signal due to the remaining beam gradually disappeared as shown in Figs. 5-17 (b) and (c). The remaining beam values were processed using a quadratic fitting as shown in Fig. 5-18. The axis of the parabolic function for the proper phase of chopper cavity was obtained by following the analysis. After changing the setting to the tuned phase, the remaining beam was checked again by the wire using over a hundred shots.
The tuning accuracy should become more important when the peak beam current is ramped up, because the beam loss increases almost proportionally with an increase in beam current. The proposed method allowed us to set the phase of the chopper cavity more accurately.

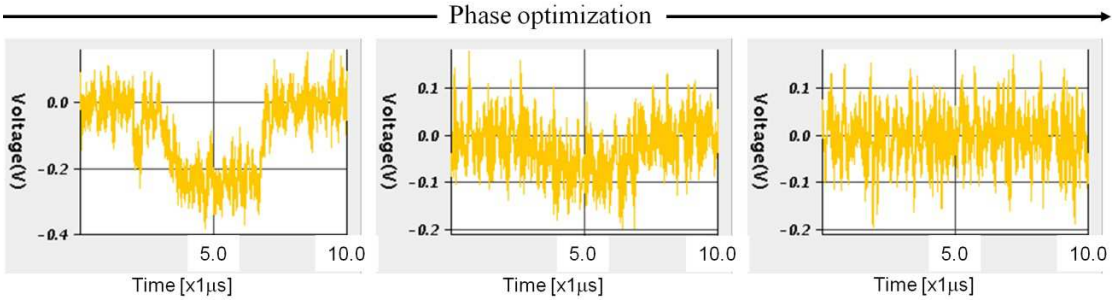

(a) Remained beam (b) Remained beam (c) No beam

Figure 5-17: Remained beam in kicked chopper measured using wire monitor.

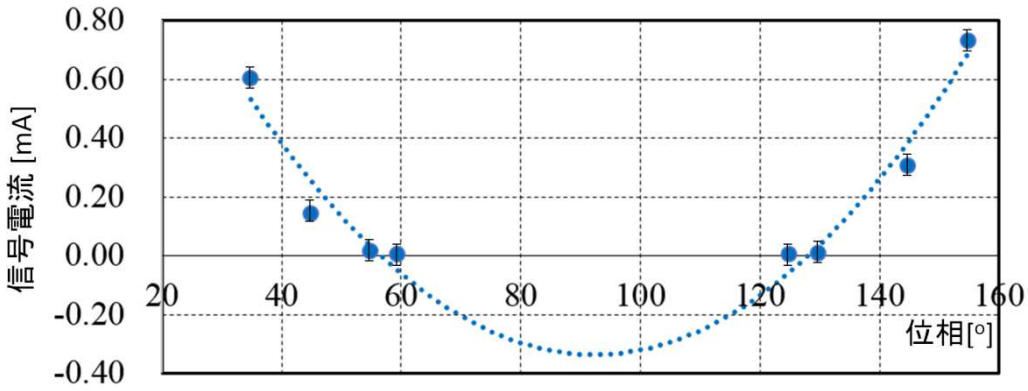

Figure 5-18: Signal height of the remaining beam current with fitting function.

5.5 Neutral Hydrogen Measurement

The WSM located in L3BT has two 2-mm thick carbon plates to collimate the beam tail shown in Fig. 5-4(b). These plates were considered to be effective for measuring low level of beam particles. Therefore, we proposed to use them for the neutral hydrogen particle (H^0) measurement. The electron in H^- is easily removed because of its small ionization potential (0.75 eV). In contrast, the neutralized hydrogen atoms cannot be controlled by the magnets and they might lead to a fatal beam loss. The beam loss is likely to become more significant when the peak current is increased.

When we intend to direct the beam to the 30° beam dump (shown in Fig. 5-1) or to the RCS, the bending magnet installed at the straight beam line must work properly. The main beam components (H^-) bended by 30º in the direction of the beam dump, but the H^0 particles did not bend in the same direction and traveled directly to the beam dump. We used the WSM for monitoring the neutralized hydrogen particles in the straight beam dump.

Figure 5-19 shows the result of the H^0 particle measurement at 15-mA operation. This is the top half of the H^0 beam profile. The signal was not detectable at 5-mA operation, but the beam profiles made by the H^0 particles could be recorded by this method. The signal level was thought to depend on the beam current, but the particle population was difficult to estimate because the WSMs were not calibrated. However, we demonstrated that we can determine the location and mechanism of neutral particle generation by the WSMs.

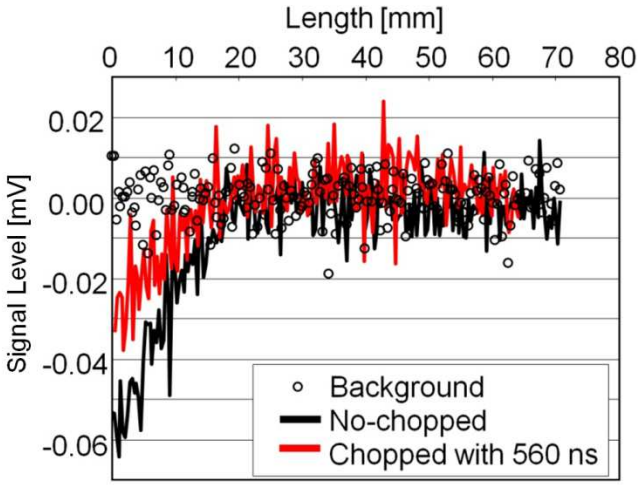

Figure 5-19: Half profile of neutral particles taken by carbon plates in WSM located in straight beam dump.

In the straight L3BT section, we determined the transverse matching using WSMs, but the longitudinal focusing force that suppresses excess beam loss could not be tuned. The relative peak intensities of the WSM signal indicate that the particle population cannot be controlled. We showed that mitigating these uncontrollable particles was possible by tuning the amplitude of the debuncher cavity (DB1) and/or by changing the longitudinal focusing force.

5.6 Summary

The main role of the WSM is to measure the RMS beam size for transverse matching. The transverse beam scan accuracy of 0.1 mm and a dynamic range of 10^{+2} are sufficient for the WSM because the transverse RMS size is typically 2 to 3 mm. However, we thought that tracking the beam halo and its growth are essential to mitigate the beam dynamics problem in the high current accelerator. Consequently, our goal was set to achieve a dynamic range of 10^{+4} because we intended to observe a beam halo at the same time.

A 30 μm diameter tungsten wire was selected for the WSM component based on the range and temperature calculations and a signal response was confirmed using the 30 μm wire. We demonstrated that the tungsten wire could lead to significant signal gain. In particular, the WSMs developed in J-PARC linac were able to achieve a dynamic range over 10^{+4} of the world top class, which allowed us to measure the evolution of beam halo.

In case of proton beam, the source of WSM signal is derived from only secondary electrons in a high energy region. From ref. [3], S. Igarashi et. al. used a flying wire system using a tungsten wire for the profile measurement. They reported in a figure that the dynamic range is within 10^{+2}. Based on the results of positive bias to suppress secondary electron emission, the signal response is almost 1.5 times greater than the non-bias signal response [9]. This indicates that the number of secondary electrons is almost half the number of the deposited electrons.

We proposed a new chopper phase tuning method by utilizing the wide dynamic range of the WSM. This unprecedented method led to accurate tuning schemes, not only for the present operation, but for the higher peak beam current operation that will be used.

Although a crude transverse beam profile and its intensity distribution could be measured using an imaging plate [13], it was difficult to estimate the exact profile. Our carbon plate collimator in the WSM could be used for measuring the neutral particle population, and we demonstrated that its high sensitivity enabled the measurement and

provided us a new scheme of debuncher tuning in the higher J-PARC peak beam current.

All of these technologies and measurement schemes should play important roles in the energy upgrade and to increase the peak beam current.

References

[1] K. Wittenburg, “Specific Instrumentation and Diagnostics for High-intensity Hadron Beams”, *A text of CAS - CERN Accelerator School, Course on High Power Hadron Machines*, May, (2011).

[2] S. G. Arutunian, et. al., “Large Aperture Vibrating Wire Monitor with Two Mechanically Coupled Wires for Beam Halo Measurements”, *Physical Review Special Topics – Accelerators and Beams*, ***17***, 032802 (2014).

[3] S. Igarashi, et. al., “Space Charge Effects during the Injection Period of the KEK PS Main Ring Proceedings of the 2003”, *Particle Accelerator Conference*, Portland, Oregon, USA, **WPPG009**, (2003).

[4] C. H. Back, et. al., “A Novel wire scanner for high intensity pulsed beams”, *SLAC report*, **SLAC-PUB-8061**, (1999).

[5] M. Plum, et. al., “SNS Linac Wire Scanner System: Signal Levels and Accuracy”, *Proceedings of the 22rd Linear Accelerator Conference (LINAC2002)*, **172**, Gyeongju, Korea, (2002).

[6] M. Ikegami, et. al., “Measurement and Simulation in J-PARC Linac”, *Proceedings of the 46th ICFA Advanced Beam Dynamics Workshop on High-Intensity and High-Brightness Hadron Beams (HB2010)*, **THO1A02**, Morschach, Switzerland, (2010).

[7] H. Akikawa, et. al., “Profile Measurement and Transverse Matching in J-PARC Linac”, *Particle Accelerator Conference*, 2007. PAC. IEEE, **1472–1474**, (2007).

[8] H. Akikawa, et. al., “Wire Profile Monitors in J-PARC Linac”, *Proceedings of the 23rd Linear Accelerator Conference (LINAC2006)*, **TUP021**, Knoxville, Tennessee USA, (2006).

[9] William R. Leo, “*Techniques for Nuclear and Particle Physics Experiments*”, Springer, (1994).

[10] Stopping-Power and Range Tables for Electrons, Protons, and Helium Ions, http://physics.nist.gov/PhysRefData/Star/Text/contents.html

[11] E. J. Sternglass, “Theory of Secondary Electron Emission by High-Speed Ions”,

Physical Review, **108**, 1(1957).

[12] A. Miura, et. al., “Operational Performance of Wire Scanner Monitor in J-PARC Linac”, *Proceedings of International Particle Accelerator Conference (IPAC2010)*, **MOPE021**, Kyoto, Japan, (2010).

[13] R. C. McCrady, et. al., “Stripping of H-minus Beams by Residual Gas in the Linac at the Los Alamos Neutron Science Center”, *Proceedings of Linear Accelerator Conference (LINAC2010)*, **THP069**, Tsukuba, Japan, (2010).

Chapter 6

Longitudinal Pulse Width Monitor (Bunch Shape Monitor)

In order to upgrade the beam energy, the acceleration frequency must be increased to 972 MHz which is thrice of the SDTL frequency. As the frequency jump may lead to beam loss due to longitudinal mismatch, we need to perform beam-length matching between SDTL and ACS section. Bunch shape monitors (BSMs) were developed to follow the beam behavior in the two ACS-type buncher cavities for the longitudinal beam matching. The typical bunch phase length is considered to be 2-3^{o} in the new ACS cavities, therefore the phase resolution should be less than 1.0^{o}. The design developed in the Institute for Nuclear Research, Russian Academy of Science (INR/RAS) [1, 2] was utilized for the BSM because of finer phase resolution.

There are several schemes for the bunch shape measurement, among them a waveform comparison using BPM electrode is a possible candidate [3]. We chose the BSM using secondary electrons from a thin target which probes the ion beam profile, because secondary electrons are emitted and accelerated quickly keeping the time structure [4, 5]. An RF deflector system modulates the electron energy at the same frequency with the ion beam, while an additional magnetic field can separate the secondary electrons from detached electrons.

A tuning method was proposed using BSMs in which we took the longitudinal matching using three BSMs together with the transverse profile matching. The new longitudinal tuning method was developed because of no redundancy of the BSM location. In the final part of this chapter, we discuss usefulness of BSMs for the tuning of linac at higher energy and intensity.

6.1 Development of Bunch Shape Monitor

6.1.1 Principle of Bunch Shape Measurement

A device for the longitudinal beam width measurement was designed on the basis of observation of secondary electrons from a single wire intersecting the beam, as shown in Fig. 6-1 [6, 7]. Figure 6-1 shows a schematic of the operation. A series of bunches of the beam under measurement intersects the target wire of 0.1 mm diameter and low-energy secondary electrons are emitted by the beam-wire

interaction. The wire is held at a negative potential of typically -10 kV. The secondary electrons move almost radially and enter the RF deflector through collimators.

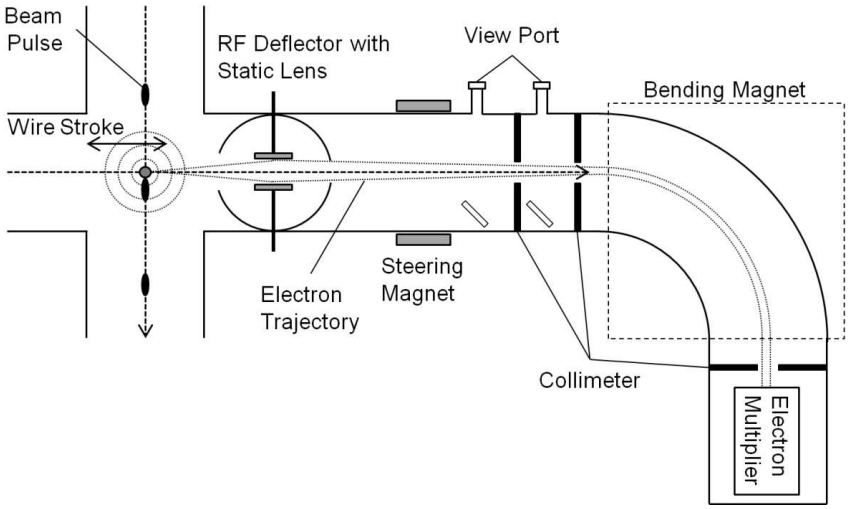

Figure 6-1: Schematic diagram of BSM.

We applied an RF-field with the same frequency as the accelerating RF (324 MHz). The deflection of the electrons at the exit of the RF deflector depends on their phase with respect to the deflecting field. By adjusting the phase of deflecting field with respect to the accelerator RF reference, we could obtain the longitudinal width of bunches.

6.1.2 System Configuration of Bunch Shape Monitor

The BSM comprises a body, an RF deflector, a steering magnet, an actuator, and an electron detector (shown in Figs. 6-2 and 6-3). The BSM body was designed for installation between the quadrupole doublets. The RF deflector and the actuator that holds the target wire were vertically installed against the beam axis. Secondary electrons pass through the collimators of the RF deflector and the duct connected to the electron detector. The target wire made of tungsten has a diameter of 0.10 mm. It can be moved by the actuator driven by a stepping motor in the vacuum chamber with a minimum precision of 0.50 μm.

The collimators and the structural parts degraded the pumping conductance. During the BSM measurement, we applied a high bias voltage to the static lens and the target wire, and controlled the RF power input as a main parameter. They were also the main factors influencing the vacuum condition.

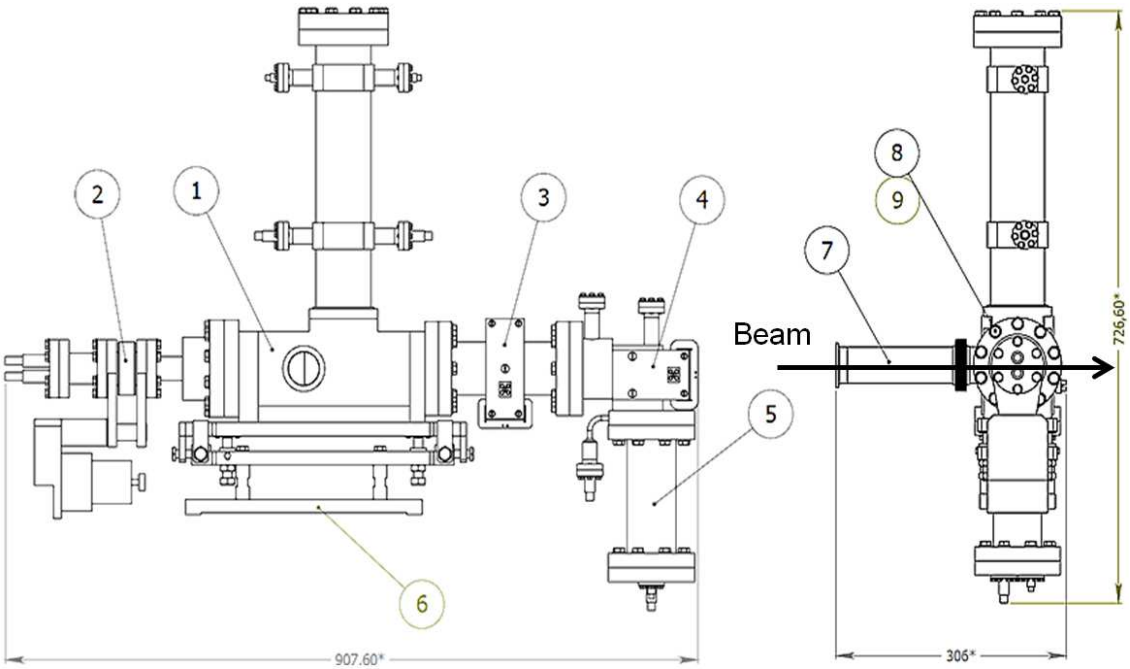

Figure 6-2: BSM outline (1-Body, RF Deflector, 2-Actuator, 3-Steering Magnet, 4-Bending Magnet, 5-Detector, 6-Support, 7-Beam Duct).

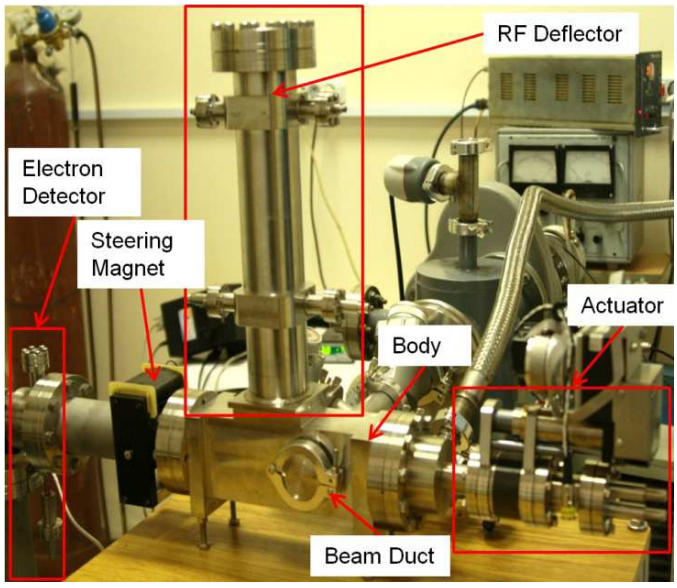

Figure 6-3: Whole view of BSM.

The RF deflector shown in Fig. 6-4 is composed of a pair of electrodes whose length is adjusted to be $\lambda/2$ (λ: wave length of the acceleration frequency of 324 MHz). We applied a constant DC voltage to focus the secondary electron trajectories.

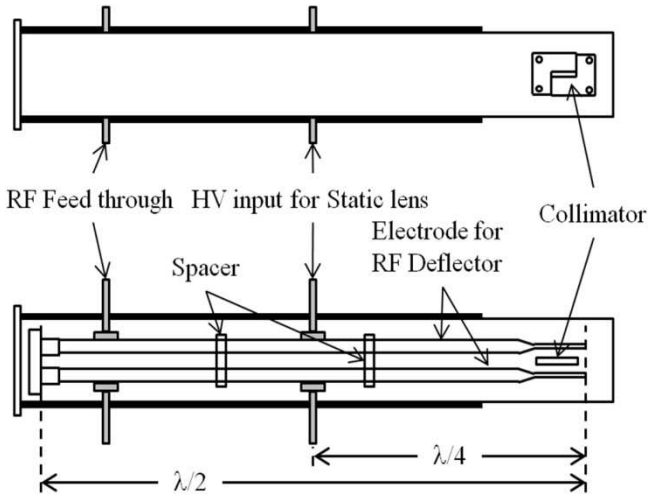

Figure 6-4: Schematic view of RF deflector. Upper is the surface of deflector and the lower is the top-view of deflector.

The electric field around the RF deflector was calculated and shown in Fig. 6-5 [8]. We set the electrodes into the RF deflector, and placed collimator #1 and #2 on a side surface of the RF deflector. The collimators #1 and #2 were connected to the ground, and the potential of the electrodes was typically biased to -8.0 kV.

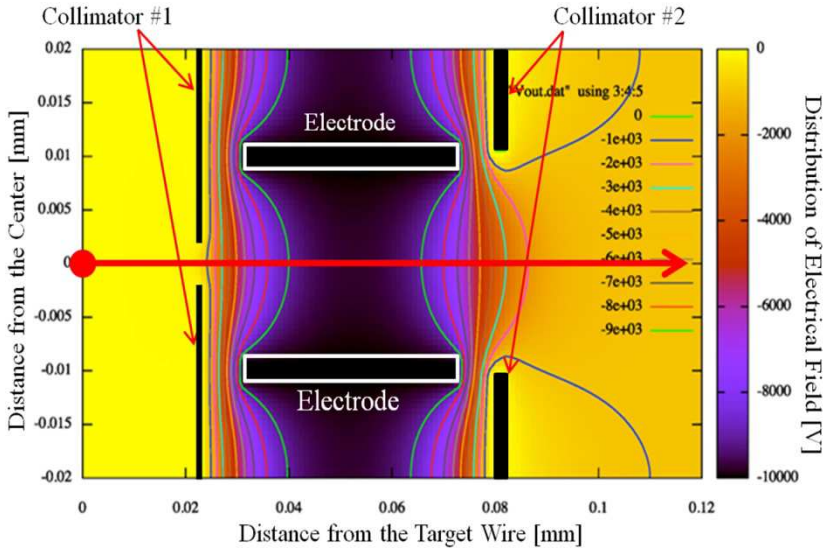

Figure 6-5: Electric filed inside the BSM where the electrodes are negatively biased.

Secondary electrons accelerated from the target wire by -10.0 kV passed through the collimator #1. They are deaccelerated by the gradient of the field to the center of the electrodes, and finally accelerated again by the symmetrical gradient.

The target wire was movable in the vacuum chamber with precision of 0.5 μm, so the

spatial resolution was enough high for the measurement of the bunch shape. The BSM operational parameters are field strengths of the bending magnet, the steering magnet and the static lens, and also bias voltages of the wire for electron multiplication.
We measured the relation between the control voltage and the phase to make a fitting function for accurate phase control. The fitting function was used for all of the phase shifters which could be operated with 1^{o} intervals.

6.1.3 Installation Layout

We assembled all three BSMs before moving to accelerator tunnel and made laboratory tests of mechanics, electronics, and control systems. They were installed in ACS cavities, ACS type-bunchers between the original SDTL and the additional ACS section. The acceleration frequency jumps from 324 MHz to 972 MHz in this section as was shown in Fig. 2-7 (in Chapter 2). During the BSM measurement, the RF powers of ACS cavities were switched off, and used two 972 MHz ACS-type buncher cavities as the knobs for the longitudinal-width matching.

6.1.4 Positioning of Target Wire

When the target wire is intercepting the series of beam bunches, we can use an integrated beam loss signal to take a proper position of the target. The signals from the nearest downward beam loss monitor are shown in Fig. 6-6. This profile was almost correspondent with the transverse profile taken by WSM.

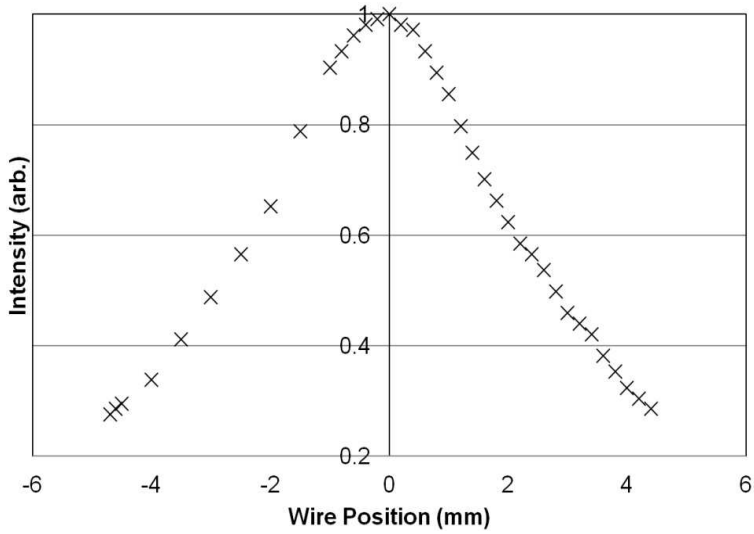

Figure 6-6: Plots of beam loss signal obtained by BSM.

6.2 First Beam Test

6.2.1 Evaluation of Phase Resolution

The most important characteristic of the BSM is phase resolution. The resolution includes several constituents. The phase resolution of BSM can be found experimentally by considering the focusing and deflecting properties of the electron optical channel.

This component can be found as

$$\Delta\varphi = \frac{\Delta Z}{Z_{max}} \ , \qquad (6\text{-}1)$$

where ΔZ is full width at half maximum of the focused secondary electron beam and Z_{max} is the maximum electron displacement at output collimator due to RF deflection. First of all, we tested focusing property of the optical channel and calculated the RMS width of the measured curve. This width was expressed in millimeters based on calibration (10 V of steering voltage corresponds to 1 mm of electron beam displacement). The minimum RMS size was 0.23 mm corresponding to the output collimator size of 0.5 mm. To find the maximum displacement Z_{max}, we measured relative phase positions of the observed bunches in a broad range.

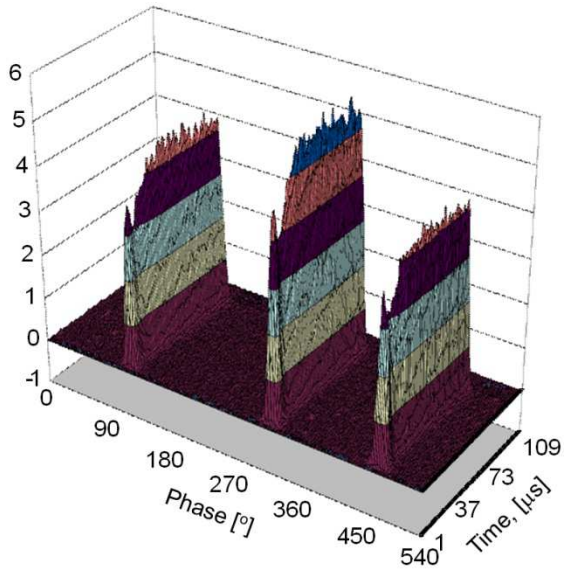

Figure 6-7: Example of bunch phase positions for wide range phase adjustment.

Figure 6-7 demonstrates an example of the phase position for 540° range of phase. If the steering voltage is adjusted to direct the electrons exactly into the slit of the output collimator, the observed bunches should be periodical with the period of 180°.

If the electron beam at the output collimator is displaced by Z_c the observed bunches becomes bi-periodical: the phases of the observed bunches becomes 180°-2Δ and 180°+2Δ.

The parameters Δ, Z_c and Z_{max} are related as

$$\Delta = \frac{Z_c}{Z_{max}} \ . \qquad (6\text{-}2)$$

Figure 6-8 shows the phase position of the observed bunches for Z_c=15 mm and Z_c=-15 mm. The phase distances between the adjacent bunches versus Z_c is shown in Fig. 6-9. Using Eq. (6-2), the value of maximum displacement Z_{max} can be found to be equal to 54.5 mm. Substituting ΔZ=0.5 mm and Z_{max}=54.5 mm in Eq. (6-1) the phase resolution can be estimated to be : $\Delta\phi$=0.53°.

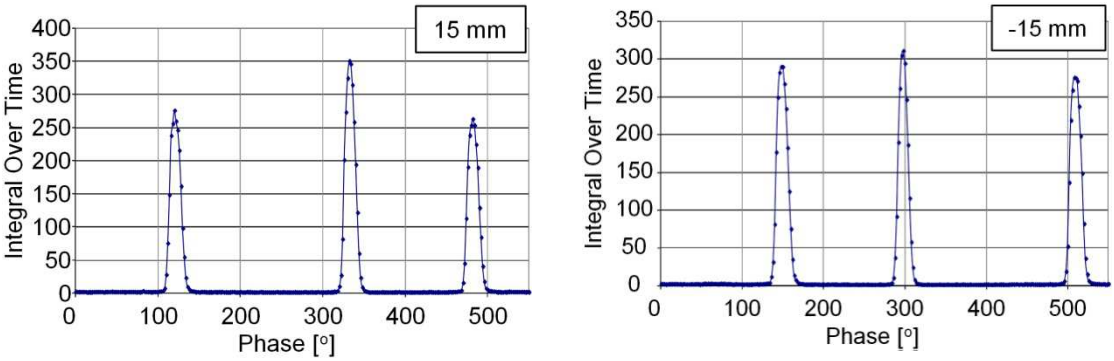

(a) Z_c = 15 mm (b) Z_c = -15 mm

Figure 6-8: Phase position of bunches.

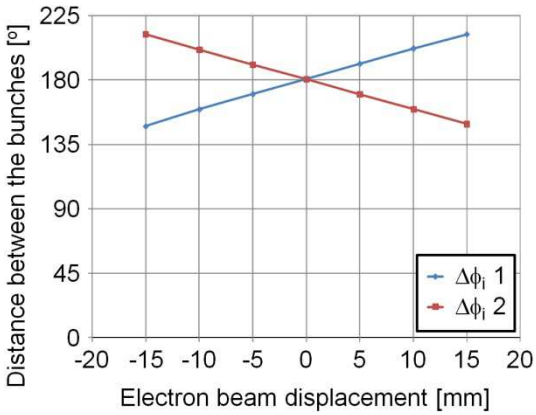

Figure 6-9: Dependence of phase distance between the adjacent bunches on electron beam displacement.

6.2.2 Functioning Tests

In the BSM functioning tests, we had only 324 MHz-driven cavities and used the 15th SDTL cavity as a knob of the longitudinal focusing device, because there were

no ACS cavities. The test beam parameters were as follows: 324-MHz operational frequency, 170-MeV source energy, 15-mA peak beam current, and 3-mm transverse beam size in rms. The phase shifter of the RF deflector could work at 1.0°-intervals, and the signals were sampled with intervals of 1 μs.

There was no RF cavity between the exit of SDTL and the BSMs. Then, the phase width of the beam started to grow rapidly after the SDTL exit due to space-charge effect. The beam phase width further grows between BSMs. The beam phase width measured with a downstream BSM is larger than that with an upper stream one. Using this relation, we made a check on the consistency among BSMs. Then, we turned on and off the last SDTL module, or SDTL15, to move the phase width growth point upstream.

The beam phase width measured with each BSM is shown in Fig. 6-10. The knob of the measurement was RF on-off of the SDTL15. The reference line was obtained when the SDTL15 on but blue one shows the phase when the SDTL15 off. This relation and the tendencies of phase width were as expected.

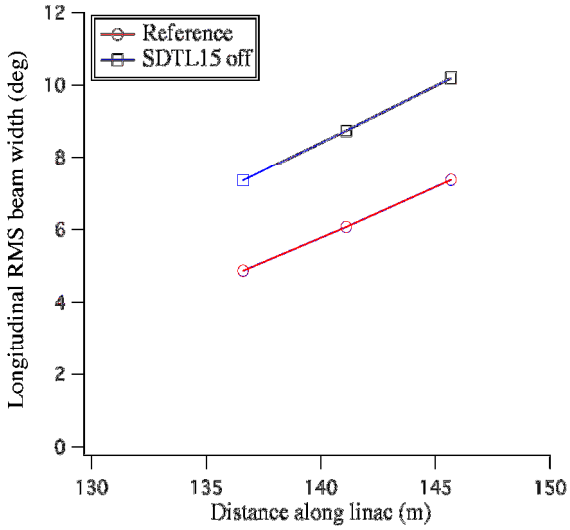

Figure 6-10: Initial check of BSM measurement.
Reference means RF on of SDTL15 as a nominal operation.

We have made more detailed monitor verification as follows. We estimated that the consistency of the RMS phase width among BSMs by switching off the cavity in front of the BSMs. We changed the SDTL15 amplitude while setting its synchronous phase to -90°. We measured the response of each monitor with respect to the SDTL15 amplitude. In this situation, the width was predicted to be larger at the downstream monitor positions using 3D-PIC simulation.

Figure 6-11 shows the measured dependence and simulation results. In the figure, horizontal axis means a scaled focusing strength with an amplitude of ADTL15, and the nominal SDTL15 amplitude was assumed to be 1.0. When the RF amplitude was increased, focusing strength was expected to increase proportionally. As can be seen in this figure, the experimentally obtained phase width dependence agrees with the simulated value for BSM#1 and #2, however, the result for the BSM#3 showed some discrepancy. After we investigated the results of BSM#3 carefully, it was concluded that a mechanical assembly error caused this discrepancy.

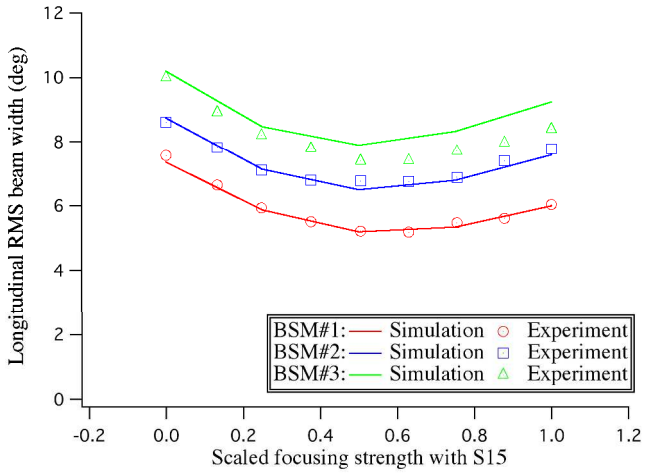

Figure 6-11: Measured longitudinal RMS beam width versus focusing strength of last SDTL cavity (SDTL15) and corresponding simulation results.

6.2.3 First Measurement of Longitudinal Bunch Width

The first data acquisition of longitudinal width was conducted after transverse matching. The first data recorded by BSM#1 is shown in Fig. 6-12 [9]; plots of the intense signals recorded by the electron detector versus phase led to the Gaussian shapes of 1-μs intervals. Starting from 0 μs, the beam bunch comes from the backside, and the phase shifted because of a feed forward delay and it can be seen around the pulse head. Moreover, noisy electrons enter into the electron detector, and the base level around the bunch tail increases.

The dynamic range of the monitor reached ~10^3 as shown in the figure. This range is sufficient for calculating the RMS bunch width, but the high sensitivity would be advantageous to study the beam dynamics. When we shifted the phase from 0° to 540° against the acceleration frequency, we should be able to observe three intensity peaks up-to 540°, because the amplitude of the deflection RF reaches zero every

180° phase.

We chose the peak with the lowest noise for the RMS calculation. We fit the data in Fig. 6-24 with the Gaussian profile, and calculated the RMS longitudinal width to be 5.02°. As the data was fit very smoothly to the Gaussian shape, we considered that the phase resolution is sufficient for measuring the longitudinal bunch width [10].

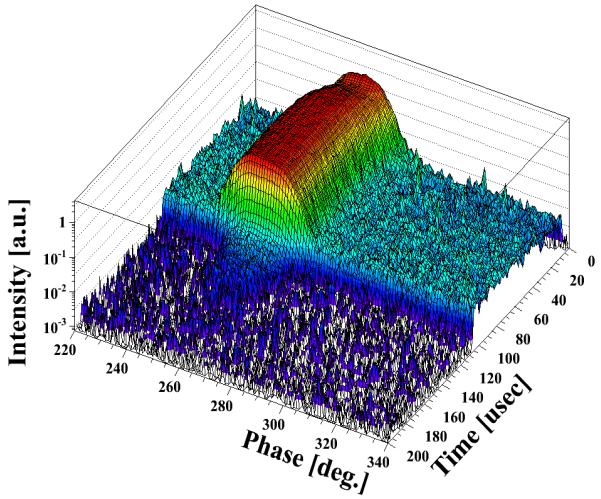

Figure 6-12: First data of longitudinal width measurement by BSM#1. The beam bunch originates from the backside.

6.3 Errors of Bunch Length Measurement

6.3.1 Effect of the RF Feed Forward System

When the beam operation started, we usually tuned an RF feed forward (FF) system for the compensation of the RF power loss due to the pass of charged particles through the RF cavity. To investigate the behavior of the pulse head, we took waveforms at various peak beam currents. In 30 mA operation, the peak beam current can be squeezed by the scraper in the upstream of linac to make 5 to 30 mA with 5 mA intervals.

A wake field in an RF cavity is caused by traveling electric field induced by the charged beam pulse. The strength of the wake field directory depends on the traveling electrical field, i.e., the peak beam current. The wake field counteracted the beam pulse, namely that induced a slowdown of the beam particles [11].

Figure 6-13 shows an example of the wake field effect on the beam pulse. In the figure, pulse heads are the left and the tails are the right. The color contour means intensity of the signal. At a 5 mA level, the phases were not affected by the wake field and the profiles were almost straight. When the peak-beam current was getting

higher, the pulse heads were effectively bended. This was usually compensated by the RF feed forward system. Without compensation, it was usually difficult to calculate the pulse width accurately. These results suggested the importance of RF feed forward adjustment to compensate the wake field for the measurement at high peak beam current operations.

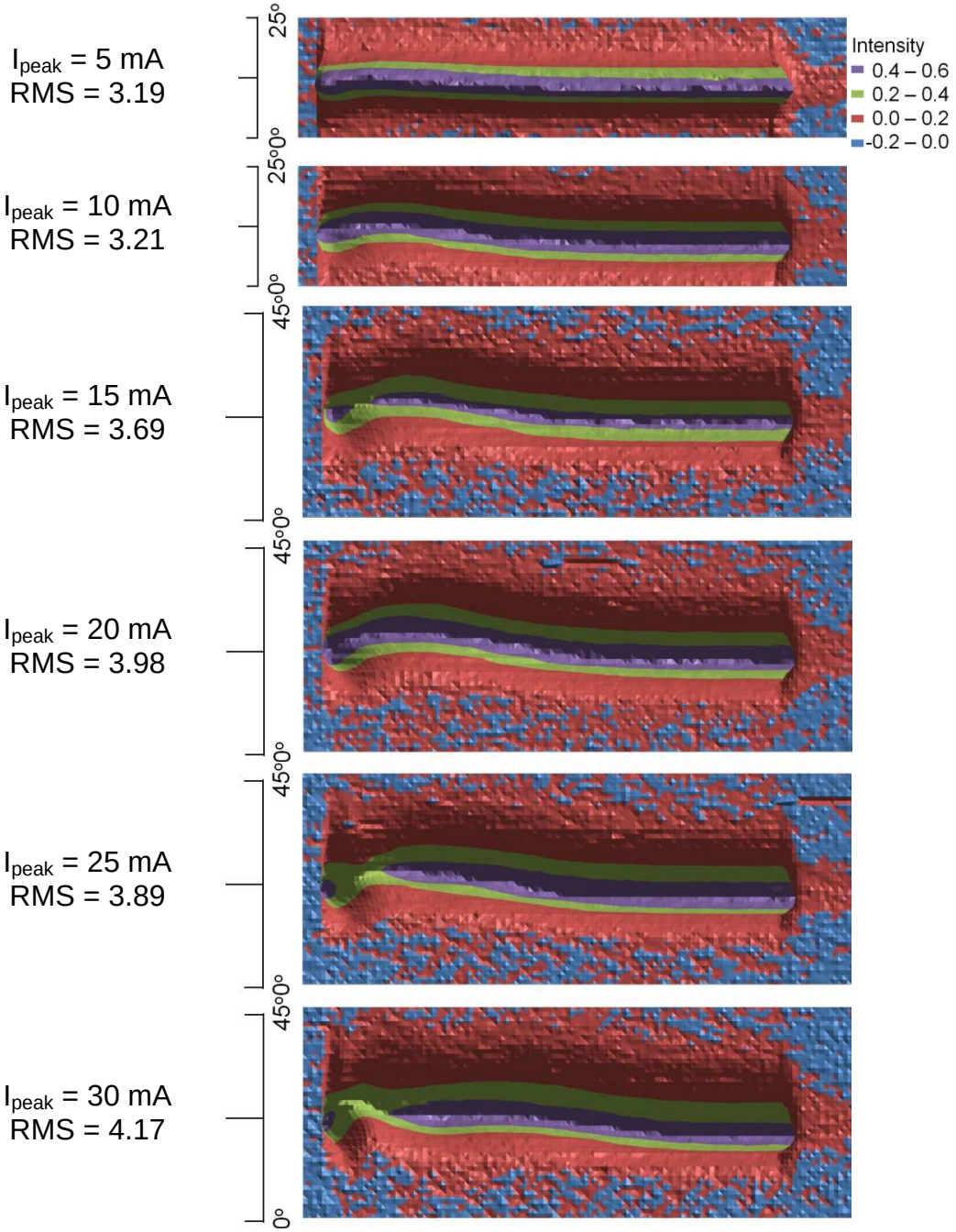

Figure 6-13: Wake field effect on waveform. Feed forward system is off and peak beam current is changed.

Conventional BSMs used in the other facilities have not measured such high beam currents. This is the world first measurement of the wake field which gives us important lessons for the measurement errors and understanding the slowdown mechanism of the beam acceleration.

The measured longitudinal bunch width was not uniform, and this would affect the RMS bunch width calculation. Therefore, we picked up the last half of the pulse to neglect the feed forward delay. Then the RMS width here is the average through the last half of the pulse.

6.3.2 Effect of Off-Centering Beam

When the peak beam current is increasing, the target wire will be exposed to a higher peak beam current and the thermal stress will become serious. Then the misalignment with the beam axis should be evaluated correctly.

Several measurements were conducted for different horizontal wire positions scanning from −2 mm to +2 mm in steps of 0.5 mm as shown in Fig. 6-14. Here the positive position means the wire is inserted to the right position of the detector in Fig. 6-1, so that the position is nearer to the collimators and the electron multiplier than the optimum position. To control the thermal stress, we evaluated the data taken at an off-center beam with those taken at an on-center beam. The minimum phase spread can be seen at −1.0 mm where the maximum signal was detected by the electron multiplier and the Gaussian fitting is shown to underestimate the actual RMS bunch length [11].

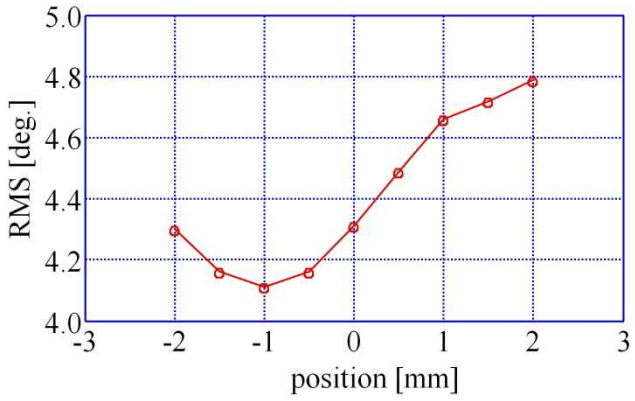

Figure 6-14: RMS phase spread at different horizontal wire positions.

This tendency agrees with the front-end bunch length of the 3-MeV beam measured at Linac4 at CERN [12]. The absolute bunch length of the 3-MeV beam is quite

larger than that above 191 MeV beam in J-PARC. The signal-level shift with wire position is considered to be caused by the shift of focus position.

Because the BSM is a type of wire scanning device, the possibility of using it as a horizontal profile monitor is incidentally discussed [12], because the signal level is a function of the wire position. However, the measurement results include functional errors. We usually defined the wire position of the beam center by the beam loss signal taken at the downstream beam loss monitor (Fig. 6-6 in 6.1.4). In focus of the optimum wire position (0 mm in Fig. 6-14), phase size was proportionally dependent on the position shift, the dependence was approximately 1% of RMS phase width per 0.1 mm, therefore the wire shift should be within ± 0.5 mm and corresponding phase error width was estimated to be within $\pm 0.5^{o}$ in phase. In the discussion of the electrical field in Fig. 6-5, static field is optimized to focus the electron trajectory on the collimeters. When the target wire is horizontally shifted, the focusing point is shifted. This shift is considered to be the cause of the phase shift.

6.3.3 Linac Beam Dynamics Study

For a study on space-charge driven transverse-longitudinal coupling resonance, we measured the longitudinal emittance with BSMs. The results are expected to contribute to the design of the beam operational parameters for the energy upgraded linac. The high intensity linac design follows the equipartitioning (EP) condition. That means a strict control of the transverse and longitudinal tune ratios throughout the linac is considered to be important. To ensure space-charge driven emittance exchange between the longitudinal and transverse planes should be minimized as the tune ratio diagram indicates (Hofmann's stability charts). By the development of BSMs, we can conduct an experimental study on the topic [13], namely we can monitor both the transverse and longitudinal emittance simultaneously for the first time.

When the J-PARC project started its design, there were enough evidences that an EP conditioned lattice offers a natural solution for emittance conservation at such high-intensity hadron accelerators, owing to the pioneering works by I. Hofmann, R. A. Jameson et al, [14] and the data based on experiences from SNS. Fortunately J-PARC linac could find its EP solution as the baseline design without sacrificing the hardware efficiency. It also has the applicability for a wide range of off-EP condition. Then it is offering opportunities not only for investigating the basic beam physics principles but also for further optimizations of the machine operation.

When the horizontal, the vertical and the longitudinal temperature stand for T_x, T_y and T_z, normally we can assume T_x=T_y. As shown in Fig. 6-15, it is possible, within the hardware capability, we can set the DTL, the SDTL and the ACS in a wide range of T_x/T_z. The temperature ratio of horizontal and longitudinal (T_x/T_z) is also the ratio of oscillation energies in transverse and longitudinal plane, which is defined as,

$$\frac{T_x}{T_z} \equiv \frac{r_x^2 k_x^2}{r_z^2 k_z^2} = \frac{\epsilon_x k_x}{\epsilon_z k_z} \ . \qquad (6\text{-}3)$$

Here r stands for the beam RMS envelope, ε the RMS emittance. Focusing is represented by the wave number k (with current) and k_0 (0-current). For instance, settings to the left in the Fig. 6-15 means less transverse focusing or more longitudinal focusing and vice versa. The EP condition generate biggest stable area for the beam propagation.

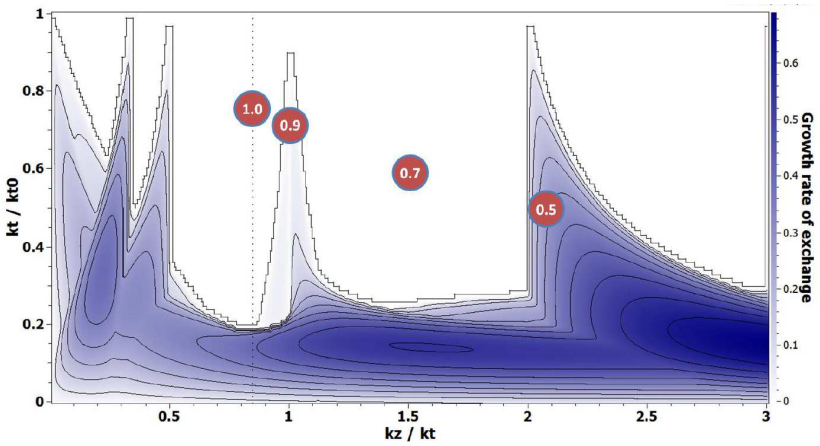

Figure 6-15: Hoffman's stability chart for J-PARC linac with an emittance ratio ε_z / ε_t =1.2 [17].

Four different working points have been tried with temperature ratios of 1.0, 0.9, 0.7 and 0.5 as in Fig. 6-15. To avoid any uncertainty from matching into the DTL, only the SDTL section has been modified for each test case, by adjusting the quadrupole gradients such that the beam stays on the resonance, thus enhancing the effect. The front-end and the DTL settings are kept constant for all measurements. The beam current was set at 15 mA which was the operating value. The design current is 30 mA for the first phase of the project and 50 mA after the energy upgrade.

The experimental procedure follows several steps. First the quadrupole settings in the SDTL section are changed such that the working point is brought to the desired value. Transverse matching is then achieved at the DTL-SDTL transition with an array of

wire scanner monitors (WSMs) and quadrupoles. Next, WSMs are used to measure the transverse emittance at the ACS entrance. Finally, bunch shape monitors (BSMs) are used at the ACS entrance to evaluate the longitudinal emittance. This procedure is repeated for each of the working points. Details of the SDTL-ACS section are given in Fig. 6-16 (same as Fig. 2-7 in chapter 2). Gradients of four quadrupoles in DTL-SDTL transition are varied and the beam size is measured with four periodically located wire WSMs. Matching involves the use of an envelope over several quadrupole tuning iterations until the RMS beam widths are equal.

By knowing the phase advance between the scanners, emittance and Twiss parameters can be obtained by a parameter fitting routine to the measured RMS beam widths. For this, a 3D envelope model of the machine used during operation and developed in Open XAL is being employed [15, 16].

The longitudinal emittance measurement is also performed at the SDTL-ACS transition, using one of the three BSMs. The synchronous phase of tank SDTL15 is set to bunching mode (-90^{o}) and the RMS phase width is measured at the BSMs as a function of the tank amplitude. The resulting beam profiles measured for the J-PARC linac with BSM can be seen in Fig. 6-11 and 6-12, showing the bunch length for the entire pulse duration. The emittance and Twiss parameters at SDTL15 were then calculated by doing a 3-parameter scan to fit the measured beam widths.

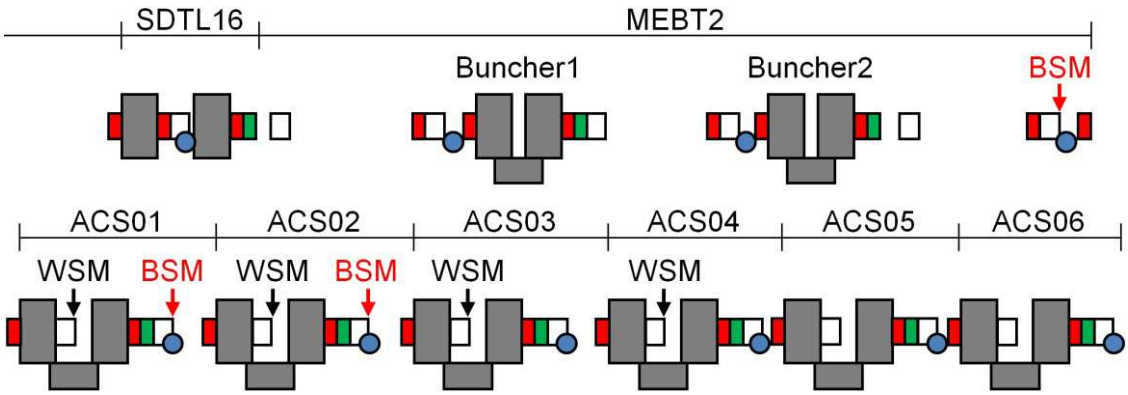

Figure 6-16: Beam monitor layout around SDTL16. The positions of the WSMs and the BSMs are indicated with arrows.

Instead, the fitting was done by particle tracking using IMPACT simulation and assuming a Gaussian distribution at SDTL15 [16]. During BSM calibration, a full scan was performed in which the RMS beam width was measured as a function of SDTL15 tank amplitude and then compared with simulations performed with

IMPACT and TraceWin. The results for BSM#1 which will be further used for the measurement of emittance can be seen in Fig. 6-11 where a good agreement between the simulation and the measurement can be observed.

The emittance evolution throughout the linac for the four cases can be summarized in Table 6-1. The graphical representation seen in Fig. 6-17 shows some emittance exchange for case T=0.9 (k_z / k_t = 1) and much stronger for T=0.5 (k_z / k_t = 2), while cases T=1.0 and T=0.7 show no exchange. It is also interesting to note that there is a strong longitudinal emittance growth between the end of the SDTL and the location of BSMs. This is caused by the absence of longitudinal focusing in this section and is the reason for needing multiparticle tracking to estimate the emittance.

Table 6-1: Simulated emittance evolution vs. position in the chart (Fig. 6-15) for the four working points tested [17].

T_t / T_z	DTL Output [π.mm.mrad]		DTL Output [π.mm.mrad]		Emittance Growth [%]	
	ε_t	ε_z	ε_t	ε_z	ε_t	ε_z
1.0	0.229	0.260	0.237	0.261	3.1	0.4
0.9	0.229	0.260	0.243	0.249	5.7	- 4.1
0.7	0.229	0.260	0.237	0.260	3.2	0.2
0.5	0.229	0.260	0.266	0.243	15.6	- 6.7

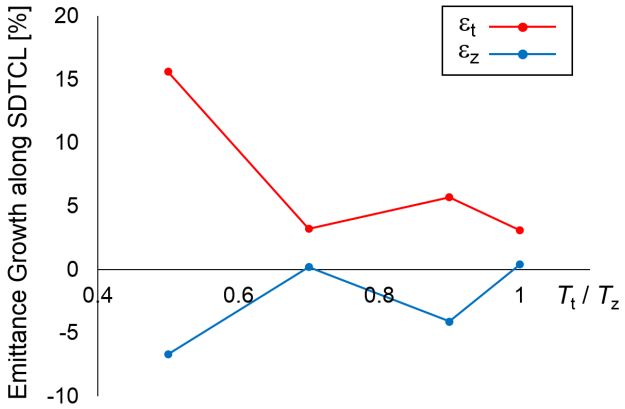

Figure 6-17: Simulated emittance growth in the linac for the four working points tested.

As explained above, the transverse emittance is measured at the SDTL output using a set of WSMs at the beginning of the ACS section. Typical horizontal and vertical beam profiles can be seen in Fig. 6-18. The longitudinal emittance is estimated using RMS beam phase lengths measured with BSM#1.

The results are summarized in Table 6-2 where the measured emittance values at the end of the SDTL are presented.

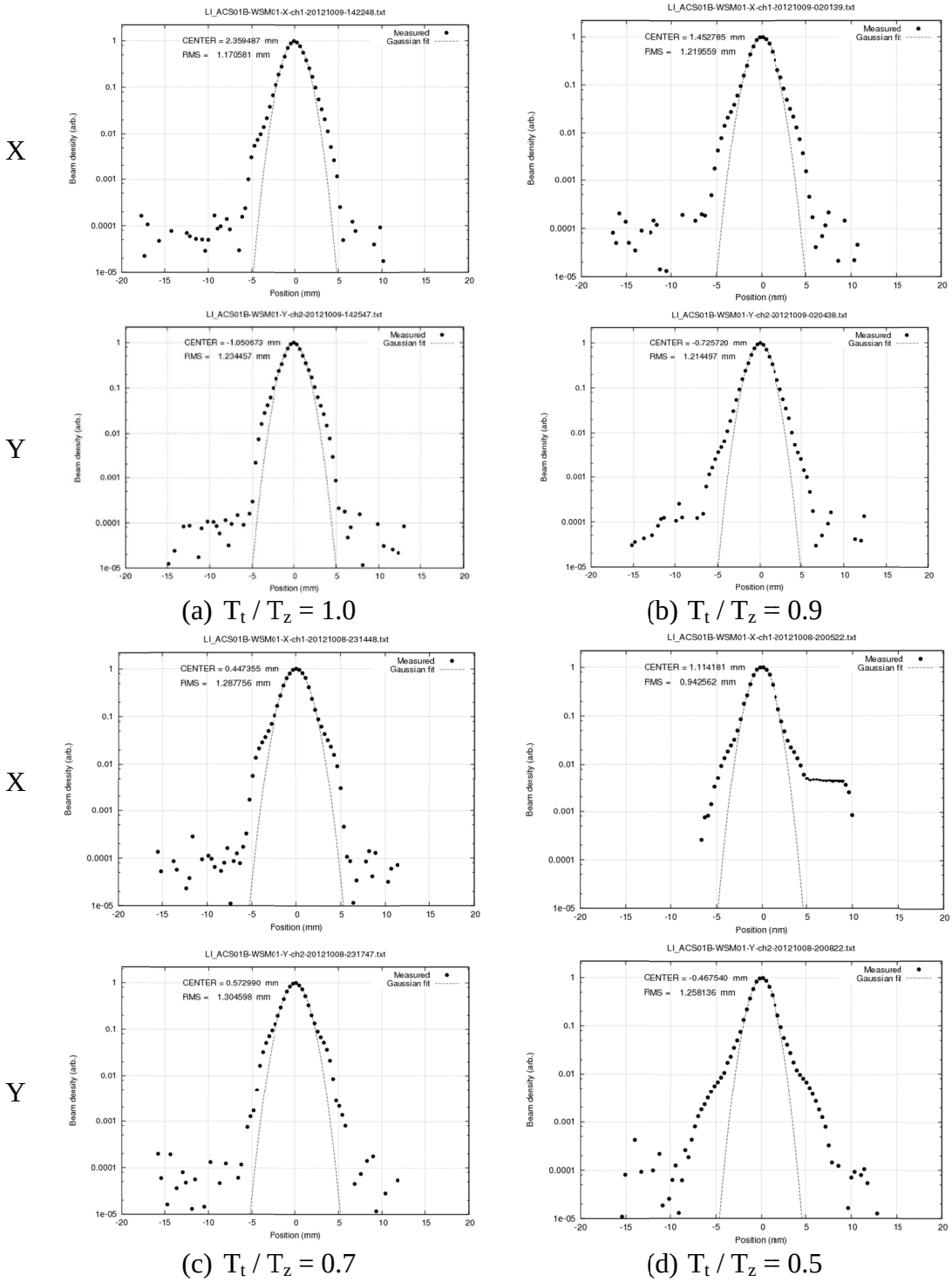

Figure 6-18: Measured transverse beam profiles in the ACS section. The horizontal axis is the measured width (mm) while the vertical is the logarithmic beam density (arb.).

A clear increase in transverse emittance coupled with a decrease of longitudinal one has been observed for the case 0.5. This is the first experimental observation of emittance exchange in a linac driven by the k_z / k_t = 2 resonance and also the first emittance exchange measurement in a proton linac with emittance ratios close to 1. Additionally, unexpected halo has been measured transversely as indicated by the long tails in Fig. 6-18(d). Some exchanges have also been measured for case 0.7, which is unexpected as it has not been predicted numerically or by theory.

Table 6-2: Measured J-PARC linac emittance values for the four working points tested [17].

T_t / T_z	DTL Output [π.mm.mrad]	
	ε_t	ε_z
1.0	0.216	0.269
0.9	0.229	0.233
0.7	0.253	0.223
0.5	0.293	0.161

While the first experimental evidence for emittance exchange at k_z / k_t = 2 in a proton linac in the world with emittance ratios close to 1 is certainly encouraging for the establishment by EP tuning, however questions still remain and efforts are being made to quantify the measurement limitations and fully understand the results. The unexpected emittance exchange seen at T=0.7 was also observed. A strong contender for a possible explanation currently being investigated is transverse mismatch observed at the SDTL input. In addition, the mechanism led to emittance exchange is detailed by the initial mismatch recently [17].

6.3.4 Proposal of Beam Width Tuning Based on the Longitudinal-Transverse Coupling

We proposed another tuning method. As we have no redundancy of the BSMs in J-PARC linac, if one of them is missing by a monitor trouble, we need to consider the new way to tune the longitudinal RMS beam size. We remounted all BSMs to make vacuum improvement and BSM were tested and conditioned. One BSM was installed in front of ACS01 as shown in Fig 6-19. We can measure the longitudinal pulse width using SDTL16, buncher 1, and buncher 2. The amplitude scan curve was obtained as shown in Fig. 6-20. As the discussions above, EP condition should be far from the resonance region to avoid transverse-longitudinal emittance exchange.

We proposed a tuning method using amplitude scan curve and the Twiss parameters obtained by transverse profiles [11, 18]. In the method, we use the following formula.

$$\sigma^2_{BSM} = \varepsilon_z[(1+Lk)^2\beta_B - 2L(1+Lk)\alpha_B + L^2\gamma_B] \quad (6\text{-}4)$$

Where, ε_z is emittance, L is drift length, α_B, β_B, γ_B are Twiss parameters at BSM position, and k is longitudinal focusing force. We substituted σ^2_{BSM} and k which are obtained from Fig. 6-19. These free parameters of ε_z, α_B, β_B, were obtained by iterated calculation and γ_B by 3D-PIC simulation. These parameters were adopted to the buncher and quadrupole settings, and the total beam loss measurements, and finally proper settings for minimum beam loss situation were determined.

We have a plan to develop the BSM for the front-end. As there is no enough space to install a number of BSMs, we will install only one BSM and use this method.

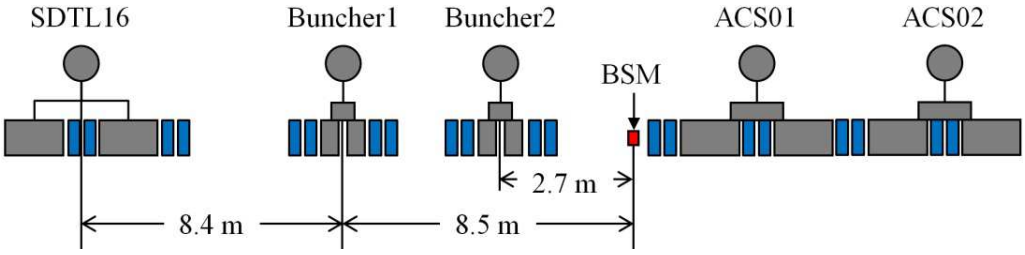

Figure 6-19: One BSM installation layout after SDTL16 with their distance.

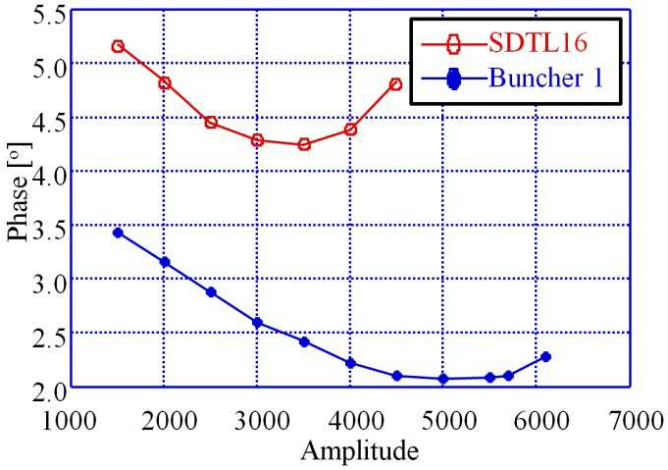

Figure 6-20: Amplitude scan curve by SDTL16 and Buncher 1.

6.4 Summary

BSMs were successfully developed for J-PARC linac in collaboration with INR. The target phase resolution was less than 1.0° and vertical stepping accuracy was less than

0.1 mm. BSMs were installed between the quadrupole doublets and the BSM body was close to the quadrupole magnet, therefore we considered the influence of the quad-magnetic fields for the operational settings. The effect of magnetic shield was evaluated to reduce the magnetic field in the BSM as well as to suppress the accelerated beam size. Also we evaluated the effect of the magnetic shield to the accelerated beam size is 1.5% which is sufficiently small to operate the quadrupole magnets properly [9].
We overcame the vacuum problems accompanied by the installation of BSMs and achieved the super-high vacuum level during the BSM operation. A vacuum system with on-line baking scheme was proposed to operate BSMs without significant vacuum degradation [19].
In the first commissioning, we confirmed the phase accuracy is less than 0.53°. A consistency check of the results using an upward acceleration cavity confirmed agreements of tendencies and absolute phase width compared with the simulated estimations. The effect of wake field generated by the charged particle beam was evaluated as a function of beam current. Lessons leant from the wake field effect evaluation was utilized to estimate the measurement errors and the beam slowdown effect. We showed the RMS phase spread at different horizontal wire positions is caused by the mechanical structure and it should be minimized by accurate wire position.
The high intensity linac design follows the equipartitioning (EP) condition. Beam dynamical experiments were conducted by measuring the longitudinal bunch length with BSMs to make Hofmann's stability charts which indicated a region of space-charge driven transverse-longitudinal coupling resonance. The results supported this chart and the condition to avoid the resonant region was estimated in the operational settings.
BSM measurements will have obvious advantages of measuring longitudinal emittance, while the accuracy of both the transverse and longitudinal emittance measurement was verified. This method brings the discussion back to the choice of a working point (EQ set-point or not) and the use of stability charts in linac design. What this experiment has highlighted is the need to understand the limitations of these design-tools. While these charts are useful guidelines, they cannot substitute a systematic analysis of the influence of mismatch, initial particle distribution, beam tune spread, resonances, errors, etc., supported by thorough self-consistent multi-particle computer simulations.
The implications for future linac designs are clear. With this experiment, there is now sufficient experimental as well as theoretical evidence to support the avoidance of the $k_z / k_t = 1$ and $k_z / k_t = 2$ stop-bands. From the analysis shown in this chapter, it is clear that the design procedure based on the EQ criterion does not necessarily equate with the

absence of emittance growth and halo development. It is also clear that safe working points do exist outside EQ.

In this chapter, we showed that we could conduct the beam dynamical study by the BSMs by which we could monitor both the transverse and the longitudinal emittance simultaneously. In addition, we proposed a new tuning scheme based on the longitudinal monitoring by the BSM and numerical simulations.

References

[1] Witkover R. L., "A Non-destructive Bunch Length Monitor for a Proton Linear Accelerator", *Nuclear Instruments and Methods*, **vol. 137**, No. 2, pp. 203-211, (1976).

[2] A. V. Feschenko, "Methods and Instrumentation for Bunch Shape Measurements", *Proceedings of Particle Accelerator Conference (**PAC 2001**)*, Chicago, p. 517 (2001).

[3]A. Shishlo, et. al., "Non-intercepting method to measure longitudinal Twiss parameters of a beam in a hadron linear accelerator using beam position monitor", *Physical Review Special Topics Accelerator and Beams*, **16**, 062801, (2013).

[4] J. Kim, et. al., "A Detector System for Measurement of the Longitudinal Bunch Shape of a CW Ion Beam", *Journal of the Korean Physics Society*, **Vol. 58**, No. 2, Feb. 2011, pp. 234-238.

[5] N. E. Vinogradov, et. al., "A Detector of Bunch Time Structure for CW Heavy-Ion Beams", *Nuclear Instruments and Methods in Physics Research*, A, **526**, (2004), pp. 206-214.

[6] P. Forck, "Lecture Notes on Beam Instrumentation and Diagnostics", *a text of the Joint University Accelerator School*, (2012).

[7] P. N. Ostroumov, "Review of beam diagnostics in ion Linacs", *Proceedings of the 1998 Linac Conference*, Chicago, IL, August 23–28, p. 724 (1998).

[8] J. Tamura, et. al., "Numerical Study on the Effect of Magnetic Shield of a Bunch Shape Monitor in J-PARC Linac", *Proceedings of the 4th International Particle Accelerator Conference (IPAC2013)*, **THPWO035**, Shanghai, China (2013).

[9] A. Miura, et. al., "Bunch Shape Measurement of 181 MeV Beam in J-PARC Linac", *Conference Proceedings of Journal of the Physical Society of Japan (JPS*), No. 8, 011003, (2015).

[10] A. Miura, et. al., "Bunch Length Measurement of 181 MeV Beam in J-PARC Linac", *Proceedings of the 4th International Particle Accelerator Conference*

(IPAC2013), **MOPME027**, Shanghai, China, May, (2013).

[11] A. Miura, et. al., "Bunch Length Analysis of Negative Hydrogen Ion Beam in J-PARC Linac", *Proceedings of the 2015 International Beam Instrumentation Conference (IBIC 2015)*, **TUPB027**, Melbourne, Australia, (2015).

[12] G. Bellodi, et. al., "Longitudinal Beam Profile Measurements in Linac4 Commissioning", *Proceedings of the 27th Linear Accelerator Conference (LINAC2014)*, **MOPP025**, Geneva, Switzerland, (2014).

[13] I. Hofmann et al., "Space Charge Resonances in Two and Three Dimensional Anisotropic Beams", *Physical Review Special Topics Accelerator and Beams* **6**, 024202 (2003).

[14] R. A. Jameson, "Equipartitioning in Linear Accelerators", *Proceedings of the 1981 Linear Accelerator Conference*, pp. 125, Santa Fe, New Mexico, USA (1981).

[15] T. Pelaia II, "Open XAL Status Report 2013", *Proceedings of the 4th International Particle Accelerator Conference (IPAC2013)*, **MOPWO086**, Shanghai, China, May, (2013).

[16] Y. Liu, et. al., "Stability Studies for J-PARC Linac Upgrade to 50 mA/400 MeV", *Proceedings of the sixth International Particle Accelerator Conference (IPAC15)*, **THPF039**, Richmond, Virginia, USA, May, (2015).

[17] C. Plostinar, et. al., "Summary of the 2012 J-PARC Space Charge Resonance Experiment", in private communication, (2015).

[18] T. Maruta, et. al., "Recent Progress of Beam Study in the J-PARC Linac", *Proceedings of the 12th Annual Meeting of Particle Accelerator Society of Japan*, **WEP014**, Tsuruga, Japan, (2014), in Japanese.

[19] A. Miura, et. al., "Vacuum Improvement of Bunch Shape Monitor for J-PARC Linac", *Proceedings of the 3rd International Beam Instrumentation Conference (IBIC 2014)*, **TUPD09**, Monterey, California, USA, September, (2014).

Chapter 7

Beam Loss Monitor

One of the important issues for the development of high-current and high-brilliance accelerators is to understand the beam dynamics induced by the high power density of the beam. A misaligned beam leads to destroy or heavily activate the accelerator components. This fact makes the beam loss monitor (BLM) system one of the essential diagnostic tools for the beam tuning, the operation, and the interlock system for the machine protection. It should suppress the loss to a level which ensures hands-on-maintenance of accelerator components during shutdown and it should shut out the radiation outside the accelerator shielding. We found that the hands-on limit is corresponding approximately to 1 W/m beam loss in the J-PARC linac.

Regular losses might occur continuously during the running and they correspond to the transport efficiency of the beam in the accelerator. Many factors are important for the design of an appropriate BLM system. In particular, a common requirement for BLMs in high power accelerator is the large dynamic range. In addition, we need radiation resistance, linearity, signal response, and more [1].

Different types of BLMs are used sometimes at the same location to extend the dynamic range and to accommodate other requirements of the monitoring. Usually sensitive BLMs are located to measure small losses and less sensitive ones are to cover the high loss rates or to cover different time scales.

We placed ionization chamber BLMs (hereafter we call them as “gas proportional BLM”) composed of gas container filled with Ar and CO_2 for the entire beam line in the J-PARC linac because of broad energy sensitivity, wide dynamic range, fast response, and ease of the maintenance. The time response is within 1 μs that is fast enough to detect the abnormal beam loss and to operate the interlock system. However the gas proportional BLMs also have sensitivity to the X-ray from RF acceleration cavities that becomes a background while the BLM measurement. In particular, they are difficult to detect the beam loss in the low energy region of accelerator, because the gas proportional BLMs are less sensitive to low energy X-ray which is generated by the beam loss in low energy part of linac.

After the gigantic earthquake occurred on March 11, 2011, the activation level

remarkably increased at the surface of DTL1 cavity at which the beam energy is less than 20 MeV. Although we thought the misaligned beam orbit to be a dominant candidate of the activation, we had a difficulty to measure the beam loss at this part by the ion chamber-type BLM.

Scintillator based BLMs were developed to cover the gas proportional BLMs at the lower energy part of the linac. Also we proposed a new beam-orbit tuning method using the new scintillator based BLMs which provides significant signals at the low energy part of the linac.

7.1 Gas Proportional BLM

A gas proportional BLM in its simplest form consists of two parallel metallic electrodes (anode and cathode) separated by a gap and an applied bias voltage of some hundreds to thousands of volts. The gap is usually fed with a mixed gas (Ar-CO_2).

As an example, we show an argon type gas proportional BLM in Fig. 7-1. A high voltage and a small gap width are preferred to achieve a wide dynamic range as well as to achieve a faster response time of the ionization chamber [2]. We achieved electron collection times of less than 1 μs, even in large chambers, by an appropriate arrangement of the electrodes.

An Ar-CO_2 gas proportional BLM which is presently produced by Toshiba Electron Tubes & Devices Co., Ltd., was developed for the machine protection and the tuning of misaligned beam orbit, for reasons of high sensitivity and fast rise time [3]. It was reported that has an internal gas amplification of 6×10^4 at 2 kV, a dynamic range of 10^3 and a fast rise time of 100 ns [4].

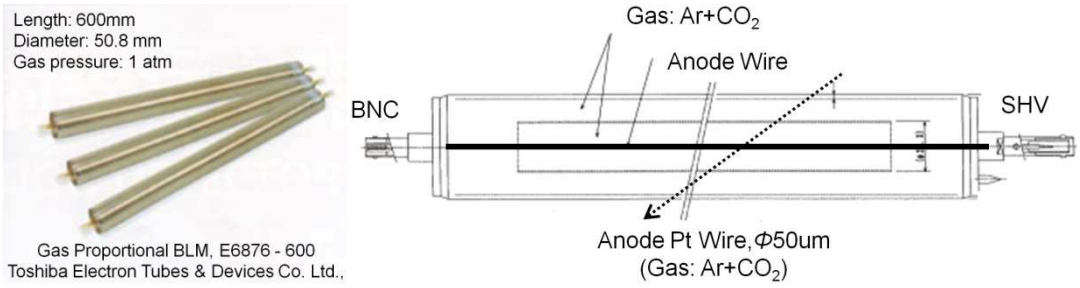

Figure 7-1: Structure of ion chamber (Ar and CO_2 filled).

The BLM system configuration is shown in Fig. 7-2. Considering the sensitivity and the linearity, we supplied a maximum voltage to obtain sufficient output signal. The signal

is amplified and transferred to a signal processing unit. We applied a computer controlled threshold voltage to the comparator, which alerts to the interlock system. To observe the beam loss behavior, we observed the total beam loss using a signal integrator. This provided the integrated beam loss levels of macro pulses at each position. In the J-PARC linac, we obtained the beam loss distribution using a series of BLMs, which is a very important matter for the accelerator tuning.

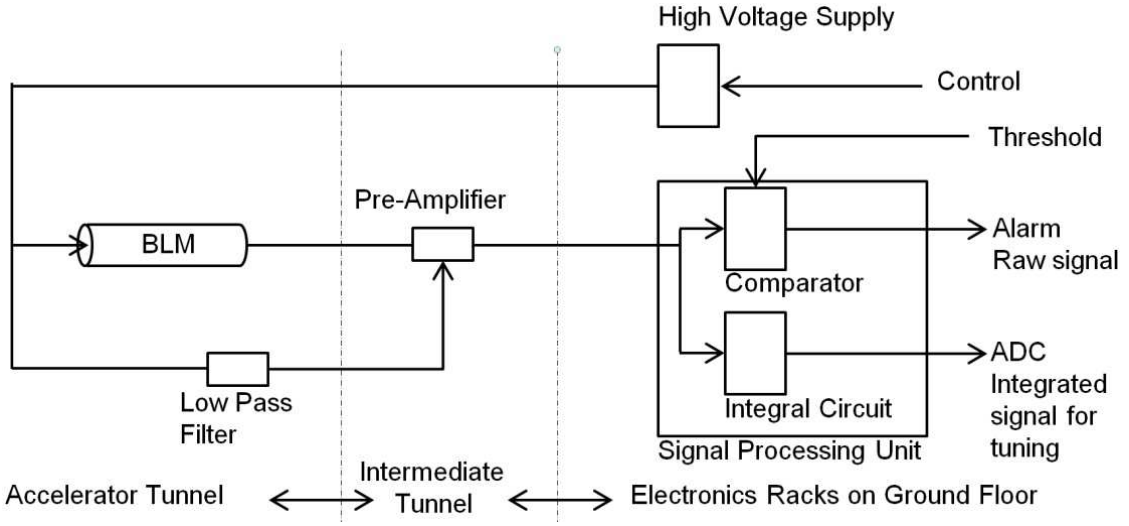

Figure 7-2: System configuration of the beam loss detection using ionization chamber BLM with interlock system.

7.2 Scintillation Detectors

A combination of a scintillator and a photomultiplier (PMT) achieves very fast response (a few nano second) and high sensitivity of beam loss detection [5, 6]. While the plastic scintillator has a life due to radiation damage (usually the transmission decreases to 1/e with 0.01 to 1 MGy dose), it has advantages; less sensitive to low energy X-ray and can be modulated in nearly all shapes and sizes.

Also the adjustable gain of the PMT can increase the dynamic range of this type of BLM. We used photo-multipliers (Hamamatsu H3164-10) with a maximum gain of 1.1 $\times 10^6$, at wavelength of 420 nm, and a rise time of 0.8 ns (Fig. 7-3). The plastic scintillator we used is Saint-Gobain BC-408 [7] which emits a fluorescence with rise time of 0.9 ns and peak wavelength of 425 nm which matches with the photomultiplier.

The BLM using plastic scintillation (hereafter we call it scintillation BLM) system configuration is shown in Fig. 7-4. High voltage was carefully chosen to 700 V by observing the signal waveforms. If the fast time response is the most important issue, the preamplifier can be removed.

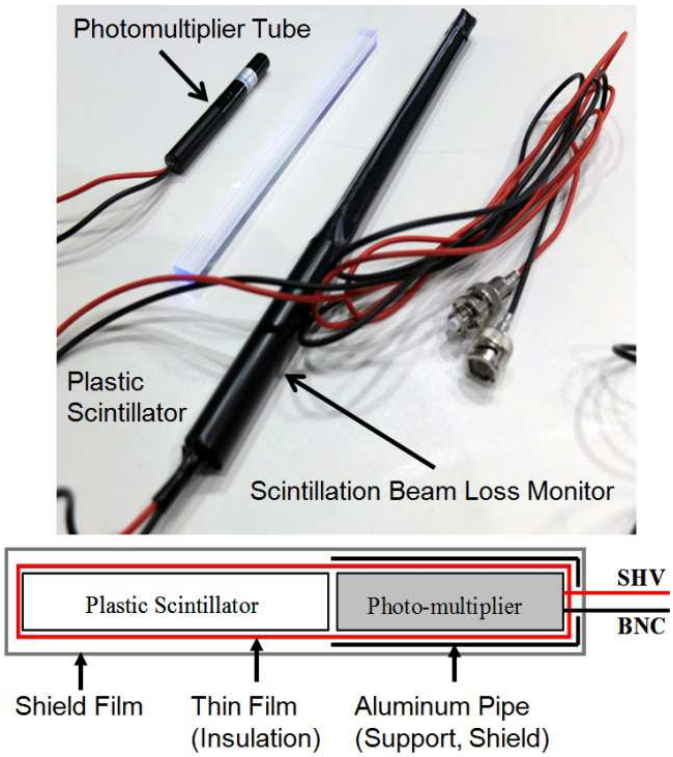

Figure 7-3: Fast and sensitive BLM system composed of a PMT in combination with a plastic scintillator.

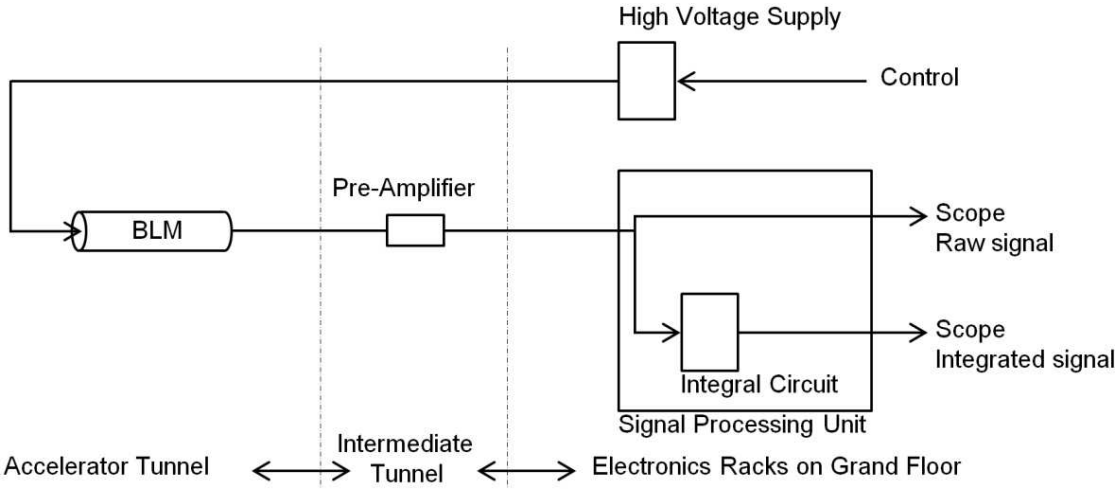

Figure 7-4: System configuration of the beam loss detection using scintillator BLM.

7.3 Beam Loss Measurement with Gas Proportional BLM

We confirmed that the gas proportional BLMs are sensitive to X-rays emitted from the RF cavities. The left waveform of Fig. 7-5 shows the response from BLM in ACS18 with RF “on” but without the beam. When the beam was “on,” the signal waveform changes to the right waveform.

Signal width in Fig. 7-5 was 650 μs corresponding to the RF gate width. We can consider the background X-rays to be an offset value of the integrated BLM signal and estimated the actual beam loss from the difference between beam “on” and “off.”

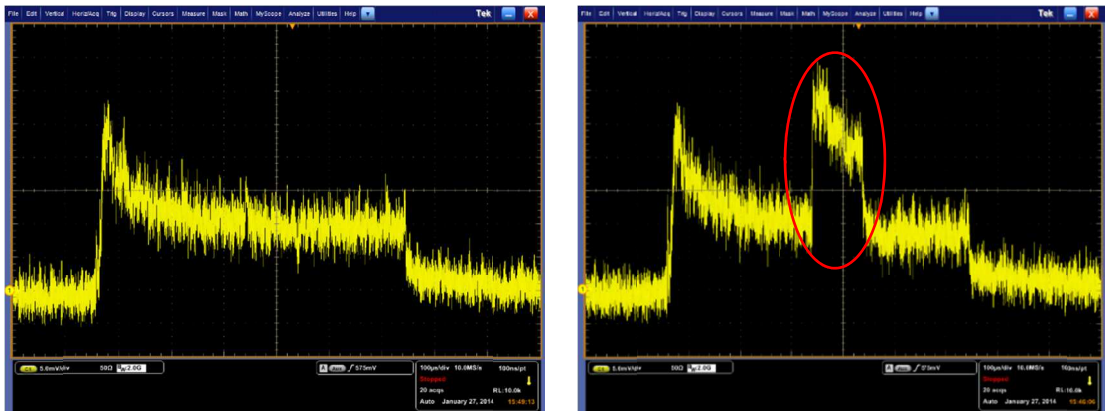

Figure 7-5: Beam loss signal acquired at ACS18, where higher beam loss can be observed. In the panels, the horizontal axis is 100 μs/div, and the vertical axis is 5.0 mV/div.

7.4 Beam Loss Measurement with Scintillation BLM

J-PARC linac has three DTL cavities, and the first DTL cavity consists of 75 drift tubes (DTs) and quadrupoles in the cavity. All DTs were aligned within 50 μm to the center of the magnetic fields.

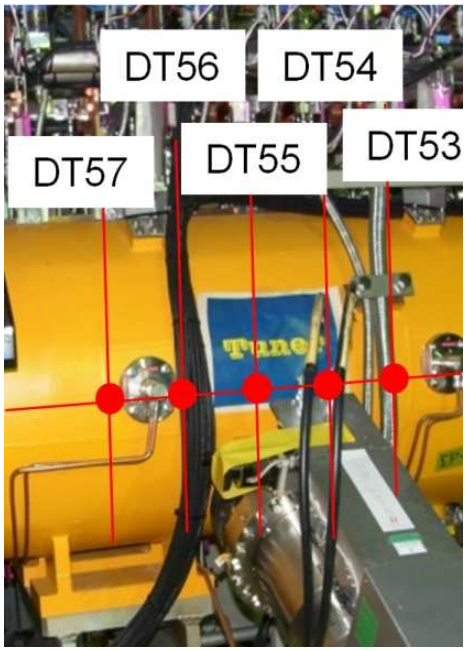

Figure 7-6: Measurement points of residual radiation.

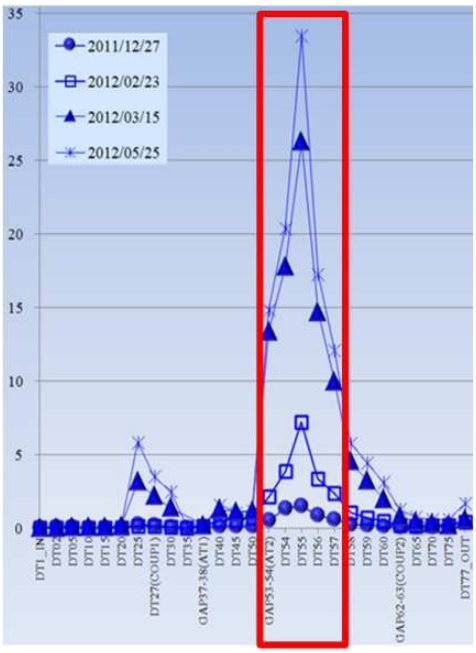

Figure 7-7: Residual radiation at DTL1. Vertical axis is in μSv/h.

Residual radiation was not so remarkable on the surface of DTL cavities before the gigantic earthquake, but after reoperation, remarkably high residual radiation was found (as shown in Figs. 7-6 and 7-7). As the Ar filled gas proportional BLM was less sensitive to the beam loss around DTL, we chose another BLM to support the investigation of the cause of beam loss.

In order to support the gas proportional BLM, we performed a beam loss simulation using the GEANT4 to estimate the loss particle and its distribution generated by the scattering between the beam particles and the residual gas [8]. The region of the simulation covered from SDTL to L3BT. We considered all RF cavities, the quadrupole magnets and the beam pipes in totally 250m of beam transport line as the boundary conditions. Although the residual gas components are considered to be N_2, H_2 and hydrocarbon, we assumed that is composed of nitrogen gas (N_2) with 10^{-5} [Pa] in the beam pipe.

In this simulation, we assumed 10^{12} H^- particles traveled from the SDTL section with initial momentum. H^0 particles were mainly generated by the interaction between H^- particles and residual gas. Figure 7-8 shows the position and the scattering frequency. In the figure, the color indicates the frequency compared with the assumed particle number. The particles with imperceptible angles traveled about 40 m downstream as shown in Fig. 7-8, because the neutral hydrogen particles diffuse to the downstream with the initial momentum.

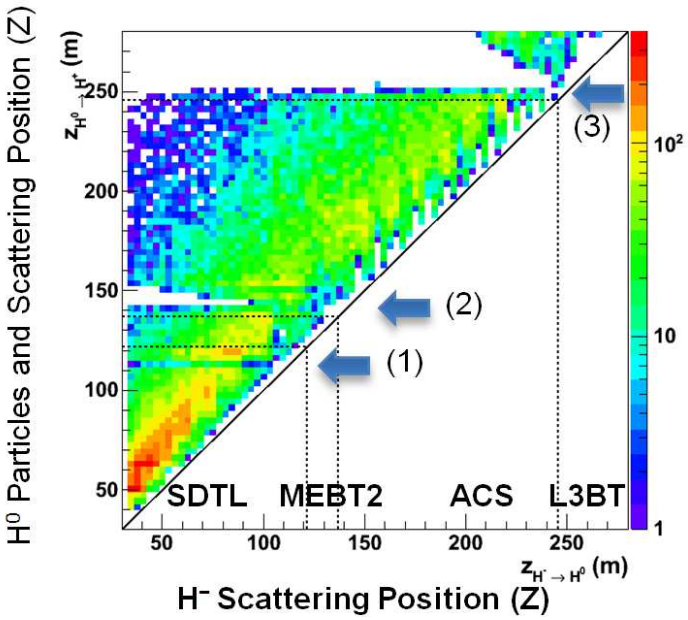

Figure 7-8: Position and frequency of the scattering between H^0 and beam duct.

After the travel to the downstream, they made collisions in the beam duct and interacted with the structural materials, and made the other hadrons. Scattering occurred frequently at the low energy part of the linac (50 m), because of the larger cross section of the interaction at the low energy region. We confirmed three points where the loss events of the collision occur are due to the increase of the duct diameter.
Hadrons are estimated to be produced by the collision between H^0 and the beam duct. The results are shown in Fig. 7-9. We decided to measure the gamma-lay based on this simulation, because the scattered hadrons were accompanied by the gamma-ray.

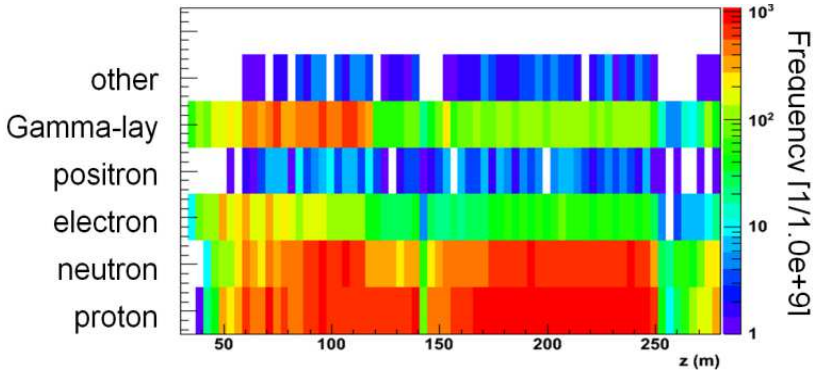

Figure 7-9: Generated hadrons by the interaction between H^0 and the beam duct.

We tested the scintillation BLMs at the downstream of SDTL because we could see remarkable signals with them at high energy part. We set the scintillation BLM behind the gas proportional BLM as shown in Fig. 7-10.We measured the loss particles which deposit a high energy in the scintillation BLM.

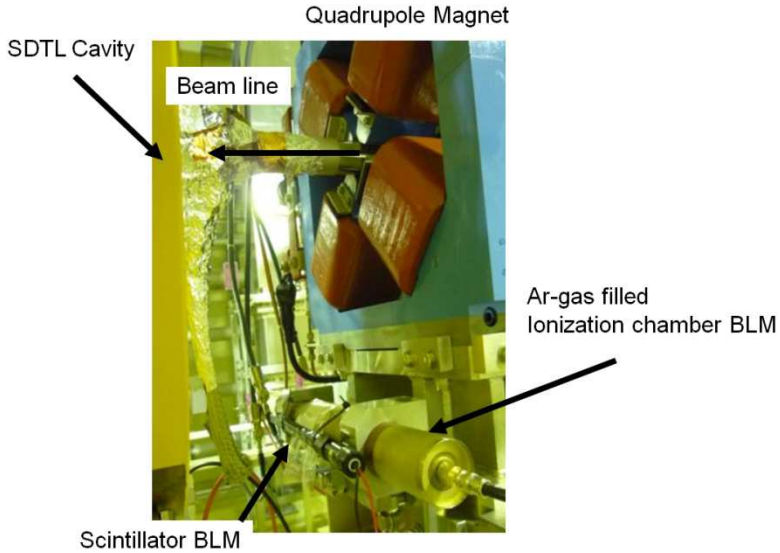

Figure 7-10: Installation layout of Ar-gas filled ionization chamber BLM and scintillator BLM.

Figure 7-11 shows the beam loss signals obtained from the gas proportional counter and the scintillation BLM. As shown, signals from the gas proportional counter had a RF pulse width (600 μs), but the width of signal from the scintillation BLM was 200 μs which corresponded to the actual beam pulse. We obtained good signal response with the plastic scintillation BLM, which had almost no sensitivity to the background X-ray.

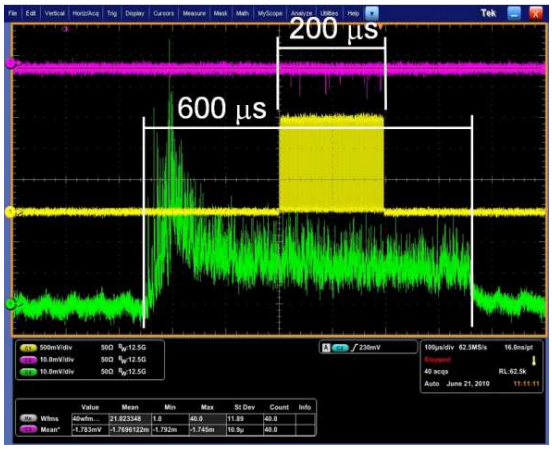

Figure 7-11: Signals from a gas proportional BLM (green) and scintillation BLM (magenta) at SDTL13. Time scale is 100 μs/div. The beam current signal from SCT is also shown (yellow).

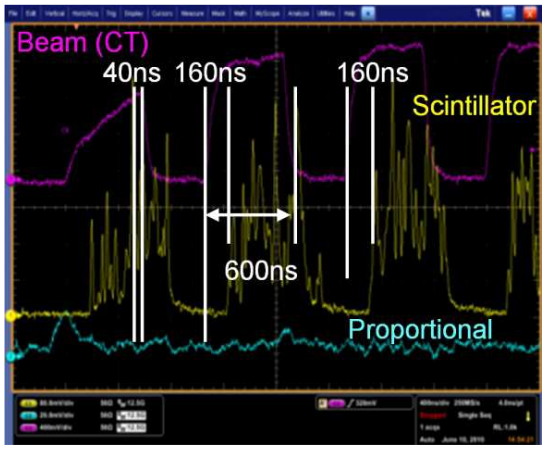

Figure 7-12: Signals from a gas proportional BLM (blue) and scintillation BLM (yellow) at SDTL13. Time scale is 400 ns/div. The beam current signal from SCT is also shown (magenta).

The time resolution of the scintillation BLM was sufficient to measure the beam loss caused by the chopped pulse as shown in Fig. 7-11. Width of the scintillation signal by one event was estimated to be several tens ns. The time delay of the scintillation signal was almost 160 ns and this delay was corresponding to the time constant of the pre-amplifier (in Fig. 7-12). In the test operation with plastic scintillation BLM, we successfully measured clear beam loss signals with low noise level and employed the scintillation BLM to measure the beam loss at DTL1.

Sensitivity of the plastic scintillator (BC-408) is usually matched to the radiation generated at the region of high beam energy, however we confirmed that it still has sensitivity to the beam loss signal in a region of beam energy less than 5 MeV. We installed four scintillation BLMs to both horizontal sides of the DTL1 cavity at DT25 and DT55 (Fig. 7-13). In order to confirm the beam orbit dependence of the beam loss signals at DT25 and DT55, we shifted the beam orbit with a steering magnet located at upstream of DTL [9].

Yellow：Beam Current, 2.0 V/div
Purple：Beam Loss (+x side), 20 mV/div
Green ：Beam Loss (-x side), 20 mV/div

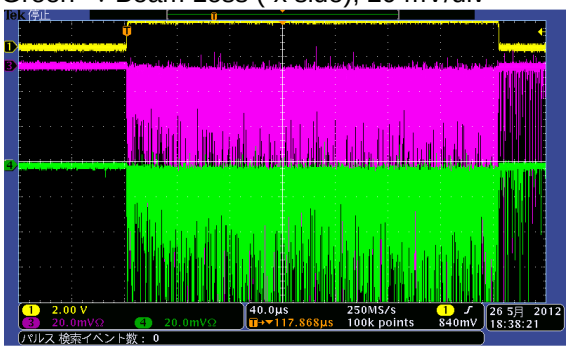

Figure 7-13(a): Beam loss event before beam orbit tuning.

Yellow：Beam Current, 2.0 V/div
Purple：Beam Loss (+x side), 20 mV/div
Green ：Beam Loss (-x side), 20 mV/div

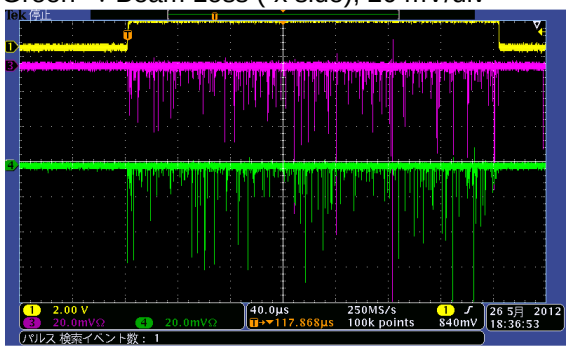

Figure 7-13(b): Beam loss event after beam orbit tuning.

As the results, we obtained fine waveforms using the scintillation BLMs. Waveforms obtained at DT25 are shown in Figs. 7-13(a) and 7-13(b). Figure 7-13(a) shows the waveform obtained before beam orbit correction. Beam orbit was corrected with consistently observing the downstream beam loss. Figure 7-13(b) shows the BLM signals obtained after the beam orbit tuning. This is the way of the beam orbit tuning and we could optimize the beam orbit so as to suppress the beam loss.

As shown, the beam loss was successfully measured by the scintillation BLMs at the surface of DTL cavity even in the low beam energy region.

7.5 Summary

We installed gas proportional BLMs in the J-PARC beam line and used them in the energy-upgraded linac. Although a background X-ray signal was still detected, we could estimate the amount of beam loss. We tried to use scintillation BLMs in the lower energy region of linac. As the results, we successfully obtained clear beam loss signals with low X-ray background by careful designing and calibration.

A beam orbit correction scheme using the BLMs was established at the region where it is difficult to detect the beam loss due to the low beam energy. This new scheme using scintillation BLM is an epochal idea for the accelerator tuning. In addition, this BLM helps in obtaining the loss signal with excellent time response and high sensitivity, so that we can understand the time dependence of the beam loss [10].

The newly developed scintillation BLMs played an important role to mitigate the beam loss and to modify the misalignment of the beam transport of the J-PARC linac after the earthquake.

References

[1] K. Wittenburg, “Specific Instrumentation and Diagnostics for High-intensity Hadron Beams”, *A text of CAS - CERN Accelerator School*, Course on High Power Hadron Machines, May, (2011).

[2] D. Gassner, et. al., “Design and testing of the new ion chamber loss monitor for SNS”, *Proceedings of 2003 Particle Accelerator Conference*, **WPPB019**, Portland, OR, May (2003).

[3] M. Tanaka, et. al., “Investigation of Sensitivity Property of Gas Filled Proportional Counters for J-PARC Beam Loss Monitors”, *Proceedings of the 1st Annual Meeting of Particle Accelerator Society of Japan*, **PP519**, Funabashi, Japan, (2004), in Japanese.

[4] T. Toyama, et. al., “Beam loss monitoring using proportional counters at J-PARC”, *Proceedings of 42nd ICFA Advanced Beam Dynamics Workshop on High-Intensity, High-Brightness Hadron Beams (HB2008)*, **WGF03,** Nashville, TN, (2008).

[5] A. Maltsev, et., al., “A Scintillation-Solid State Detector for Non-Destroying Synchrotron Diagnostics for High Energy Proton Beams”, *Proceeding of the 46th ICFA Advanced Beam Dynamics Workshop on High-Intensity and High-Brightness Hadron Beams (HB2010)*, **MOPD57**, Morschach, Switzerland, (2010).

[6] G. F. Knoll, “*Radiation Detection and Measurement, 3rd ed.*”, in Chapter 8, John Wiley & Sons, Inc., (2000).

[7] Catalog of Premium Plastic Scintillators, Saint-Gobain Crystals.

[8] T. Maruta, et. al., “Beam loss Study at J-PARC Linac by using Geant4 Simulation”, *Proceedings of the 2nd International Particle Accelerator Conference (IPAC11)*, **WEPS047**, San Sebastian, Spain (2011).

[9] A. Miura, et. al., “Beam Loss Occurred at DTL Cavity in J-PARC Linac”, *Proceedings of the 26th International Linear Accelerator Conference (LINAC12)*, **TUPB101**, Tel-Aviv, Israel, September, (2012).

[10] H. Hotchi, et. al., “Beam Loss Reduction By Injection Painting in The 3-Gev Rapid Cycling Synchrotron of The Japan Proton Accelerator Research Complex”, *Physical Review Special Topics Accelerator and Beams*, **15**, 040402, (2012).

Chapter 8

Beam Monitors for Advanced Beam Study

Beam monitors are usually used to observe the continual operational status and tuning, but the monitors can also provide valuable data for the beam physics study. We introduced the beam monitors for the first beam commissioning where we confirmed the beam monitor performances and established the 400-MeV operational parameters. The beam physical study was conducted for the evaluation of important performances of the acceleration cavities which was already introduced.

8.1 First Beam Commissioning after Energy Upgrade

The first beam commissioning of the new ACS cavities had two important missions: (1) to establish 400-MeV operation and (2) to determine suitable parameters for high-power beam operation (i.e., output power of 1 MW). Before attaining 400-MeV operation, we had to deal with two other missions for the beam commissioning: (1) to reproduce 181-MeV operation again in the new beam line and (2) to confirm the proper functioning of beam monitors destined for tuning the ACS cavities [1]. The main purpose of this commissioning was to check the functioning of developed beam monitors whether they accommodate the required specification.

We confirmed appropriate functioning and alignment offset of BPMs using the conventional beam-based calibration (BBC) method shown in the section “3.4 Installation Accuracy: Beam Based Calibration”, which resulted in an installation offset of 18.8 μm.

The functioning of FCTs was checked while delivering the 181-MeV beam to the straight beam dump. The beam energy was measured with various FCT pairs using the TOF method, because the beam bunch structure could be reasonably sustained over the new ACS section. The beam energies measured with different FCT pairs should agree within the expected accuracy for the TOF method, considering the deceleration by exciting idle cavities. In the beam phase measurement, we accounted for the phase offsets from FCT itself and the effect from the signal transmission line.

After tuning the SDTL cavities, we used the 181-MeV beam to compare various FCT pairs for the energy measurement. If the calibration of the offset value was appropriately adjusted to the 324 MHz reference, the output energy was 181 MeV with errors of 1.0%.

All data, with only one exception, were obtained within 0.6% error (corresponding beam energy of 1.0 MeV) by repeated calibrations, as shown in Fig. 8-1. Most importantly, the FCT pair can be used for the phase scan because of the good energy resolution.

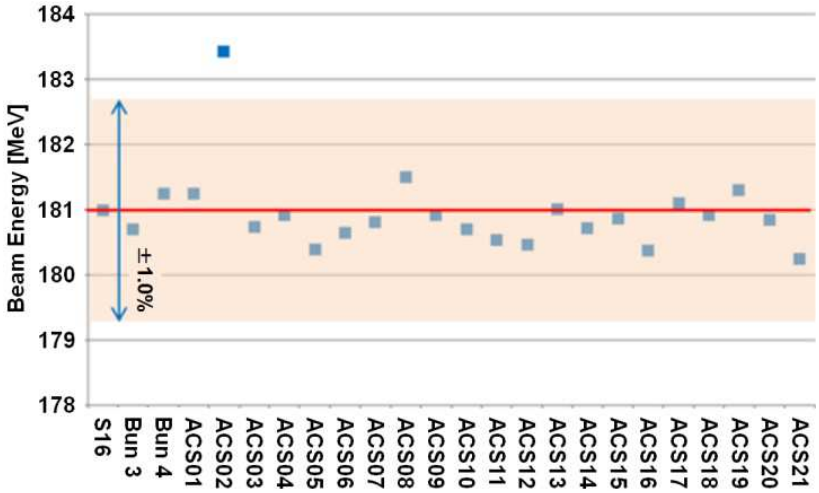

Figure 8-1: Beam energy data obtained by various FCT pairs at 181-MeV operation. S16 means the 16th SDTL cavity, Bun 3 and Bun 4 are the 1st and the 2nd Buncher cavity in MEBT2.

The proper amplitude and phase of each accelerating cavity of ACS were set by the phase scan method. In the phase scan method, the beam energy was measured by the TOF method with a pair of FCTs. The measured energy and simulation results were consistent. The tuning error was within 1.0% in amplitude and 1° in phase. The measured beam energy at the ACS section after the phase scan agreed well with the design energy, with a difference of only 0.6% over the entire ACS section as in Fig. 8-1. The output energy measured at the last ACS cavity was 400.4 MeV, which was only 0.10 % higher than the design value.

We also checked the consistency of data with another energy measurement with BPM. In the L3BT section, we expected that there is the largest dispersion point in the linac. The magnetic field was adjusted to the calculated value based on the measurements for the suitable beam orbit at 400 MeV. When the beam energy shifted from 400 MeV, the beam orbit also shifted. The corresponding energy accuracy was approximately 1.0%, because the positional accuracy of BPM was less than 0.1 mm. The measurement of the beam orbit at the largest dispersion point indicated that the energy shift was within 0.8%, which was below the lowest limit of this method as shown in Fig. 8-2.

After 400-MeV beam injection into the RCS, we measured the beam energy by the

closed-orbit distortion method. According to this measurement, the energy shift was estimated to be 0.21% with corresponding energy shift of 0.84 MeV and the phase shift within 1.0°.

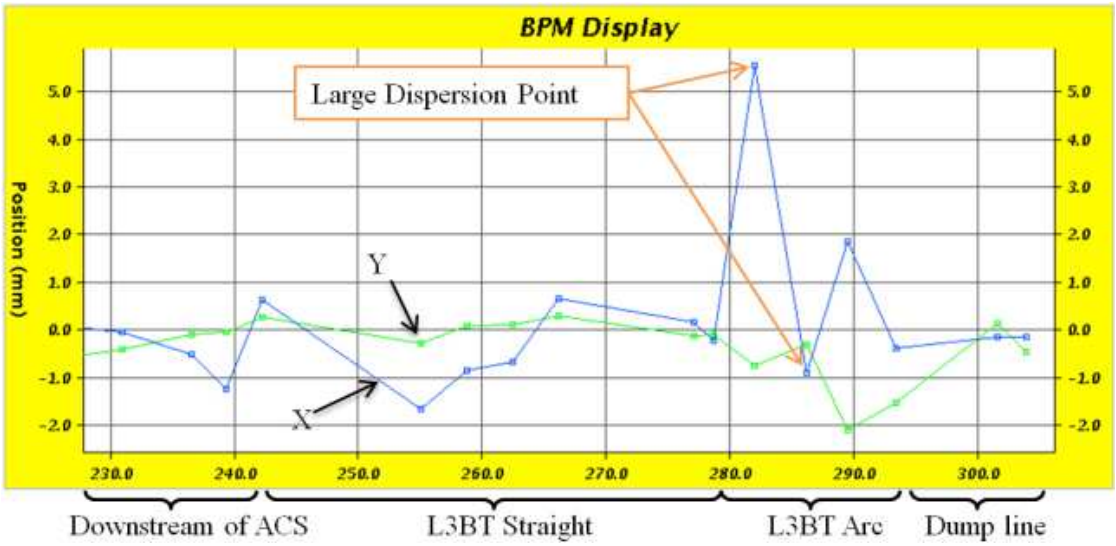

Figure 8-2: Beam orbit at the largest dispersion point of Linac. Blue dots and line are the horizontal orbit, and green dots and line are the vertical orbit. When the beam energy is not ideal, horizontal beam orbit drastically shifted.

8.2 Acceptance Scan of ACS Cavities

The ACS in J-PARC linac is a variation of coupled structure cavity linac with emphasis on the axial symmetry of the RF field [2]. The RF frequency of J-PARC ACS is 972 MHz which is a threefold frequency jump from the SDTL. Because it was the first time to accelerate the beam by the ACS, we needed to confirm the property and to estimate the RF tuning accuracy of cavities. That motivated us to measure the ACS longitudinal properties after realization of 400-MeV acceleration.

We calculated the acceptance by a 3D particle-in-cell code, IMPACT [3]. In the simulation, the initial particles were launched at the ACS entrance distributed over a sufficiently wide area to cover the entire acceptance in the longitudinal phase space. The particles were tracked to the ACS exit without considering space charge effect.

Particles above the energy threshold were chosen at the ACS exit, and then traced back their initial positions at the ACS entrance to obtain the longitudinal acceptance. The blue dotted area in Fig. 8-3 shows the simulated acceptance for ACS. The horizontal axis in this figure is the beam injection phase to ACS with respect to the design synchronous phase ($\Delta\phi_s$). The vertical axis is the difference of injection beam energy with respect to the designed energy (ΔE). As seen in Fig.8-3, the acceptance is ranging from −30 to 60 ° in $\Delta\phi_s$ and from −2.7 to 2.4 MeV in ΔE, respectively [4].

The longitudinal beam distribution was evaluated at the ACS entrance. The particle simulation was performed from the exit of RFQ to the entrance of ACS, in which the output distribution from PARMTEQM [5] was taken as the initial distribution [6]. In the simulation, we adopted the same integrator and the integration step width as the acceptance evaluation. However, we took into account of the space charge effect of beam with 30mA peak current this time. The longitudinal beam distribution at the ACS entrance was superimposed with red dots on the acceptance plot in Fig. 8-3.

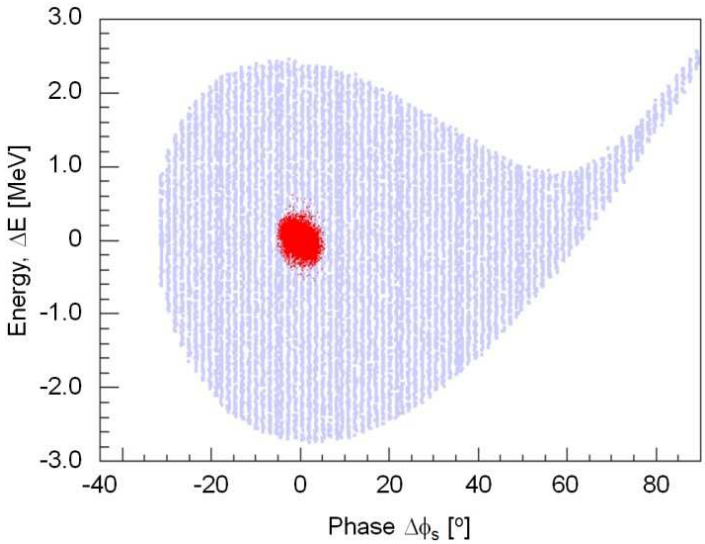

Figure 8-3: Longitudinal acceptance at the ACS entrance (blue points). Designed beam distribution at the ACS entrance is shown with red points [4].

The experiment was conducted at the peak current of 15 mA. When the particles are out of the acceptance, they are not accelerated and are lost fatally. If the beam passed through the L3BT section, the section plays a role of a momentum collimation. Therefore we choose a beam destination in RCS. The RF phase for the ACS cavities were varied while monitoring the beam transmission and the beam orbit at a place in the downstream. The injection beam phase shifted by changing the driving phase of all ACS cavities at the same time with same intervals.

We measured the beam transmission with slow current transformers (SCTs) which were designed to detect the peak beam current. We averaged two SCT signals in the MEBT2 section and regarded as the injection beam current to ACS. Then, we evaluated the average of two SCTs at L3BT in the downstream as the output beam current. The beam transmission efficiency was defined as the ratio between these averages.

Figure 8-4 shows the result of the transmission measurement. In the measurement, we scanned the phase of the injection beam from -45^{o} to 80^{o} with respect to the nominal

phase setting. When the transmission declined to 50 %, we interpreted the beam center was on the acceptance edge. Then we could estimate the acceptance width in the phase direction. The experimental result in Fig. 8-4 indicates that the acceptance ranges from -32^{o} to 60^{o} in $\Delta\phi_s$. As described above, the acceptance range extended from -30^{o} to 60^{o} in the simulation. Therefore, the actual acceptance is slightly wider than the designed value by 2^{o}.

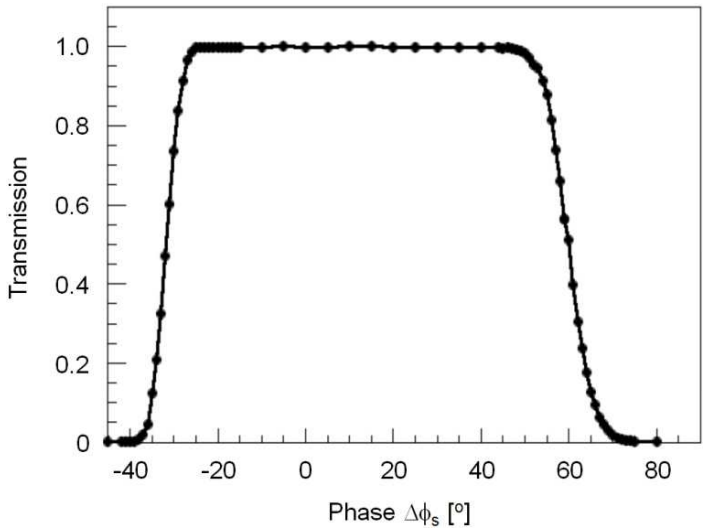

Figure 8-4: Result for the transmission measurement [4].

We measured longitudinal specifications of newly installed ACS accelerator, namely the acceptance width on the phase direction and output beam energy dependence on the injection beam energy. We evaluated the acceptance from the beam transmission to the first arc section downstream to be 92^{o}. It is slightly larger than the design of 90^{o}. Since the acceptance becomes wider as the injection energy increases as shown in Fig. 8-3, the wider acceptance could come when the injection energy increases. As conducted the measurements above, the specification of an accelerator cavity can be evaluated at the point of the beam acceptance range.

As is well known [7], an RF cavity usually has an acceptance width from -30^{o} which corresponds to the synchronous phase with negative direction to $+60^{o}$ to the twice synchronous phase with positive direction. Although the data taken in this study have small disagreement, the width is consistent well with the theory. While tuning of the acceleration cavities, the acceptance scan range was quite important to minimize tuning errors in the J-PARC R&D.

8.3 Summary

We confirmed the functioning of BPMs and beam phase monitors while delivering the 181-MeV beam to the straight beam dump. The accuracy of the beam energy measurement using new pairs of FCTs was under 0.6% at 181 MeV. That resulted in the accuracy of less than 1.0^{o} in phase measurement. The beam energy of 400 MeV was confirmed by two methods of TOF involving the new pair of FCTs and the beam orbit at the largest dispersion point was detected using BPMs.

The longitudinal pulse width of newly installed ACS accelerator was estimated by beam current transmission measurements with phase scanning method. Because this procedure is for checking the cavity specification, special measurement device was not required for it. This is a kind of unique utilization of the current monitors and the results can provide an important information to tune phase settings of the RF cavity in linac.

References

[1] M. Ikegami, et. al., “Commissioning Plan for Energy Upgrade of J-PARC Linac”, *Proceedings of the fourth International Particle Accelerator Conference (IPAC2013)*, **THPWO028**, Shanghai, China, (2013).

[2] H. Ao, et. al., “First High-power Model of the Annular-ring Coupled Structure for Use in the Japan Proton Accelerator Research Complex Linac”, *Physical Review Special Topics Accelerator and Beams*, **15**, 011001 (2012).

[3] J. Qiang, et. al., “An Object-Oriented Parallel Particle-in-Cell Code for Beam Dynamics Simulation in Linear Accelerators”, *Journal of Computational Physics* **163**, 434 (2000).

[4] T. Maruta, et. al., “Longitudinal Measurement of Annular-Ring Coupled Structure Linac in J-PARC”, *Proceedings of the 27th Linear Accelerator Conference (LINAC2012)*, **THPP090**, Geneva, Switzerland, (2014).

[5] K.R. Crandall, et. al., “RFQ Design Codes”, *LANL Report*, **LA-UR-96-1836** (1996).

[6] Y. Kondo, et. al., “Particle Distributions at the Exit of the J-PARC RFQ”, *Proceedings of the 2004 Linear Accelerator Conference (LINAC04)*, Lübeck, Germany, pp. 78-80, (2004).

[7] T. P. Wangler, “*RF Linear Accelerator 2nd Ed.*”, Wiley-VCH, (2007).

Chapter 9

Summary & Conclusions

9.1 Summary

Modifications of original beam monitors are important not only as engineering topics of accelerators but the key issue also to establish the energy upgrade operation. Proposals of the related tuning schemes are also the key issues.

The series of the studies are summarized below.

We designed stripline-type beam position monitors (BPMs) and installed them. We achieved total accuracy of 0.20 mm for beam position measurements. The author achieved center offset of 18.8 μm with accuracy of 0.1 mm by the BPMs in beam based alignment operation after installation.

The design and performances of a slow current transformer (SCT) and a fast current transformer (FCT) were described. It was pointed out that the required time constant of SCT was less than 50 ns and the signal droop rate was less than 1%/μs. As the typical waveform of SCT showed, the rise time was around 20 ns and it had almost no droop for concerning pulse duration. Our commissioning strategy required FCTs which have the phase accuracy of 6.5^{o} and time resolution of 1 ns. It was shown that achieved phase accuracy of the FCT was less than 1.0^{o} and the time constant was less than 1 ns.

The WSMs developed in J-PARC linac achieved a dynamic range over 10^{+4} which provided a successful measurement of beam halo. Tracking the beam halo and its growth are essential to mitigate the beam dynamical problem in high current accelerator. We showed that the wide dynamic range WSM has a world top performance and discussed the mechanism of the wide dynamic range. Namely, this sensitivity was provided by the direct interaction between the wire and electrons which were easily removed from H^{-} particles. This phenomenon had been only understood qualitatively, however the measurement results and the signal estimations enabled to explain it quantitatively.

A new chopper phase tuning method was proposed which was provided by the wide dynamic range WSM. This unprecedented method enabled us to make accurate tuning

not only in present operation but in the high peak beam current operation in near future.
We also developed bunch shape monitors (BSMs) for the J-PARC linac. We evaluated the phase accuracy to be 0.53°, and showed that this is sufficient for the commissioning of the upgraded linac. The high intensity linac design generally follows the equipartitioning (EP) condition. We made the Hofmann's stability charts which indicated space-charge driven transverse-longitudinal coupling resonance. We measured evolutions of the longitudinal emittance with the BSMs. The results supported this chart and we could estimate the operational settings to avoid the resonant region.
By the development of BSMs, an experimental beam physics study could be conducted, where, for the first time, both the transverse and the longitudinal emittance could be monitored simultaneously. In addition to this, we proposed another usage of BSMs for longitudinal tuning in which we use only one BSM and simulation results. This is based basically on a transverse tuning method. However, there is no preceded example of application of BSMs adopted to the longitudinal beam behavior in the world.
Gas proportional beam loss monitors (BLMs) had been used in the beam line and they were also used in the energy-upgraded linac. We could estimate the amount of beam loss with the gas proportional BLMs, however a background X-ray signal was also detected. Then we tried to use a scintillation BLM for lower energy region of linac. The scintillation BLM is usually used to understand the beam loss mechanism because of the fast time response, however, an X-ray background was the problem. This difficulty was successfully overcome by careful design and calibration. As the results, we successfully measured clear beam loss signals with a low X-ray background. There was no example to use the BLMs for orbit tuning at low energy part, because the necessity of careful calibration made difficult to use it for the orbit tuning.
In the 400-MeV beam commissioning stage, we confirmed the beam monitors performance. The error of the beam energy measurement using new pairs of FCTs was under 0.6% which resulted in the accuracy of less than 1.0^{o} in phase monitoring. We confirmed the operation with beam energy of 400 MeV by two methods of TOF involving the new pair of FCTs and by detecting the beam orbit at the largest dispersion point using BPMs.

9.2 Conclusion

The studies presented in this thesis were motivated towards the development of beam monitors for the J-PARC linac as well as establishment of the tuning schemes for the high-intensity proton accelerator using developed monitors. Along with the beam

energy upgrade and peak beam current ramp up projects to reach 1 MW output at the RCS exit, we discussed the accelerator tuning strategy, and the rational beam monitor layout. Based on them, we clarified requirements of the beam monitor specification and developed beam monitors for the new beam line.

In conclusion, we modified the WSM for the high-intensity beam loading and adopted WSMs of wide dynamic range and BSMs of fine phase accuracy for the RF cavity tuning of J-PARC linac. The WSMs provided more accurate matching to suppress excess beam loss and the BSMs provided amplitude tuning of ACS-type buncher cavities to sustain the longitudinal stability.

The BSMs have been usually used to compare the beam behavior with the beam dynamics simulation in preceded studies, but there were quite a few examples of usage for the tuning purpose. We used the BSMs and proposed the tuning schemes to take the beam data in the high intensity beam operation. We showed that our scheme which refers to the longitudinal profile provides a new method for tuning.

These monitoring data will be able to evaluate the tuning scheme based on equipartitioning conditioning in high-intensity operation of J-PARC linac. Although we still need to continue the discussion about the most successful settings, some results obtained in the recent study suggested that the optimum tuning point is differ from the equipartitioning condition.

Finally, the author would like to point out that all of the data of beam monitors obtained in this study will be contributory not only for the development of J-PARC complex but also the beam physical studies in high-intensity ion accelerators.

Acknowledgement

The author is deeply indebted to Professor Kazuhiko Horioka, department of energy sciences, Tokyo Institute of Technology, who gave prescient guidance and discerning comments of the work to accomplish this thesis. The author would also appreciate Professors or doctors Eiki Hotta, Ken Takayama, Yoshiyuki Oguri and Jun Hasegawa for variable and fruitful comments in preparing the thesis.

The thesis was prepared on the basis of part of the work on J-PARC project which has been organized by Japan Atomic Energy Agency (JAEA) and High Energy Accelerator Research Organization (KEK). This acknowledgement is due to all the staffs who have participated so far in the project in J-PARC. The author especially thank to Drs. Kazuo Hasegawa (J-PARC/JAEA), Hidetomo Oguri (J-PARC/JAEA), Nobuo Ouchi (J-PARC/JAEA), Naoki Hayashi (J-PARC/JAEA) for the direction of the J-PARC linac studies. The author especially thank to Drs. Tomofumi Maruta (J-PARC/KEK), Yong Liu (J-PARC/KEK), Masanori Ikegami (The facility for rare isotope beams, Michigan state university) for the prescient beam studies and discussions, Drs. Takeshi Toyama (J-PARC/KEK), Jun Tamura (J-PARC/JAEA), Kenta Futatsukawa (J-PARC/KEK) for the helpful assistance and contribution to my studies. Bunch shape monitors developed at Institute for Nuclear Research, Russian Academy of Science has been used and modified. The author thank for Dr. Alexander V. Feschenko and the late Dr. Alexander N. Mirzojan of the original development of BSM, and fruitful advice of the BSM measurement. For the BSM modification, we had a lot of discussions. Thanks are extended to Mr. Zenei Igarashi (J-PARC/KEK), Tomoaki Miyo (J-PARC/KEK), Yusuke Kawane (J-PARC/JAEA) for the assistance in measurement and experiential advice.

Finally the author has been supported by the family and parents. The author wishes to thank for all. The work associated with this thesis was conducted in the cooperation with many colleagues in J-PARC linac.

Appendix: Publication List

Publication are classified into three categories which consist of 1) refereed research papers, 2) Proceeding papers of international conference and meetings, and 3) proceedings papers of domestic conference and meetings in Japanese. The author's name is highlighted with underline. The author was invited to have a talk of the "Progress of Beam Instrumentation in J-PARC Linac" in the first International Beam Instrumentation Conference (IBIC2012) in the reference of [24] in proceeding papers of international conference and meetings.

1. Refereed Papers

[1] T. Maruta, A. Miura, H. Sako, J. Tamura, M. Ikegami, K. Futatsukawa, Z. Fang, T. Miyao, and Y. Liu, "Progress of Beam Commissioning and Beam Loss Mitigation in J-PARC Linac After the Tohoku Earthquake", *Journal of the Korean Physics Society*, **Vol. 63**, No. 7, October 2013, pp. 1274-1279.

[2] A. Miura, N. Ouchi, H. Oguri, K. Hasegawa, T. Miyao, and M. Ikegami, "Design and Delivery of Beam Monitors for Energy-Upgraded Linac in J-PARC", *Journal of the Korean Physics Society*, **Vol. 66**, No. 3, Feb. 2015, pp. 364-372.

[3] Y. Kondo, T. Morishita, S. Yamazaki, T. Hori, Y. Sawabe, E. Chishiro, S. Fukuta, K. Hasegawa, K. Hirano, N. Kikuzawa, I. Koizumi, A. Miura, H. Oguri, K. Ohkoshi, F. Sato, S. Shinozaki, A. Ueno, H. Kawamata, T. Sugimura, A. Takagi, Z. Fang, Y. Fukui, K. Futatsukawa, K. Ikegami, T. Maruta, T. Miyao, and K. Nanmo, "Beam Test of a New Radio Frequency Quadrupole Linac for the Japan Proton Accelerator Research Complex", *Physical Review Special Topics - Accelerators and Beams*, **17**, 120101 (2014).

[4] A. Miura, T. Maruta, Y. Liu, T. Miyao, Y. Kawane, N. Ouchi, H. Oguri, M. Ikegami, and K. Hasegawa, "Beam Monitors for the Commissioning of Energy Upgraded Linac", *Conference Proceedings of Journal of the Physical Society of Japan (JPS)*, **No. 8**, 011002, (2015).

[5] A. Miura, A. V. Feschenko, A. N. Mirzojan, T. Miyao, N. Ouchi, T. Maruta, Y. Liu, H. Oguri, M. Ikegami, and K. Hasegawa, "Bunch Shape Measurement of 181 MeV Beam in J-PARC Linac", *Conference Proceedings of Journal of the Physical Society of Japan (JPS)*, **No. 8**, 011003, (2015).

[6] K. Hasegawa, H. Oguri, T. Ito, E. Chishiro, K. Hirano, T. Morishita, S. Shinozaki, H. Ao, K. Ohkoshi, Y. Kondo, J. Tamura, S. Yamazaki, T. Hori, F. Sato, Y. Nemoto, I.

Koizumi, N. Ouchi, N. Kikuzawa, A. Ueno, A. Miura, S. Fukuta, A. Yoshii, K. Sato, A. Ozone, Y. Sawabe, Y. Kawane, H. Ikeda, Y. Ito, Y. Kato, K. Kikuchi, F. Hiroki, T. Takayasu, T. Usami, M. Yanai, K. Tadokoro, K. Ohsawa, F. Naito, Y. Liu, Z. Fang, T. Sugimura, K. Futatsukawa, K. Ikegami, M. Kawamura, K. Nanmo, Y. Fukui, T. Miyao, T. Maruta, A. Takagi, "Upgrade and Operation of J-PARC Linac", *Conference Proceedings of Journal of the Physical Society of Japan (JPS)*, **No. 8**, 011012, (2015).

[7] A. Miura, K. Hasegawa, T. Miyao, T. Maruta, Y. Liu, K. Horioka, "Beam Profile Monitor for Intense Negative Hydrogen Ion Beams in J-PARC Linac", Accepted to the *Journal of the Korean Physics Society*, (2015).

2. Proceeding papers of international conferences and meetings

[1] A. Miura, S. Sato, T. Tomisawa, H. Sako, T. Morishita, H. Takahashi, A. Ueno, K. Hasegawa, H. Yoshikawa, "Study of Beam Loss Measurement in J-PARC Linac", *Proceedings of Particle Accelerator Conference (PAC09)*, **TH5RFP096**, Vancouver, BC, Canada, September, (2008).

[2] S. Sato, A. Miura, T. Tomisawa, H. Sako, T. Morishita, A. Ueno, K. Hasegawa, H. Yoshikawa, "Study of J-PARC Linac Beam Position Monitor as Phase Monitor", *Proceedings of Particle Accelerator Conference (PAC09)*, **TH5RFP061**, Vancouver, BC, Canada, September, (2008).

[3] A. Miura, H. Sako, H. Akikawa, M. Ikegami, "Operational Performance of Wire Scanner Monitor In J-PARC Linac", *Proceedings of the first International Particle Accelerator Conference (IPAC2010)*, **MOPE021**, Kyoto, Japan, May, (2010).

[4] M. Ikegami, H. Sako, A. Miura, G. Wei, "Recent Progress in The Beam Commissioning of J-PARC Linac", *Proceedings of the first International Particle Accelerator Conference (IPAC2010)*, **MOPD041**, Kyoto, Japan, May, (2010).

[5] H. Sako, G. Wei, A. Miura, M. Ikegami, "Reduction of Transverse Emittance Growth in J-PARC Linac DTL", *Proceedings of the 25th International Linear Accelerator Conference (LINAC10)*, **TUP067**, Tsukuba, Ibaraki, Japan, September, (2010).

[6] A. Miura, H. Sako, G. Wei, M. Ikegami, "Residual Gas Pressure Dependence on Beam Loss", *Proceedings of the 25th International Linear Accelerator Conference (LINAC10)*, **TUP075**, Tsukuba, Ibaraki, Japan, September, (2010).

[7] A. Miura, H. Sako, K. Yamamoto, N. Kikuzawa, T. Maruta, S. Sato, K. Imai, S. Adachi, H. Sugimura, Z. Igarashi, T. Miyao, M. Ikegami, "Status of Beam Loss Evaluation at J-PARC Linac", *Proceedings of the 25th International Linear*

Accelerator Conference (LINAC10), **TUP076**, Tsukuba, Ibaraki, Japan, September, (2010).

[8] M. Ikegami, H. Sako, A. Miura, G. H. Wei, "Measurement and Simulation in J-PARC Linac", *Proceedings of The 46th ICFA Advanced Beam Dynamics Workshop (HB2010)*, **THO1A02**, Morschach, Switzerland, September, (2010).

[9] A. Miura, S. Sato, T. Tomisawa, Z. Igarashi, T. Miyao, M. Ikegami, T. Toyama, "Beam Diagnostics in the J-PARC Linac for ACS Upgrade", *Proceedings of the 10th European Workshop on Beam Diagnostics and Instrumentation for Particle Accelerators (DIPAC2011)*, **MOPD08**, Hamburg, Germany, May, (2011).

[10] A. Miura, T. Maruta, H. Sako, K. Hasegawa, N. Ouchi, Z. Igarashi, T. Miyao, M. Ikegami, "Beam Loss Detected by Scintillation Monitor", *Proceedings of the 10th European Workshop on Beam Diagnostics and Instrumentation for Particle Accelerators (DIPAC2011)*, **MOPD43**, Hamburg, Germany, May, (2011).

[11] T. Miyao, Z. Igarashi, T. Toyama, A. Miura, "Beam Position Monitors for the ACS Section of The J-PARC Linac", *Proceedings of the 10th European Workshop on Beam Diagnostics and Instrumentation for Particle Accelerators (DIPAC2011)*, **TUPD18**, Hamburg, Germany, May, (2011).

[12] A. Miura, Z. Igarashi, T. Miyao, M. Ikegami, N. Ouchi, H. Oguri, K. Hasegawa, "Beam Monitor Deformation by Tohoku Earthquake and its Recovery Project", *Proceedings of the second International Particle Accelerator Conference (IPAC2011)*, **WEPC144**, San Sebastian, Spain, September, (2011).

[13] A. Miura, T. Maruta, H. Sako, M. Ikegami, Z. Igarashi, T. Miyao, K. Hasegawa, N. Ouchi, "Beam Loss Detected by Scintillation Monitor", *Proceedings of the second International Particle Accelerator Conference (IPAC2011)*, **TUPC104**, San Sebastian, Spain, September, (2011).

[14] T. Maruta, A. Miura, H. Sako, G. H. Wei, M. Ikegami, "Longitudinal Beam Acceptance of J-PARC Drift Tube Linac", *Proceedings of the second International Particle Accelerator Conference (IPAC2011)*, **WEPS046**, San Sebastian, Spain, September, (2011).

[15] T. Maruta, A. Miura, H. Sako, G. H. Wei, M. Ikegami, "Longitudinal Beam Profile Measurement at J-PARC Separated Drift Tube Linac", *Proceedings of the second International Particle Accelerator Conference (IPAC2011)*, **TUPC100**, San Sebastian, Spain, September, (2011).

[16] H. Sako, T. Maruta, A. Miura, "Measurement of Beam Loss Tracks by Scintillating Fibers at J-PARC Linac", *Proceedings of the second International Particle Accelerator Conference (IPAC2011)*, **TUPC102**, San Sebastian, Spain, September,

(2011).

[17] G. H. Wei, A. Miura, K. Hirano, T. Maruta, M. Ikegami, “Dependence of Beam Loss on Vacuum Pressure Level in J-PARC Linac”, *Proceedings of the second International Particle Accelerator Conference (IPAC2011)*, **WEPS048**, San Sebastian, Spain, September, 2011

[18] M. Ikegami, Z. Fang, K. Futatsukawa, T. Miyao, T. Maruta, H. Sako, A. Miura, G. H. Wei, J. Tamura, “Beam Start-up of J-PARC Linac after the Tohoku Earthquake”, *Proceedings of the third International Particle Accelerator Conference (IPAC2012)*, **THPPC010**, New Orleans, Louisiana USA, May, (2012).

[19] M. Ikegami, K. Futatsukawa, T. Miyao, Y. Liu, T. Maruta, A. Miura, J. Tamura, “High Intensity Aspects of J-PARC Linac Including Re-Commissioning after Earthquake”, *Proceedings of The 52nd ICFA Advanced Beam Dynamics Workshop on High-Intensity and High-Brightness Hadron Beams (HB2012)*, **THO3a01**, Beijing, China, September, (2012).

[20] M. Ikegami, K. Futatsukawa, Z. Fang, T. Miyao, Y. Liu, T. Maruta, A. Miura, H. Sako, J. Tamura, G. H. Wei, “Beam Loss Mitigation in J-PARC Linac after the Tohoku Earthquake”, *Proceedings of the 26th International Linear Accelerator Conference (LINAC12)*, **MOPB096**, Tel-Aviv, Israel, September, (2012).

[21] H. Sako, T. Maruta, A. Miura, “Beam Loss Track Measurements by a Fast Trigger Scheme in J-PARC Linac”, *Proceedings of the 26th International Linear Accelerator Conference (LINAC12)*, **TUPB082**, Tel-Aviv, Israel, September, (2012).

[22] A. Miura, T. Ito, K. Hirano, T. Maruta, T. Miyao, K. Nanmo, M. Ikegami, F. Naito, “Beam Loss Occurred at DTL Cavity in J-PARC Linac”, *Proceedings of the 26th International Linear Accelerator Conference (LINAC12)*, **TUPB101**, Tel-Aviv, Israel, September, (2012).

[23] A. Miura, T. Miyao, Z. Igarashi, “Design and Performances of Phase Monitor in J-PARC Linac”, *Proceedings of the 26th International Linear Accelerator Conference (LINAC12)*, **TUPB102**, Tel-Aviv, Israel, September, (2012).

[24] A. Miura, “Progress of Beam Instrumentation in J-PARC Linac”, *Proceedings of the first International Beam Instrumentation Conference (IBIC2012)*, **MOIA02**, Tsukuba, Japan, October, (2012).

[25] H. Sako, A. Miura, T. Maruta, “Status of Beam Loss Spatial Distribution Measurements at J-PARC Linac”, *Proceedings of the 4th International Particle Accelerator Conference (IPAC2013)*, **MOPME024**, Shanghai, China, May, (2013).

[26] A. Miura, H. Oguri, M. Ikegami, “Beam Monitor Layout for Future ACS Section in

J-PARC Linac", *Proceedings of the 4th International Particle Accelerator Conference (IPAC2013)*, **MOPME026**, Shanghai, China, May, (2013).

[27] A. Miura, H. Oguri, N. Ouchi, J. Tamura, A. V. Feschenko, A. N. Mirzojan, K. Futatsukawa, T. Miyao, T. Maruta, M. Ikegami, "Bunch Length Measurement of 181 MeV Beam in J-PARC Linac", *Proceedings of the 4th International Particle Accelerator Conference (IPAC2013)*, **MOPME027**, Shanghai, China, May, (2013).

[28] T. Maruta, M. Ikegami, K. Futatsukawa, T. Miyao, A. Miura, T. Ito, "Beam Loss Monitoring and Mitigation at J-PARC DTL", *Proceedings of the 4th International Particle Accelerator Conference (IPAC2013)*, **THPWO02**, Shanghai, China, May, (2013).

[29] M. Ikegami, T. Maruta, Y. Liu, K. Futatsukawa, T. Miyao, Z. Fang, A. Miura, J. Tamura, "Commissioning Plan for Energy Upgrade of J-PARC Linac", *Proceedings of the 4th International Particle Accelerator Conference (IPAC2013)*, **THPWO028**, Shanghai, China, May, (2013).

[30] M. Ikegami, T. Maruta, Y. Liu, K. Futatsukawa, T. Miyao, Z. Fang, A. Miura, J. Tamura, "Recent Progress in Beam Commissioning of J-PARC Linac", *Proceedings of the 4th International Particle Accelerator Conference (IPAC2013)*, **THPWO030**, Shanghai, China, May, (2013).

[31] J. Tamura, H. Ao, A. Miura, N. Ouchi, M. Ikegami, T. Maruta, T. Miyao, K. Takata, "Numerical Study on the Effect of Magnetic Shield of a Bunch Shape Monitor in J-PARC Linac", *Proceedings of the 4th International Particle Accelerator Conference (IPAC2013)*, **THPWO035**, Shanghai, China, May, (2013).

[32] K. Futatsukawa, Z. Fang, Y. Fukui, M. Ikegami, Y. Liu, T. Maruta, T. Miyao, E. Chishiro, K. Hirano, T. Hori, Y. Ito, N. Kikuzawa, A. Miura, F. Sato, S. Shinozaki, T. Suzuki, "Upgrade of Power Supply System for RF-Chopper at J-PARC Linac", *Proceedings of the 4th International Particle Accelerator Conference (IPAC2013)*, **WEPFI016**, Shanghai, China, May, (2013).

[33] Y. Liu, T. Maruta, K. Futatsukawa, A. Miura, "Studies on wake field in Annular Coupled Structure", *Proceedings of the 27th International Linear Accelerator Conference (LINAC14)*, **TUPP072**, Geneva, Switzerland, September, (2014).

[34] T. Maruta, K. Futatsukawa, T. Miyao, M. Ikegami, Y. Liu, A. Miura, H. Sako, "Recent Progress of Beam Commissioning at J-PARC Linac", *Proceedings of the 27th International Linear Accelerator Conference (LINAC14)*, **TUPP094**, Geneva, Switzerland, September, (2014).

[35] T. Maruta, Y. Liu, A. Miura, "Longitudinal Measurement of Annular-type Coupled Structure Linac in J-PARC", *Proceedings of the 27th International Linear*

Accelerator Conference (LINAC14), **TUPP090**, Geneva, Switzerland, September, (2014).

[36] A. Miura, K. Hasegawa, H. Oguri, N. Ouchi, M. Ikegami, Y. Liu, T. Maruta, T. Miyao, "Installation and Performance Check of Beam Monitors for Energy Upgraded J-PARC Linac", *Proceedings of the 27th International Linear Accelerator Conference (LINAC14)*, **TUPP091**, Geneva, Switzerland, September, (2014).

[37] O. A. Konstantinova, H. Sako, T. Maruta, A. Miura, "Scintillating Fiber Detector for the Beam Loss Proton Measurements at J-PARC Linac", T*echnology and Instrumentation in Particle Physics*, **083**, (2014).

[38] Y. Liu, T. Maruta, A. Miura, M. Ikegami, K. Futatsukawa, T. Miyao, "Stability Studies for J-PARC Linac Upgrade to 50 mA/400 MeV", *Proceedings of the sixth International Particle Accelerator Conference (IPAC15)*, **THPF039**, Richmond, Virginia, USA, May, (2015).

[39] A. Miura, Y. Kawane, N. Ouchi, T. Miyao, "Vacuum Improvement of Bunch Shape Monitor for J-PARC Linac", *Proceedings of the 3rd International Beam Instrumentation Conference (IBIC 2014)*, **TUPD09**, Monterey, California, USA, September, (2015).

[40] T. Maruta, Y. Liu, A. Miura, M. Ikegami, K. Futatsukawa, T. Miyao, "Recent Progress of the Beam Commissioning in J-PARC Linac", *Proceedings of the sixth International Particle Accelerator Conference (IPAC15)*, **THPF040**, Richmond, Virginia, USA, May, (2015).

[41] A. Miura, T. Maruta, Y. Liu, T. Miyao, N. Hayashi, "Bunch Length Analysis of Negative-Hydrogen Ion Beam in J-PARC Linac", *International Beam Instrumentation Conference (IBIC2015)*, **TUPB027**, (2015).

[42] A. Miura, T. Maruta, Y. Kawane, T. Miyao, N. Kikuzawa, "Interlock of Beam Loss at Low Energy Part of J-PARC Linac", *International Conference on Accelerator and Large Experimental Control Systems (ICALEPCS 2015)*, **MOPGF137**, (2015).

3. Proceedings papers of domestic conference and meetings (in Japanese)

[1] S. Sato, Z. Igarashi, T. Tomisawa, A. Miura, A. Ueno, H. Sako, T. Morishita, Y. Kondo, G. Shen, H. Akikawa, M. Ikegami, T. Toyama, S. Lee, "Beam Energy Measurement at J-PARC LINAC"、*第5回日本加速器学会年会*、**WP090**、2009年8月、東広島市中央公民館、東広島市

[2] S. Sato, A. Miura, Z. Igarashi, M. Ikegami, A. Ueno, H. Sako, T. Morishita, H. Yoshikawa, K. Hasegawa, T. Kobayashi, "Tuning of MEBT-Chopper by using wire

scanner monitor”、*第6回日本加速器学会年会*、**WPBDA06**、2009年8月、日本原子力研究開発機構、東海村

[3] 三浦昭彦、佐藤進、佐甲博之、吉川博、長谷川和男、五十嵐前衛、池上雅紀、「J-PARCリニアックACS加速空洞増強におけるモニターシステムの設計」、*第6回日本加速器学会年会*、**TOBDC01**、2009年8月、日本原子力研究開発機構、東海村

[4] A. Miura, T. Kobayashi, K. Hasegawa, H. Sako, M. Ikegami, “MEBT-Chopper Tuning Procedure and its Tolerance”、*第7回日本加速器学会年会*、**THPS053**、2010年8月、姫路市文化センター、姫路市

[5] H. Sako, A. Miura, K. Yamamoto, N. Kikuzawa, S. Sato, K. Imai, S. Adachi, H. Sugimura, “Study for Beam Loss Evaluation at J-PARC Linac”、*第7回日本加速器学会年会*、**THPS079**、2010年8月、姫路市文化センター、兵庫県姫路市

[6] G. H. Wei, M. Ikegami, H. Sako, A. Miura, H. Ao, T. Itou, H. Asano, “Simulation Study of Error Effects for the J-PARC Linac Energy Upgrade - Error study of J-PARC LINAC for 400 MeV upgrade-”、*第7回日本加速器学会年会*、**WEPS046**、2010年8月、姫路市文化センター、兵庫県姫路市

[7] N. Kikuzawa, T. Suzuki, Y. Ito, A. Miura, S. Fukuta, M. Ikegami, H. Sako, T. Kobayashi, H. Suzuki, K. Hasegawa, “Development of Fast Beam-Stop System Using RF Chopper”、*第7回日本加速器学会年会*、**WEPS112**、2010年8月、姫路市文化センター、兵庫県姫路市

[8] 佐甲博之、菊澤信宏、三浦昭彦、丸田朋史、足立智、今井憲一、佐藤進、杉村仁志、「シンチレーションファイバーによるJ-PARCリニアックのビームロス測定」、*日本物理学会　第66回年次大会*、2011年3月、**26pGAB-7**(東日本大震災のため予稿のみ)

[9] 丸田朋史、菊澤信宏、佐甲博之、三浦昭彦、「Geant4シミュレーションを用いたJ-PARCリニアック部ビームロスの研究」、*日本物理学会　第66回年次大会*、2011年3月、**26pGAB-9** (東日本大震災のため予稿のみ)

[10] A. Miura, T. Maruta, H. Sako, K. Hasegawa, N. Ouchi, Z. Igarashi, T. Miyao, M. Ikegami, “Beam Loss Detected by Scintillation Monitor”、*第8回日本加速器学会年会*、**MOPS077**、2011年8月、エポカルつくば、茨城県つくば市

[11] H. Sako, K. Imai, S. Sato, H. Sugimura, A. Miura, T. Maruta, N. Kikuzawa, “Beam Loss Particle Tracking in J-PARC Linac”、*第8回日本加速器学会年会*、**MOPS078**、2011年8月、エポカルつくば、茨城県つくば市

[12] M. Ikegami, Z. Fang, K. Futatsukawa, T. Miyao, Y. Liu, T. Maruta, H. Sako, A. Miura, J. Tamura, G. H. Wei, “Beam Commissioning of J-PARC Linac after

Tohoku Earthquake and its Beam Loss Mitigation”、*第9 回日本加速器学会年会*、**WELR01**、2012 年 8 月、大阪大学豊中キャンパス、大阪府豊中市

[13] J. Tamura, H. Ao, H. Asano, M. Ikegami, T. Maruta, A. Miura, T. Morishita, H. Oguri, N. Ouchi, Y. Sawabe, T. Suzuki, M. Yamazaki, “Beam Loss Reduction by the Beam Duct Realignment in the J-PARC Linac Beam Transport Line”、*第9 回日本加速器学会年会*、**WEPS013**、2012 年 8 月、大阪大学豊中キャンパス、大阪府豊中市

[14] T. Miyao, Z. Igarashi, A. Miura, M. Mayama, “Design And Performances of Phase Monitor in J-PARC Linac”、*第9 回日本加速器学会年会*、**WEPS071**、2012 年 8 月、大阪大学豊中キャンパス、大阪府豊中市

[15] H. Sako, T. Maruta, A. Miura, “Observations of Beam Loss Proton Trajectories in J-PARC Linac”、*第9 回日本加速器学会年会*、**WEPS090**、2012 年 8 月、大阪大学豊中キャンパス、大阪府豊中市

[16] A. Miura, T. Miyao, T. Ito, K. Hirano, K. Nanmo, T. Maruta, J. Tamura, M. Ikegami, F. Naito, “Beam Loss Occurred at DTL Cavity In J-PARC Linac”、*第9 回日本加速器学会年会*、**WEPS094**、2012 年 8 月、大阪大学豊中キャンパス、大阪府豊中市

[17] A. Miura, A. V. Feschenko, A. N. Mirzojan, T. Miyao, N. Ouchi, H. Oguri, K. Hasegawa, M. Ikegami, “Bunch Shape Monitor for J-PARC Linac”、*第10 回日本加速器学会年会*、**SAP088**、2013 年 8 月、名古屋大学東山キャンパス、愛知県名古屋市

[18] K. Hirano, T. Itou, Y. Kondo, S. Shinozaki, E. Chishiro, A. Miura, T. Morishita, M. Ikegami, C. Kubota, T. Sugimura, F. Naito, K. Nanmo, Z. Fang, Y. Fukui, K. Futatsukawa, T. Maruta, T. Miyao, “Development of RF chopper system at J-PARC Linac”、*第10 回日本加速器学会年会*、**SUP016**、2013 年 8 月、名古屋大学東山キャンパス、愛知県名古屋市

[19] T. Miyao, T. Maruta, T. Sugimura, F. Naito, A. Miura, Y. Kondo, T. Morishita, N. Ouchi, H. Oguri, “Beam monitor for RFQ test stand of J-PARC”、*第10 回日本加速器学会年会*、**SUP066**、2013 年 8 月、名古屋大学東山キャンパス、愛知県名古屋市

[20] H. Sako, T. Maruta, A. Miura, “Angular Distributions of Beam Loss Protons at J-PARC Linac”、*第10 回日本加速器学会年会*、**SUP078**、2013 年 8 月、名古屋大学東山キャンパス、愛知県名古屋市

[21] K. Futatsukawa, M. Ikegami, Z. Fang, Y. Fukui, T. Maruta, T. Miyao, Y. Liu, Y. Ito, N. Kikuzawa, F. Sato, S. Shinozaki, E. Chishiro, K. Hirano, T. Hori, A. Miura, T. Suzuki, “Upgrade of Power Supply System for RF-Chopper at J-PARC Linac”、

第10回日本加速器学会年会、**SUP092**、2013年8月、名古屋大学東山キャンパス、愛知県名古屋市

[22] H. Oguri, K. Hasegawa, T. Ito, E. Chishiro, K. Hirano, T. Morishita, S. Shinozaki, H. Ao, K. Ohkoshi, Y. Kondo, J. Tamura, S. Yamazaki, T. Hori, F. Sato, Y. Nemoto, I. Koizumi, N. Kikuzawa, A. Ueno, A. Miura, Y. Kato, S. Fukuta, H. Ikeda, K. Sato, A. Oozone, Y. Sawabe, Y. Kawane, K. Kikuchi, F. Hiroki, T. Iimura, M. Yanai, K. Tadokoro, K. Ohsawa, F. Naito, Y. Liu, Z. Fang, T. Sugimura, K. Futatsukawa, K. Ikegami, M. Kawamura, K. Nanmo, Y. Fukui, T. Miyao, T. Maruta, A. Takagi, N. Ouchi, Y. Ito, T. Suzuki, T. Ishiyama, A. Yoshii, T. Takayasu, T. Usami, "Present Status of J-PARC Linac"、*第11回日本加速器学会年会*、**FSP021**、2014年8月、リンクステーションホール青森、青森県青森市

[23] T. Miyao, A. Miura, Y. Kawane, N. Ouchi, "Calibration of Phase Detector using IQ modulator"、*第11回日本加速器学会年会*、**SAP083**、2014年8月、リンクステーションホール青森、青森県青森市

[24] T. Maruta, Y. Liu, A. Miura, H. Sako, K. Futatsukawa, T. Miyao, M. Ikegami, "Progress of beam commissioning at J-PARC linac after 400 MeV upgrade"、*第11回日本加速器学会年会*、**SUP011**、2014年8月、リンクステーションホール青森、青森県青森市

[25] Y. Kawane, A. Miura, T. Miyao, K. Hirano, T. Sugimura, Y. Kato, Y. Sawabe, S. Fukuta, N. Ouchi, "Interlock System of Beam Line for Beam Current Upgrade"、*第11回日本加速器学会年会*、**SUP099**、2014年8月、リンクステーションホール青森、青森県青森市

[26] 三浦昭彦、高井良太、「IBIC 2014 会議報告」、*加速器*、Vol. 11, No. 4, 2014, (**1-5**).

[27] 丸田朋史、劉勇、二ツ川健太、宮尾智章、三浦昭彦、池上雅紀、「J-PARCリニアックにおけるビーム調整試験の進捗」、*第12回日本加速器学会年会*、**WEP014**、2015年8月、プラザ万象、福井県敦賀市

[28] 岡部晃大、丸田朋史、發知英明、Saha Pranab、吉本政弘、三浦昭彦、Liu Yong、金正倫計、「J-PARC RCSにおける入射ビームのtwiss parameterマッチング」、*第11回日本加速器学会年会*、**THP010**、2015年8月、プラザ万象、福井県敦賀市

[29] 平野耕一郎、近藤恭弘、川根祐輔、篠崎信一、千代悦司、堀利彦、三浦昭彦、森下卓俊、杉村高志、内藤富士雄、方志高、福井佑治、二ツ川健太、丸田朋史、宮尾智章、「J-PARCリニアックチョッパシステムの開発」、*第11回日本加速器学会年会*、**THP012**、2015年8月、プラザ万象、福井県敦賀市

[30] 澤邊祐希、三浦昭彦、石山達也、菊澤信宏、林直樹、丸田朋史、Liu Yong、

宮尾智章、「J-PARC LINAC におけるビームパルス定義変更によるビームロス低減」、*第11 回日本加速器学会年会*、**THP080**、2015 年 8 月、プラザ万象、福井県敦賀市

[31] 二ツ川健太、宮尾智章、川根祐輔、田村潤、根本康雄、林直樹、三浦昭彦、福岡翔太、真山実、「J-PARC リニアック製のバンチ・シェープ・モニタの開発」、*第11 回日本加速器学会年会*、**THP092**、2015 年 8 月、プラザ万象、福井県敦賀市

[32] 宮尾智章、三浦昭彦、川根祐輔、田村潤、根本康雄、青寛幸、林直樹、小栗英知、大内伸夫、真山実、吉川宗良、鈴木隆洋、「J-PARC リニアック　バンチシェイプモニタの真空圧力改善」、*第11 回日本加速器学会年会*、**THP117**、2015 年 8 月、プラザ万象、福井県敦賀市